SEMBLANCE BASED IMAGING OF SCATTERERS WITH AN APPLICATION IN IDENTIFYING NEAR-SURFACE HETEROGENEITIES

A Dissertation
Presented to
The Academic Faculty

by

Tatiana D. Toteva

In Partial Fulfillment
of the Requirements for the Degree
Doctor of Philosophy in the
School of Earth and Atmospheric Sciences

Georgia Institute of Technology
August 2006

SEMBLANCE BASED IMAGING OF SCATTERERS WITH AN APPLICATION IN IDENTIFYING NEAR-SURFACE HETEROGENEITIES

Approved by:

Dr. Leland T. Long, Advisor
School of Earth and Atmospheric Sciences
Georgia Institute of Technology

Dr. Robert P. Lowell
School of Earth and Atmospheric Sciences
Georgia Institute of Technology

Dr. Daniel Lizarralde
School of Earth and Atmospheric Sciences
Georgia Institute of Technology

Dr. Andrew V. Newman
Earth and Atmospheric Sciences
Georgia Institute of Technology

Dr. Carlos J. Santamarina
School of Civil and Environmental Engineering
Georgia Institute of Technology

Date Approved: May 2, 2005

To my Family

ACKNOWLEDGMENTS

I would like to thank several people who have been instrumental in the success of my research and the completion of this dissertation. First of all, my advisor Dr. Tim Long, for his patience, support, and guidance at all stages of my doctoral work. His expertise, innovative vision, and encouragement inspired me during all the years that I worked with him. In addition, I would like to thank Dr. Robert Lowell, Dr. Daniel Lizarralde, Dr. Andrew Newman, and Dr. Carlos Santamarina for taking the time to serve on my thesis committee. Thank you for your advice, comments, and constructive criticism which made the completion of this dissertation possible. Special thanks go to Lester Williams for his assistance with key field measurements and expertise in the interpretation of this data. I would like to acknowledge Anton Darmenov, Peng Zhao, Chunquan Wu, Lei Liu, and Gabriel Hebert for their assistance during various stages of this research as well as the many fellow EAS students who made my "graduate student" life much more enjoyable.

My sincere thanks to the School of Earth and Atmospheric Sciences for providing me with teaching assistantships. Dr. Judy Curry, thank you for your unwavering support and care. Rita Anderson, Susan Ryan, Laura Cederquist, and Kathy Plummer, thank you for your prompt and professional response to any administrative issues I had to deal with.

I am deeply grateful to my parents, my sister, and my friends for their love, patience, and encouragement to follow my dreams. Last, but definitely not least, I would like to thank Richard for his love, friendship, and support. Thank you for standing by my side in the many moments of self-doubt.

This research was supported partially by the Georgia Water Research Institute through the State Water Resources Research Program, Department of Interior, United States Geological Survey. Additional support was provided by the Office of Science (BER), U.S. Department of Energy, Grant No. DE-FG02-04ERG3866.

TABLE OF CONTENTS

LIST OF TABLES

LIST OF FIGURES

SUMMARY

This dissertation investigates a seismic technique for imaging the heterogeneities of near-surface crystalline rocks. Mechanical discontinuities, such as faults, fractures, and cracks that are found at shallow depths are more efficient in scattering seismic energy than velocity discontinuities. Three small-scale seismic experiments were conducted with the objective of identifying shallow scatterers that are principally fractures. The experiment targeted the upper 100m of the Earth's subsurface. The analysis consisted of three steps. In the first step, we acquired data from three seismic arrays, at two different field sites. In the second step, the seismic records were processed using semblance analysis. The goal was to calculate the semblance coefficient for scattered waves as a function of their arrival time, apparent velocity (angle of incidence), and azimuth. This information was the input for the third step – the 3-D imaging algorithm. Scatterers in a homogeneous media were imaged along ellipses with dimensions defined by the true velocity of propagation and the time of arrival. The depth was defined from the ratio of true to apparent velocity. We found that the lack of good coupling between a geophone and the rock is a potentially significant source of undamped resonances that can interfere with the semblance computations. In addition, the semblance analysis shows that narrow-band frequency filtering and short time intervals must be used in order to minimize the interference from wavelets with different lengths and arrival times. The three-dimensional images from an outcrop field site, obtained from scattered *P* and S waves, show good correlation with the geological and GPR data acquired in the area. They outline a zone of contact between granite and amphibolite-biotite gneiss. This contact

zone is most likely controlled by a combination of fractures, joints and differential weathering. The semblance imaging technique failed to locate a subhorizontal fracture within the bedrock of a site with a soil cover. This was probably due to inconsistency between the homogeneous velocity model assumed in the semblance analysis and the layered geological structure at the soil site. Greater attenuation in the soils and the velocity contrast between the soil and rock also contributed to weak signals.

Our results suggest that the technique can be successfully applied to a medium that can be approximated with homogeneous velocity structure. For more complex environments, the algorithm must be modified. First, ray tracing must be incorporated in the algorithm to find the exact locations of the near-surface heterogeneities. Second, geophones and source should be applied to the bedrock to avoid the attenuation from the soil overburden.

CHAPTER 1

INTRODUCTION

This dissertation investigates a seismic technique for imaging the heterogeneity of near-surface crystalline rocks. The concepts for seismic modeling, imaging and digital data processing techniques have been dominated by a vertically heterogeneous Earth model. The subsurface is conventionally assumed to be composed of laterally continuous layers. The layering may be determined by two seismic techniques: seismic reflection and seismic refraction. The seismic refraction techniques primarily utilize the first *P*-wave and *S*-wave arrivals. Reflection seismology utilizes the seismic waves observed to arrive after the direct waves. These late waves, which usually have amplitudes smaller than the direct waves represent reflected and diffusely scattered body and surface waves. In earthquake seismology, these late arrivals are part of the seismic coda. The word coda comes from the Latin word "caudal", which means tail. Aki (1969) suggested that the observed coda of regional *S* waves could be utilized to estimate the attenuation coefficient (1/Q) in the crust. The diffusive character of coda is the strongest evidence for lateral differences in the elastic properties of subsurface rocks. Aki proposed that the laterally heterogeneous Earth structure should be parameterized based on the statistics of velocity and density fluctuations rather than deterministically. Additional evidence for the existence of the lateral heterogeneity comes from direct measurements of geologic structures and observations, such as the variety in rock types recovered from boreholes.

In spite of the numerous surveys and huge amounts of data collected since the coda parameterization proposed by Aki (1969), seismologists still do not have a unique model

for the generation of scattered waves. Still today, the imaging of scatterers is a challenging problem due to the complexity of the seismic records in regions where the dominant inhomogenities are not stratified. This complexity is a manifestation of the diverse nature of scatterers, their irregular distribution, as well as their complicated response to incident seismic energy. The next two sections of this chapter describe this problem in more detail. In addition, the importance of scatterers, the problem statement and the organization of the thesis are outlined in sections 1.3, 1.4, and 1.5 respectively.

1.1. Nature and distribution of scatterers

The heterogeneity of the Earth is widely considered to result from local and regional tectonic processes. The heterogeneity is both compositional and mechanical and exists on all different scales. Wu (1989) shows that the scale length of the lateral heterogeneity spans eight orders of magnitude, from sub centimeter to the size of the earth. Differences in mineralogy (mm to cm), and rock composition (cm to km), cause differences in the elastic properties of rocks. In the deep crust and upper mantle (high heat and pressure regions), the compositional variations cause some zones to be close to their melting point and strongly affect the velocity structure. This is not a major concern at near-surface depths where mechanical heterogeneities such as faults (tens of meters to kilometers), fractures (meters to tens of meters), or cracks (mm to meters) have significant effect on the elastic properties (Simmons and Nur 1968). Mechanical heterogeneities are discontinuities, or surfaces in which loss of cohesion has taken place (Boadu 1994). The loss of cohesion results in a greater scattering potential than the compositional heterogeneity (Walsh 1965). Therefore, the mechanical heterogeneities can have a greater

effect on the incident seismic energy. All types of heterogeneities are potential scatterers of seismic energy, but discontinuities, such as faults, fractures, and cracks are the strongest scatterers in the near-surface environment.

Due to the relatively low temperatures and confining pressures, scatterers are widely distributed within the upper few kilometers of the Earth's crust. The increase of pressure with depth causes the closing of most cracks and fractures at a depth of about 4 km. Sealed discontinuities have less effect on the seismic energy than the open ones. Hence shallow discontinuities are more likely to be open and to scatter seismic energy more efficiently. The method described in this thesis is tested for the upper 100 m of the subsurface, which is a region known to contain open (e.g. water-bearing) fractures.

1.2. Effect of scatterers on seismic waves

When an elastic wave travels through a heterogeneous media, it exhibits changes due to the interaction with scatterers. Scattering is defined as "the change in the direction of energy travel because of collisions or inhomogeneity or anisotropy of the medium" Sheriff (2002). This change in the direction of wave propagation is observed on the seismogram as change in the arrival time, waveform, phase, or amplitude of the recorded seismic signal (Brown and Scholz 1986, Walsh and Grosenbaugh 1974). The scatterer represents a boundary between two media with different chemical composition or physical properties (density, or elastic constants, such as shear modulus, and bulk modulus). For elastic wave propagation, scattered waves can differ in character depending on the orientation, geometry, and dimension of that boundary; the impedance contrast; the frequency of the incident wave; and the angle of incidence. The seismic

energy is scattered as reflected, refracted, diffused, or diffracted waves. The effect of scatterers on the incident energy is usually studied through forward modeling.

Simple analytical models have been developed for the case of a plane harmonic wave incident on a single crack, in a homogeneous, isotropic, linearly elastic background (Mal 1970). More complex solutions (for arbitrary shape and elastic properties of the scatterer) are obtained using the Born approximation (Wu and Aki 1985). This model assumes only slightly different elastic properties of the scatterer compared to the elastic properties of the background medium. In addition, it is limited to the case of scatterers with size smaller than or comparable to the incident wavelength. The same limitation applies to the equivalent media theory (Liu et al. 2000).

The advancement of computer hardware and software led the development of numerical modeling techniques. These techniques are capable of generating more realistic models for studying the complex seismic response of scatterers. Currently the numerical techniques include Maslov theory (Chapman and Drummond 1982), finite-difference method (Frankel and Clayton 1986), pseudospectral method (Fornberg 1988), finite-element method (Lysmer and Drake 1972), spectral finite difference method (Mikhailenko 2000), and boundary element method (Pointer et al. 1998). Figures 1.1, and 1.2 present some results from the boundary element method (Pointer et al. 1998). It is a clear demonstration of the complexity of the radiation pattern as a function of the contrast in the elastic parameters, and the type of the incident wave. The simulations are done for *SH* and *P* incidence, and for three different types of inhomogeneities – a cavity, a fluid-filled inclusion, and an elastic inclusion. The simulations are implemented for different *ka* numbers. The dimensionless *ka* number, where k is the wavenumber of the primary

wave and *a* is the dimension of the scatterer, was proposed by Wu (1989) as a way to describe the scattering of the seismic waves. He showed that when the seismic wavelength is much smaller than the scatterer, the scattering has reflective or refractive character, while when the dimensions of the scatterer and the seismic wavelength are comparable, the scattering wavefield is more complicated. In the simulations of Pointer et al. (1998), the *ka* number is bigger than 1, i.e. the scatterer is bigger than the wavelength of the incident energy. Because of that most of the energy is scattered in forward direction.

Similar results were obtained by Craig et al. (1991), (Figure 1.3). Scattering radiation was calculated for 14% and 28% difference in the velocity contrast between scatterers and the homogeneous elastic crust. Scatterers were approximated by elastic spheres. This simulation resembles inclusions of granite or basalt in a sandstone matrix. The synthetic seismograms are generated by superposition of singly scattered wavelets. Here the scattering response is studied for different ka numbers ($ka<<1$, $ka\sim1$, and $ka>>1$). Again, for big *ka* numbers, the scattering is mostly in forward direction, but for *ka* on the order of or smaller than 1, back-scattering is prevalent.

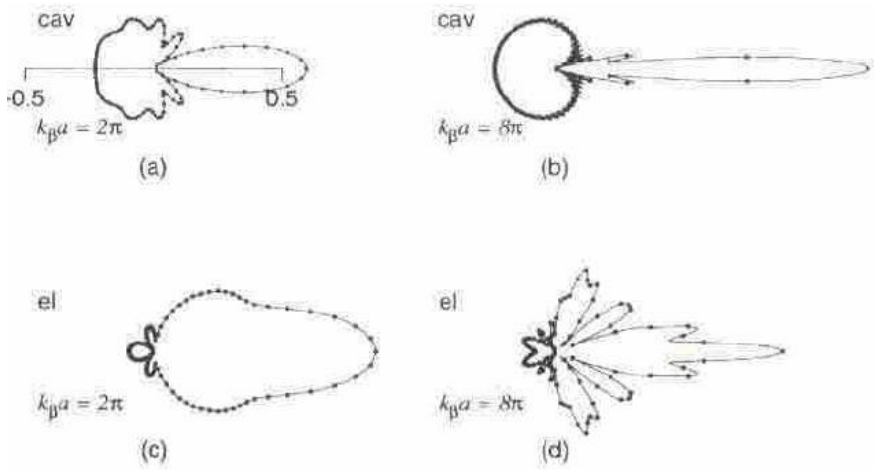

Figure 1.1: The scattered radiation pattern for a plane SH wave incident upon a cavity (a-b), and an elastic inclusion (c-d). Here k_β is the angular *S* wavenumber for the exterior region, and *a* is the scatterer' radius. The solid lines are the results from a numerical simulation and the dots - from an analytical modeling (after Pointer et al. 1998).

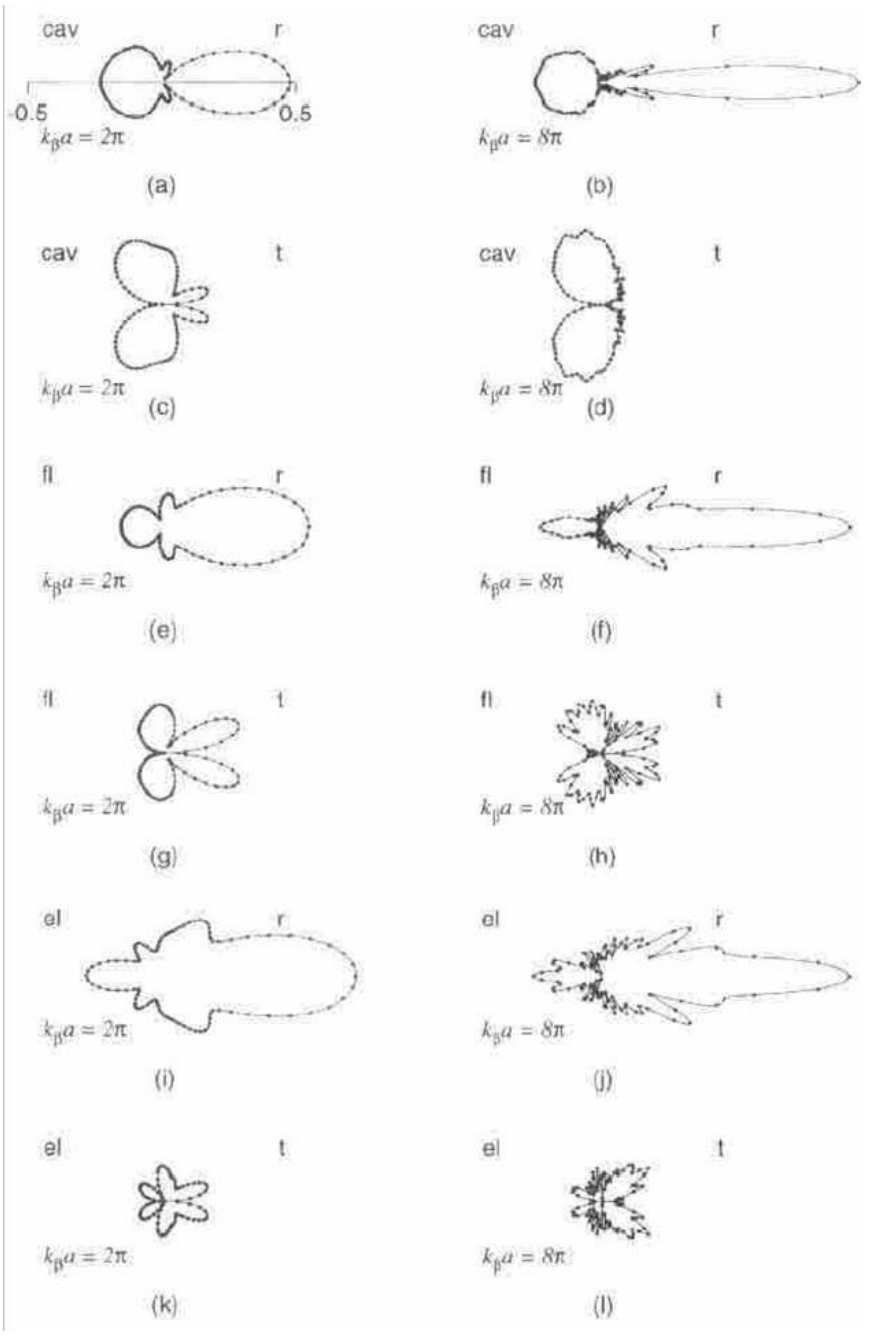

Figure 1.2: The scattered radiation pattern for a plane P wave incident upon a cavity (a-d), a fluid-filled inclusion (e-h), and an elastic inclusion (i-l). Here k_β is the angular *S* wavenumber for the exterior region, and *a* is the scatterer radius. The solid lines are the results from a numerical simulation and the dots are the results from an analytical modeling. The radial and tangential values are denoted as *r* and *t* respectively (after Pointer et al. 1998).

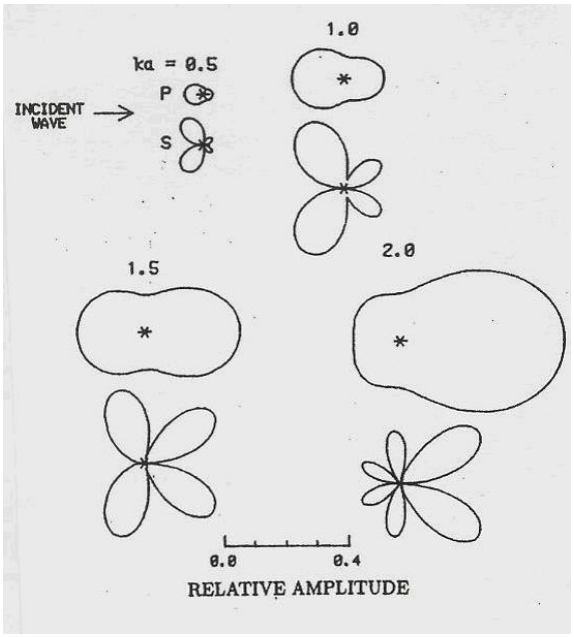

a)

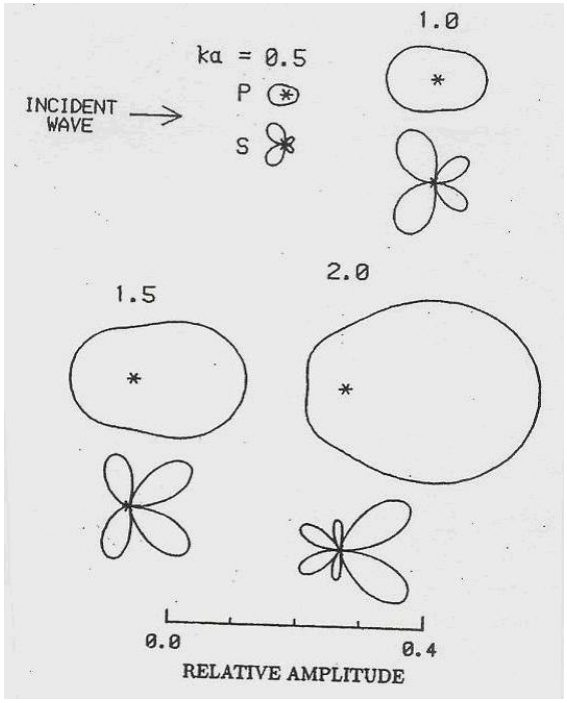

b)

Figure 1.3: Scattering radiation pattern for incident *P* and *S* waves on an elastic sphere with (a) 14 %; and (b) 28 % velocity contrast. The scattered amplitude is calculated for different *ka* numbers (0.5, 1.0, 1.5, and 2.0, for the *P* waves in the host medium), (after Craig et al. 1991)

Craig et al. (1991) assumed singly scattered waves, which is a good assumption for a weakly inhomogeneous media (Revenaugh 1999). These waves are believed to compose the "early coda" (scattered waves arriving soon after the direct waves) of the seismogram. The very tale of the seismogram though is interpreted as a result of multiple scattering (Sato and Fehler 1998). A few different models of multiple scattering have been proposed. These include the diffusion model (Sato and Fehler 1998), and the energy-flux model (Frankel and Wennenberg 1987). Both models have been used to simulate an average scattering intensity of a region rather than imaging the exact location of scatterers.

Numerical simulations of wave propagation in media with discrete distribution of scatterers (fractures rather than inclusions) show a few other effects, which result from the interaction of the incident energy with the scatterers (Vlastos et al. 2003). One effect is that areas of fracture clustering generate strong coherent scattering energy, which is important for the application described in this thesis. The semblance technique presented here is limited in its ability to image single scatterers (e.g. fractures, cracks, etc.), due to the low resolution of seismic methods. For this reason our technique is rather applicable to imaging clusters of scatterers not single scatterers. A basic assumption in our method is that such clusters would generate strong and coherent scattered waves, which is in agreement with the numerical results of Vlastos et al. (2003). In addition, they show that for constant distribution, scatterers with dimensions smaller than the seismic wavelength act as single scatterers, while those with size comparable to the seismic wavelength cause more complicated wavefield (which is in agreement with the conclusions of Wu (1989)).

The scattering process also leads to attenuation in the seismic waves. Scattering attenuation was found to be relevant to the specific shape of the coda (Sato and Fehler 1997). Turner (1998) suggests that the scattering attenuation is not only due to dissipation of energy but also due to that energy converting into different modes. In other words, the attenuation is a spatial loss rather than a temporal loss, as is the true dissipation process or absorptive attenuation.

1.3. Why are scatterers important?

The nature of scatterers defines their importance not only from scientific but also from social point of view. Mechanical scatterers, such as fractures and cracks play key role in the distribution of fluids of different types. Such fluids include hydrocarbons, different types of contaminants, or underground water.

In the exploration industry knowledge of the spatial distribution of scatterers (e.g. fractures) could be used in the optimization of the production of coal, minerals, petroleum etc. For example, natural fractures provide critical permeability pathways for efficient gas yield in low-permeability gas reservoirs (Grimm et al. 1999). Induced (hydraulic) fracturing is sometimes used to stimulate the production of hydrocarbons (Groenenboom and Falk 2000). This is a process of injection of high pressure fluid into a well to induce the opening of new fractures.

In earthquake engineering seismology, the location and character of faults are important components in earthquake-hazard analysis. The presence of fractures defines the subsurface integrity at critical locations such as power plants, refineries, waste-disposal facilities, and chemical plants. So, an efficient method for imaging scatterers

would be a useful tool in defining the design parameters for the construction. It could prevent both future engineering and environmental problems.

In earthquake prediction studies, the variation in the stress field during the preparatory period of an earthquake has been hypothesized to lead to a change in the geometry of the fractures and faults and their strength properties (Jin and Aki 1989, Fehler et al 1988, Novelo-Casanova et al 1985). Even though this hypothesis is still a subject of on-going debate, if it is proven true, the imaging of such changes could be used in earthquake prediction.

Scatterers have (a potential) importance in the new emerging field of environmental geophysics. This field has the objective of using geophysical methods for characterization of the upper 100 m of the earth's subsurface. This area contains aquifers, most of which have retaining properties that result from the presence of fractures and cracks. Also, fractures and cracks are potential pathways for chemical contaminants. The effect of fluids on both *P* and *S* waves (Van der Kolk et al. 2001) is significant, and an imaging technique could be applied not only to locate scatterers but also to monitor the movement of water and the pollutants it carries.

1.4. Problem statement

The many areas where fractures are important components of the earth model described in section 1.3 define the need for an efficient imaging technique. Imaging of scatterers can be accomplished through various inversion techniques. Chen and Long (2000), and Nishigami (2000) have developed scattering inversion techniques for earthquake data. These techniques use the larger amplitude shear waves from earthquake

sources and record the waves that have propagated 10's to 100's of kilometers, i.e. are suited to image deeper scatterers. The near-surface scattering of seismic energy is a problem of imaging smaller volumes, at shorter distances, and requires higher frequencies. This application is made difficult by the attenuation of the high frequencies in near-surface soils. Over the last decade a few field experiments were conducted with the objective of extracting information for reflectors with depths up to 100 m (Steeples and Miller 1998, Steeples and Green 1997, Bachrach and Mukerji 2004, Bachrach and Nur 1998, Bradford et al. 2006, Ghose et al. 1998, Hebert 2005). These methods are focused on obtaining high-resolution images using modified versions of conventional seismic reflection methods and therefore are not cost-efficient for near surface applications. Besides the progress in the near-surface techniques, the later portions of the seismogram, which contain shallow scattered *P*, *S*, and surface waves remain underutilized.

This thesis describes an inversion scattering technique for imaging shallow scatterers (located within the upper 100m of the subsurface). It was tested in the Panola Mountain Research Watershed, which is located in a remote area east of Atlanta, GA. This area is in the Georgia Piedmont, which is underlain by igneous and metamorphic rocks. Fracture systems in these near-surface crystalline rocks have the potential to supply large quantities of fresh water to the region (Williams et al. 2004). However, because groundwater occurs in irregular and highly discontinuous openings in the bedrock, the exploration and development of these resources has been limited. A simple, cost-efficient, and reliable technique is needed to identify the location, depth, and continuity of subsurface water bearing zones, prior to test drilling. Electrical noise,

conductive structures, and buried utilities in urban areas significantly limit the use of electrical and electromagnetic techniques, while the high clay content of surface soils prevents acquisition of usable ground penetrating radar signals.

1.5. Principle objectives of the thesis

This thesis had the general objective of developing a non-invasive and cost-efficient technique for imaging shallow scatterers. This technique consisted of three main stages: data acquisition, processing, and imaging. Each of these stages had more specific objectives, as listed below.

1) To develop a high-frequency, non-invasive and cost-efficient data acquisition method for imaging the upper 100 m of the subsurface.

2) To develop a signal-processing algorithm, capable of utilizing the late portion of the seismogram that may contain scattered waves with low signal-to-noise (S/N) ratio.

3) To develop an imaging algorithm that can project the scattering intensity into a three-dimensional space.

4) To test the technique at two different sites in order to study its limitations, while preserving the requirement for non-invasiveness. Each site had different geological characteristics – an area with a few meters thick soil layer, and a rock outcrop. A rock surface will mitigate the dispersion of the surface waves, while a soil layer will enhance it. The dispersed surface waves may interfere with shallow scattered waves. The purpose is to study the performance of the technique in the presence of soil.

5) To acquire additional geophysical and geological data in order to evaluate the uncertainty in the imaging algorithm. The geological data provide the "big" picture, while the GPR data provide very high-resolution images of the near-surface.

1.6. Thesis organization.

The thesis is divided into seven chapters.

Chapter 2. An overview of the work done on obtaining three-dimensional images of scatterers. Different imaging methods are discussed and compared with the semblance method used in this study.

Chapter 3. Describes how the experiment was designed, the type of equipment that was used, and the acquisition parameters. The field sites for the data acquisition are described as well.

Chapter 4. Describes the semblance method, and the algorithm that was developed to identify coherent arrivals. The algorithm was tested with synthetic data, and with direct surface waves. Results from scattered surface and body waves are shown and discussed.

Chapter 5. Describes the imaging algorithm, and presents the images from scattered surface and body waves in 2D and 3D. The images are presented in the form of depth slices, cross-sections, and 3D images.

Chapter 6. This chapter offers a discussion on the interpretation of the scattered 3–D images obtained with the semblance based technique. Here, some additional data, such as geological and GPR, are included to facilitate the interpretation.

Chapter 7. Presents the conclusions, and the recommendations.

CHAPTER 2

METHODS FOR THREE-DIMENSIONAL IMAGING OF SEISMIC SCATTERERS

2.1. Introduction

In exploration geophysics 3-D images of the subsurface are obtained from two-dimensional surface arrays of seismic sensors and/or sources. In earthquake and nuclear explosion detection, seismic arrays were originally built in the 1960's. It was not until the early 1970s before seismic arrays were deployed for three-dimensional seismic imaging in non-reflection seismology applications. As opposed to a single station recording, arrays allow the determination of the vector velocity of an incident wave (i.e. slowness and back azimuth) instead of only the amplitude and time of arrival. The use of arrays leads to significant improvement in the S/N ratio, and from there to much higher resolution in the seismic images. Yet, the resolution depends strongly on the spatial distribution of the array elements, in particular on their relative offsets and the array aperture. In earthquake seismology, seismic stations in an array could be spaced as close as a few tens of meters apart, but the elements of source arrays (i.e. earthquakes) may be separated by tens and hundreds of kilometers. In petroleum and environmental industry, the spatial layout of both source and receiver arrays is controllable. For this reason the 3-D techniques used in natural (i.e. earthquakes) and man-made (i.e. weight-drops, explosions, air guns) sources differ. In the petroleum and environmental industry (where man-made sources are used) the arrays are usually much denser than in earthquake studies. In exploration reflection seismology the traditional method for 3-D imaging is

migration. The techniques of migration are designed around dense arrays of sensors and sources, and are expensive in terms of acquisition and data processing. Migration methods are discussed in more detail in section 2.5 of this chapter. Other 3-D imaging methods include slant-stack, F-K analysis, double-beam imaging, and semblance. These are discussed in the subsequent sections. At the end of the chapter is offered a comparison between the different methods (Table 2.1).

Three-dimensional imaging in exploration reflection seismology is usually preceded by a number of data processing steps using signal processing techniques (e.g. frequency filtering, amplitude gain control, and stacking), which have the purpose reducing the amount of noise, normalizing the source, and correcting for surface topography (static corrections). Some seismic processing steps are particularly developed for three-dimensional surveys, but most are adopted from two-dimensional analysis. Some of these techniques will be discussed along with the description of the imaging methods.

2.2. Slant-stack method

The process of slant stacking is expressed as "time shifting traces proportional to their distance from some reference point and then stacking; the effect is to emphasize events with certain dips, that is to beam-steer" (Sheriff 2002). This technique is useful in areas of dipping reflectors. The time shifting of the traces can be done for a fixed horizontal slowness and a range of azimuths or for a fixed azimuth and a range of horizontal slownesses. Because the result of a slant-stack process is displayed as a vespagram, it is also known as the vespa process. The vespagram is a diagram of the seismic energy v of

the incoming signal as a function of slowness or back azimuth. The seismic energy υ is estimated as follows:

$$\upsilon_u(t) = \frac{1}{M}\sum_{i=1}^{M} x_i(t - t_{u,i}) \qquad \text{(Eq.1)}$$

Where $x_i(t)$ is the seismic amplitude at station i, $t_{u,i}$ is the relative travel time to station i for slowness u, and M is the number of array stations (Rost and Thomas 2002). This is also known as the linear slant stack method. An example of a vespagram (Rost and Thomas 2002) is shown on Figure 2.1. The energy of the *P*, *PcP*, and the reflected *PdP* phases is plotted as a function of time and slowness for theoretical back-azimuth of 26.6°. For a better resolution in measuring the velocity (or back-azimuth), i.e. for a better separation of arrivals with similar slownesses (or back-azimuths), the Nth root slant stack method is used instead of the linear one (Figure 2.1b). The seismic energy υ in this case is estimated as:

$$\upsilon_{u,N}(t) = \left|\upsilon'_{u,N}(t)\right|^N \frac{\upsilon'_{u,N}}{\left|\upsilon'_{u,N}\right|} \qquad \text{(Eq.2)}$$

Where

$$\upsilon'_{u,N}(t) = \frac{1}{M}\sum_{i=1}^{M}\left|x_i(t - t_{u,i})\right|^{1/N} \frac{x_i(t)}{\left|x_i(t)\right|} \qquad \text{(Eq.3)}$$

N stands for the Nth root (i.e. N=2,3,4….). Taking the Nth root of the traces leads to a reduction in the amplitude differences in the samples, i.e. to reduction in the amplitude variance of the trace (Rost and Thomas 2002).

Matsumoto et al. (1998) proposed a slant-stacking method to be applied to a sparse type of array. Three-dimensional images of the scatterer distribution in the area of the 1995 Kobe earthquake were obtained. The sources of seismic energy were 12 explosions.

The receiver array consisted of 162 stations, equipped with 1 Hz and 2 Hz vertical and three-component seismometers. Even though the receiver arrays had a small aperture and station separation of several tens of meters, the sources were spread at offsets of over 10km. The waveforms were band passed at 6-10 Hz, and stacked for 50 and 140 degrees azimuth, over a range of slownesses, from -0.18 to 0.18 s/km, with a step of 0.01 s/km. Plane wave propagation was assumed, as well as no multiply scattered waves, and no mode conversion.

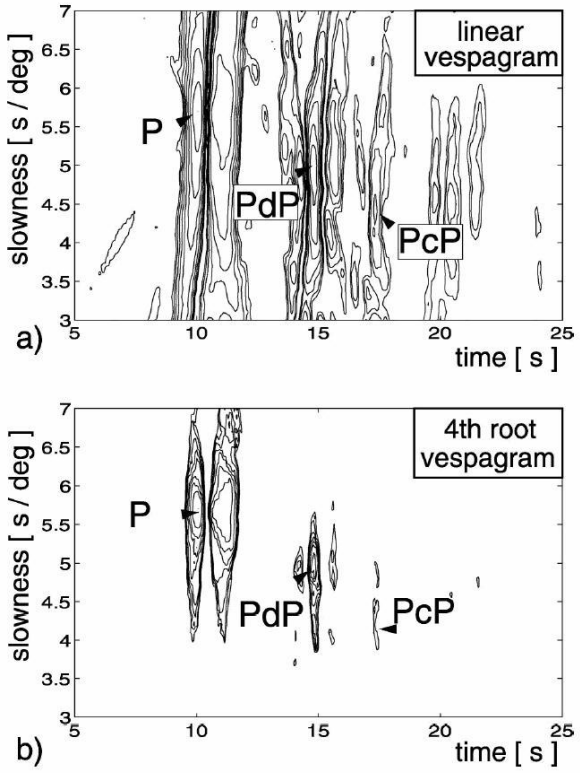

Figure 2.1: Vespagram for a 5.9M earthquake in the Kuril region. The seismic energy of three arrivals – P, PcP, and the PdP reflection are marked. PdP and PcP show slightly smaller slowness than P. (a) linear vespagram; (b) fourth-root vespagram (after Rost and Thomas 2002).

A disadvantage of the slant-stack method is that if the theoretical back-azimuth (or slowness) is not defined correctly, this could lead to misleading measurements of the slowness (back-azimuth).

2.3. Double-beam method

The double-beam method is a combination of slant-stack methods applied to a source and a receiver array. Figure 2.2 demonstrates the advantage of this method in front of the single slant-stack. The combination of beams from a source and a receiver array leads to denser coverage over the area of interest, i.e. provides better imaging resolution.

Scherbaum et al. (1997) used this method to map heterogeneities in the lower mantle. The source array consisted of 18 nuclear explosions from the test site Degelen in eastern Kazakhstan. Data were recorded by the Yellowknife array in northern Canada. Single scattering was assumed. For each grid point the theoretical travel time delay with respect to the P wave is determined, as well as the theoretical source array slowness and back azimuth, and the theoretical receiver array slowness and back azimuth. Each grid point is treated as a candidate scatterer, so the beam is formed for each grid point, and the scattered image is expressed as the resulting beam power. This study resulted in the detection of six anomalous lower mantle phases.

Kruger et al. (2001) used the double beam method to image scatterers associated with the subducting lithosphere in the Mariana subduction zone. Eight earthquakes were used as a source array. The receiver array was chosen to be the Warramunga array in Australia. To compensate for the differences in the amplitudes of the earthquakes (i.e. magnitudes) a phase weighted stack technique was applied. All traces were normalized

with respect to the amplitude of the coda. The imaging was implemented in two steps. In the first one, a rough image of the area was obtained, at a step of 10 degrees in azimuth and back azimuth, and 1s/degree in slowness. The areas that were indicating high scattering were reprocessed with higher resolution, i.e. a step of 2 degrees in azimuth and 0.25 s/degree in slowness. Two scatterers were identified, and interpreted to be related to the penetration of the subducting slab through the 660km discontinuity.

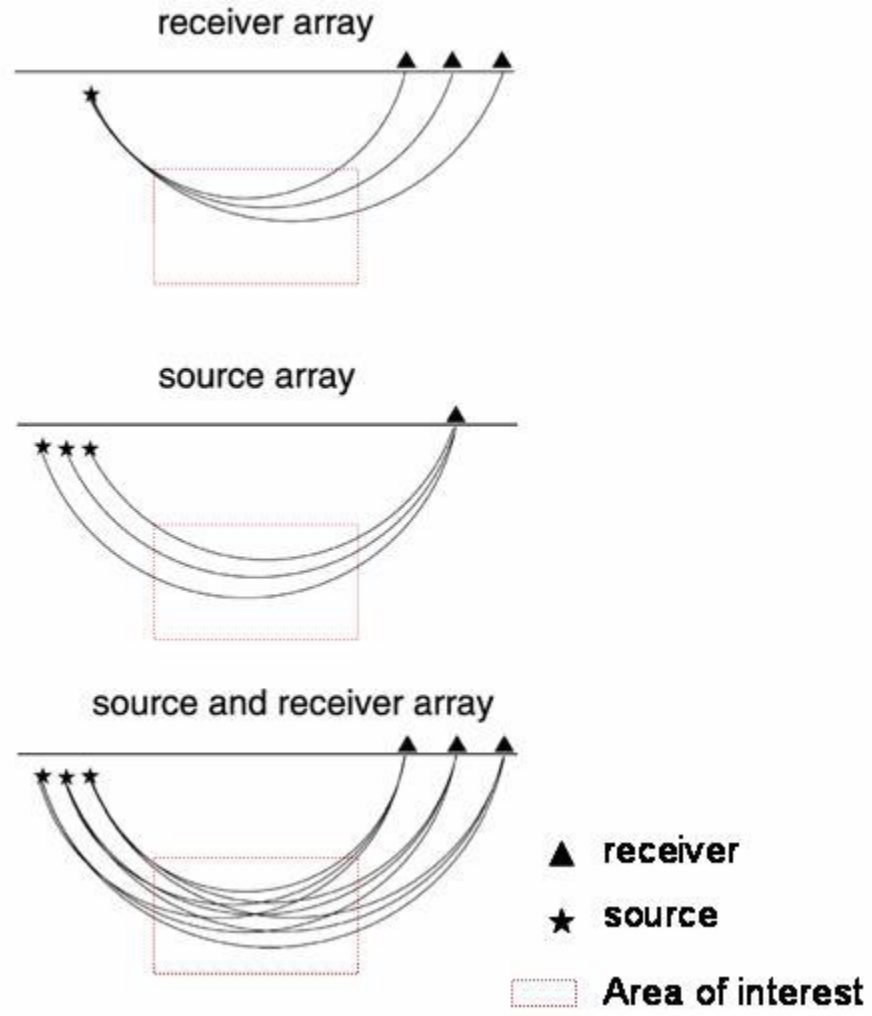

Figure 2.2: Principle of the double beam method. A double beam provides denser coverage of the region of interest. Modified from Rost and Thomas (2002).

One advantage of the double beam method is that it uses information about the travel times, back-azimuth, and slowness, as opposed to migration which uses only travel times. A disadvantage of the method is the assumption for plane waves, which limits its application to teleseismic data.

Rietbrock and Scherbaum (1999) extended the double beam method to overcome that assumption. They used 400 earthquakes triggered during a fluid injection experiment conducted in 1994, in southeast Germany. The receiver array was a temporary seismic network consisting of 71 stations, grouped into seismic mini-arrays, and equipped with 1Hz and 4.5Hz seismometers. For improving the S/N ratio all traces were band pass filtered at 2 and 30 Hz. The total double beam power (DBP) for a possible scatterer D at the location (x,y,z) was calculated as:

$$DBP(x,y,z) = \frac{1}{T}\sum_{\tau=-T/2}^{T/2}\left\{\frac{1}{N}\sum_{n=1}^{N} x_n\left(t+\tau_n^{D(x,y,z)}\right)\right\}^2 \qquad \text{(eq.4)}$$

Where N is the total number of seismograms, τ_n is the whole-path travel time from the source via the scatterer to the receiver for the n^{th} seismogram. In addition, the semblance coefficient was used to detect phases with small amplitudes. This is further discussed in section 2.6 of this chapter.

2.4. F-K method

F-K method stands for frequency-wavenumber method. The f-k power spectral density function $P_{fw}(k,f)$ is defined as the Fourier transform of the autocorrelation function $\langle u(x,t)u(x+x',t+t')\rangle$ of a stationary time series *u(x,t)* (Lacoss et al. (1969) in Sato and Fehler (1998)).

$$P_{fw}(k,f)=\int_{-\infty}^{\infty}\int_{-\infty}^{\infty}\int_{-\infty}^{\infty}\langle u(x,t)u(x+x',t+t')\rangle e^{-i(kx'+2\pi ft')}dx'dt' \qquad \text{(eq.5)}$$

The result is usually presented as a contour plot of the f-k power spectral density (Figure 2.3). The source of seismic energy is a small earthquake in New Mexico. The generation of these contour plots was proceeded by a 2-5 Hz band pass filter of the P-wave data, and 1.3-3 Hz band pass filter of the *S*-wave data. The time interval for the filtered data is 2s and corresponds to the black bars surrounding the direct *P*, *S*, and scattered *S* waves on the seismograms (Figure 2.3a). Data are recorded with eight vertical seismometers. The maximum contour denotes the direction of approach of the wave and the apparent velocity of propagation.

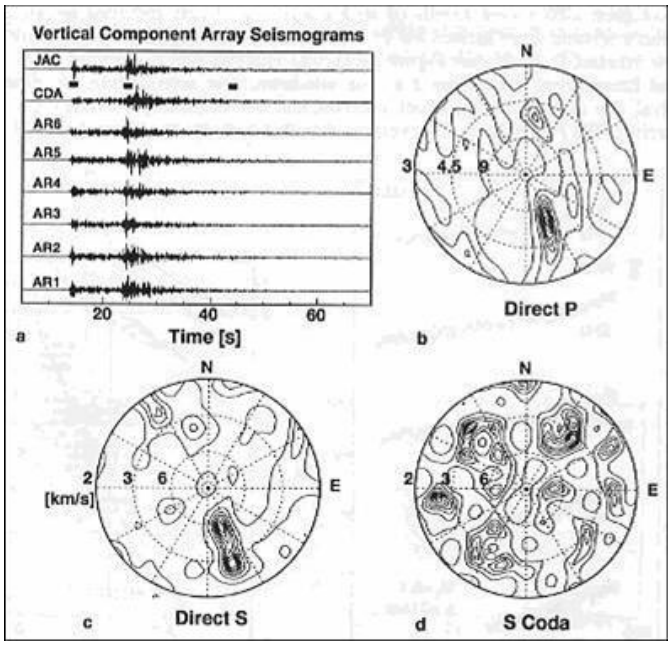

Figure 2.3: (a) Vertical seismograms from a local earthquake in New Mexico; (b) f-k analysis of filtered (2-5 Hz) direct *P*-waves. The numbers correspond to the apparent velocity of propagation in km/s; (c) f-k analysis of filtered (1.3-3 Hz) direct *S*-waves; (d) f-k analysis of filtered (1.3-3 Hz) scattered *S*-waves (after Sato and Fehler 1998).

Similar work was done by Spudich and Bostwick (1987), but the "receiver" array was composed of a cluster of earthquakes, and the "source" was a single station. They processed waves starting at the arrival of the direct *S* wave, in sequential time windows lasting to cover the late coda arrivals. The early coda was found to be represented by *S*-waves multiply scattered near the source (i.e. the seismic station). The very late coda character was not determined because of very low S/N ratio, which is a limitation of the technique. Scherbaum et al. (1991) use the same analysis, and apply it to a set of 12 and 16 earthquakes, and seven seismic stations. Their analysis shows that the early *S* coda has the same slowness vector as the direct *S* waves, while the later scattered waves are leaving in all directions.

One advantage of the F-K method is its applicability to sparse detector arrays. Another advantage is that as opposed to the double beam and slant stack methods, the f-k method measures apparent slowness and back azimuth simultaneously. This is achieved through a grid search calculation over a range of apparent slownesses and back azimuths. In addition, the computation is fast because it is performed in the spectral domain. One disadvantage of the f-k method is that it is applicable to only time windows that contain a single phase. Multiple phases with different slownesses in a time window make the clear identification of the phase impossible (Rost and Thomas 2002). Another disadvantage is that the f-k method is limited to large aperture arrays. The spectral response for a 1Hz sinusoidal wave traveling with a slowness of 7.5 s/deg., and back azimuth of 225 deg. was calculated for a small aperture (Yellowknife, Canada – Figure 2.4a) and a big aperture (Grafenberg, Germany – Figure 2.4b) array. The arrays do not have the same configuration, but the difference in the aperture is much bigger than the difference in the

configuration. The larger aperture array leads to much better resolution in slowness and back azimuth than the small aperture array.

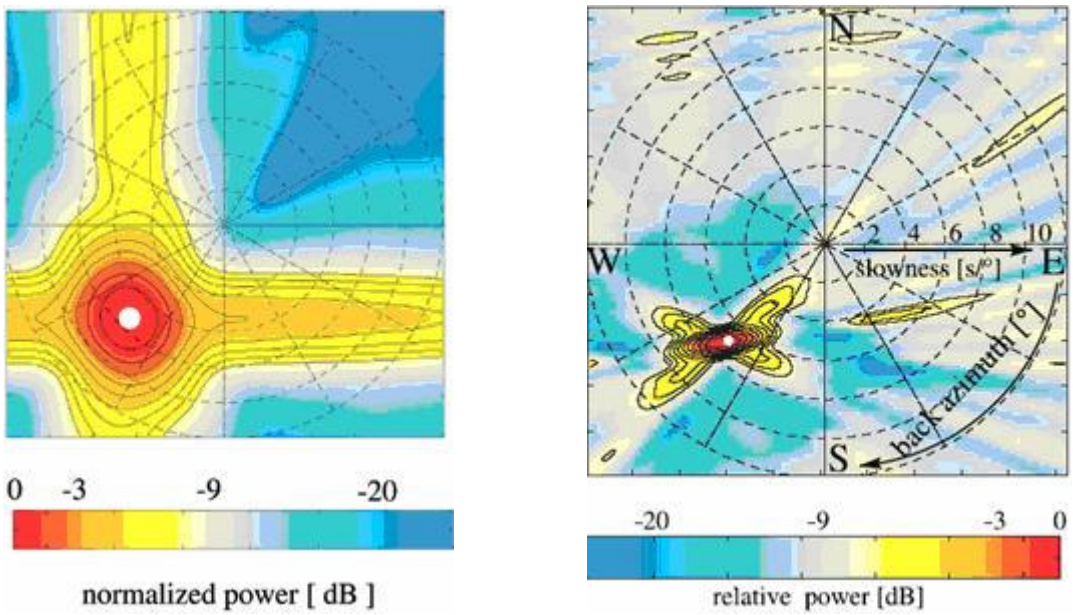

a) b)

Figure 2.4: F-K analysis for two arrays with different aperture. a) small aperture (Yellowknife, Canada) array. The response is computed for a synthetic 1Hz sinusoidal wave traveling with slowness of 7.5 s/deg, and back azimuth of 225 deg. The power spectral density is color coded and normalized to 0 dB. The slowness is displayed on the radial axis, and varies from 0 to 12s/deg, with a step of 2s/deg. The back azimuth is shown clockwise from 0 to 360 degrees. The white circle denotes the maximum in slowness and back azimuth; b) same as (a) but for a large aperture array (Grafenberg, Germany), (after Rost and Thomas 2002).

2.5. Migration

A standard procedure for 3-D imaging when dense source/receiver arrays are available, as in reflection seismology, is migration. Migration is used to project the energy back to its origin increasing the spatial resolution (Yilmaz 1987). It is usually preceded by CMP stacking. In the 2-D case this is the process of sorting of the data into gathers consisting of reflections from the same point (Common Mid Point "CMP"). In the

3-D case, the CMPs include waves from all directions and the sorting is done with respect to a midpoint bin (Figure 2.5). In the ideal case all midpoints will fall in the bin area. These midpoints are used to generate the 3-D CMP gather. The λ/4 criterion is applied to assure that the bin is not spatially aliased. The resolution of a 3-D survey is defined by the bin – the smaller the bin the higher the resolution. The opposite applies to the cost – the smaller the bin the higher the cost (Liner 1999). For this reason 3-D migration was not an option in meeting the objectives of this thesis.

Migration is an inverse procedure – the result is the earth structure that may have been present at the time of passage of the seismic energy. If the velocity v_r of a reflection is known, then the distance h_r (i.e. the depth) to the reflector can be calculated. The exact location of the reflector though cannot be found until the direction of propagation of the reflected pulse is known. In 2-D, migration builds a surface of all points that are at distance h_r from the array. In 3-D, it builds a volume. If the velocity of the medium is assumed constant the volume is an ellipsoid (Figure 2.6). If the velocity varies, the shape of the volume is more irregular. Such a surface/volume is built for all reflection amplitudes, on all traces. When added together, they produce an image of the subsurface. At the location of the reflectors the individual ellipsoids add up, in the absence of a reflector the volumes are random in amplitude and sign and tend to cancel. Migration has an effect on steeply dipping reflectors and does not influence the horizontal ones. One limitation of migration is that its imaging coverage is limited to the midpoint bin coverage.

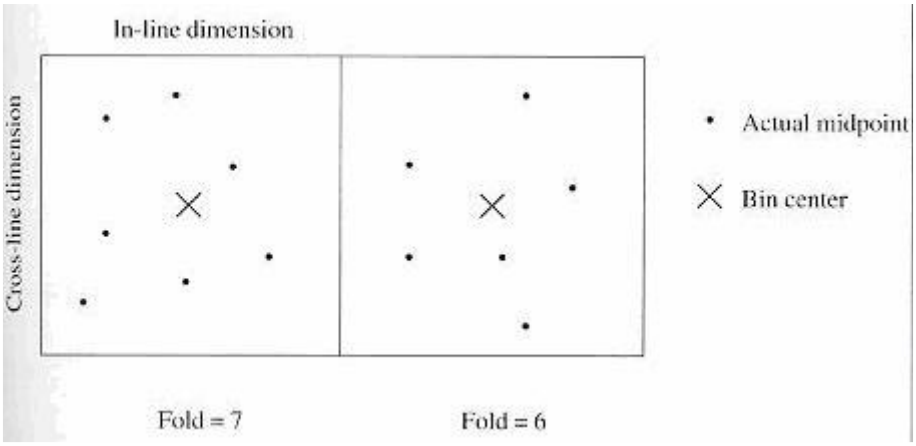

a)

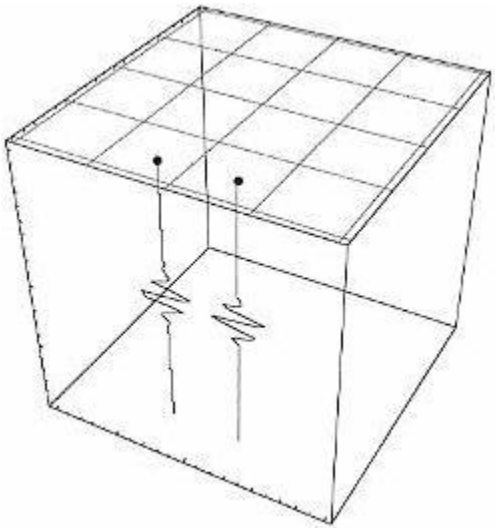

b)

Figure 2.5: The principle of CMP gathering in 3-D imaging. (a) midpoints into a 3-D bin; (b) after the stacking each bin will contain one trace (after Liner 1999).

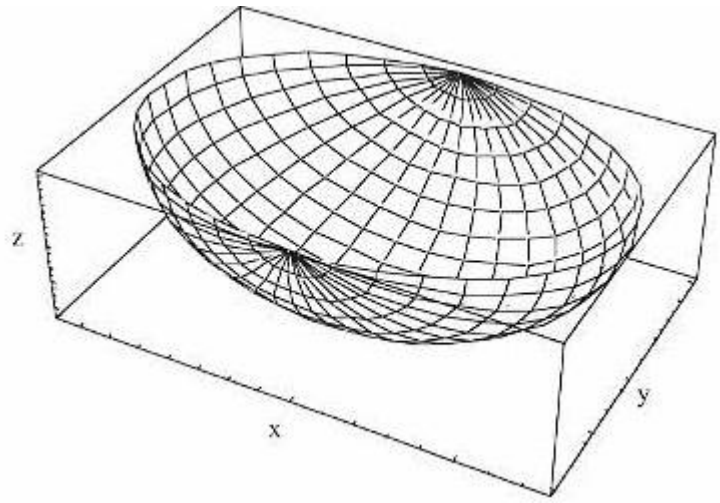

Figure 2.6: Migration ellipsoid. 3-D migration builds a volume of all points that are at distance h_r from the array. For constant velocity that volume is an ellipsoid. If the velocity varies, the shape of the volume is more irregular. Such volume is built for all reflection amplitudes, on all traces (after Liner 1999).

Migration improves the lateral resolution, which is limited by the area of the Fresnel zone. One of the applications of migration is to decrease (significantly) the size of the Fresnel zone. 2-D migration reduces the Fresnel zone along the direction of migration. 3-D migration reduces it in both directions, to the $\lambda/2$ theoretical limit.

There are different kinds of migration. Poststack migration is done to preserve all dipping events in the stack data. It is cheaper than prestack migration, but also less accurate. There is also time migration and depth migration. The output of both could be a depth image, but time migration uses a constant velocity, while depth migration accounts for variation in velocity. It actually considers a 3-D velocity distribution, thus accounting for lateral variations.

A limitation of migration is that in 99% of the cases only *P*-waves are used (Liner 1999). Another major disadvantage of 3-D migration is its cost, which is dictated by the

requirement for dense source-receiver distribution. Adding to this, if there are significant variations in the velocity profile, migration must be repeated a number of times.

Even though migration is usually applied to dense arrays, recently there have been reports for modifying the technique to suit more sparse and irregular distribution of sources and receivers. Loui et al. (2002) used seismograms from 500 local earthquakes, from two earthquake swarms in New Zealand, together with 21 vertical seismometers to obtain three-dimensional images of the epicentral area of a M6.2 earthquake. The sparsity of the source-receiver geometry is due to the big offsets between the seismic stations – on the order of kilometer, as opposed to the offsets between the sources (i.e. earthquakes), which were on the order of hundreds of meters. Single forward and back-scattered *P-P* waves are used in the analysis. Pre-stack depth migration is applied, accompanied with a few techniques to mitigate the imaging artifacts due to poor ray coverage. These include an obliquity factor, trace equalization, and enhancement by resampling statistics. The square of an obliquity factor emphasizes horizontal structures, at the expense of near-vertical structures. Trace equalization was applied for balancing the receiver amplitude and correction for spherical divergence. The resampling was achieved through destroying the trace-to-trace coherence by flipping the signs of data traces. Figure 2.7 shows a set of 3-D images obtained from that analysis. The subducted normal fault is offset of the sea floor and entraps a thick layer of reflective sediments.

Thomas et al. (1999) also report an example of applying migration to a sparse large aperture array. Teleseismic recording from 25 seismometers and 21 earthquakes, recorded by the German Regional Seismic Network and the Grafenberg array were used

in obtaining 3-D images of scatterers in the mantle, at the core mantle boundary, and at the top of the outer core.

In the process of migration the traces are shifted and summed for a large number of receivers, with different shift times, depending on the scattered wave velocities and locations. If the scattered phases have very small slownesses, i.e. very steep incidence, the depth resolution of the migration method is very poor. This is due to the fact that delay times between the receivers will not differ much for different depths, if the angle of incidence is very steep.

2.6. Semblance method

The semblance method consists of calculating the semblance coefficient as a function of azimuth and apparent velocity, and projecting it into a three-dimensional space. The semblance coefficient was defined by Neidell and Taner (1971) as the normalized output to input energy ratio. The mathematical expression is given in Chapter 4. It has been used in a number of imaging studies with earthquake sources. One such study was reported by Nikolaev and Troitskiy (1987). The semblance coefficient was used to study the scattering origin of coherent arrivals, recorded by the NORSAR seismic array. The NORSAR array consists of 22 subarrays that are offset at 20-30km on average, with a total of 132 vertical seismometers. The area of strongest scattering was interpreted to be associated with remains of either magma chambers or magma ascent paths. Both of these structures are considered to be characterized by highly fractured zones, which would trigger significant scattering of seismic energy.

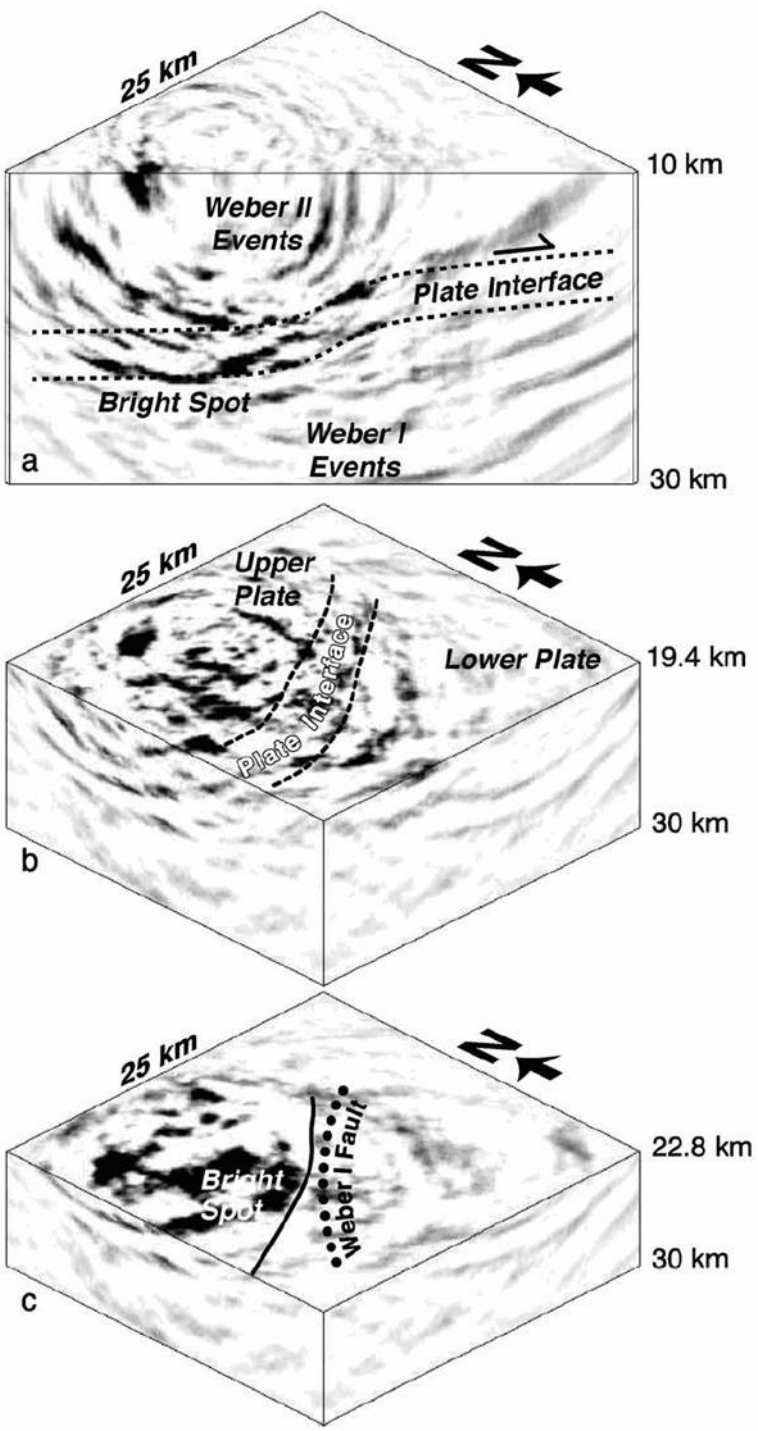

Figure 2.7: Three-dimensional image of the epicentral area of a M6.2 earthquake in New Zealand (February 19, 1990). a) 25x25x20 km volume; b) 25x25x10.6 km volume; c) 25x25x7.2 km volume. The images are obtained through prestack depth migration, using P-P backscattered waves, recorded on 21 vertical seismometers (after Loui et al. 2002).

Three-dimensional imaging of the emission sources in Northern Kanto, Japan was reported by Tchebotareva et. al (2000). Data from six local earthquakes were recorded on 195 three-component seismic stations, with average spacing of 70m. This allowed for the incorporation of both *P* and *S* waves. Data were band passed at 4.5-50 Hz. Even though the geometry of the source-receiver layout was very irregular, the proposed "emission tomography" method identified clear regions of high semblance. These regions coincide with an area of large historical and recent earthquakes, and are interpreted to be due to scattering of seismic waves from a large magma body.

Bannister and Melhuish (1997) used semblance analysis to examine the nature of seismic coda in the Taupo Volcanic Zone. Explosive-generated seismic waves, recorded by a two-dimensional array of 48 surface geophones (14-Hz central frequency), placed on the Kaingarao plateau were used for the analysis. Geophones were separated by 24m; the total dimensions of that receiver array spanned 120x168 m. The array was placed at two different positions, offset at 500m, to obtain larger space coverage. Strong reverberations of seismic energy at or near the source region are interpreted as related to the presence of low-velocity layers of breccia and tuff, interbedded with sheets of high-velocity ignimbrite.

Kuwahara et al. (1997) calculated semblance coefficient for microearthquakes in Tsukuba, central Japan. He used data from 13 seismometers (2 Hz Mark products), with average spacing of 50m (fairly dense array). His results show high semblance for the P-coda, but much smaller one for the *S*-coda. *S*-coda also shows a wide distribution of directions of propagation.

Rietbrock and Scherbaum (1999) extended the double-beam method described in section 2.3, to the case of a non-plane wave propagation and applied it to a set of earthquakes (400), recorded at 71 seismic stations in Germany. They used the semblance coefficient as a measure of the coherence in the scattered waves. The sampling interval of the data was 0.05s, and the seismometers were 1 Hz or 4.5 Hz. Most seismometers were clustered in small arrays, with aperture of approximately 500m. Arrays that did not have high S/N ratio were not used in the analysis, which is a limitation of their technique. Data were band-pass filtered at 2-30 Hz to enhance the S/N ratio for the rest of the arrays. Figure 2.8 shows some of their results. A clear pick in the semblance coefficient is recognized between 9.9 and 10.4 km. This was interpreted as the top of a velocity anomaly defined from previous seismic reflection studies as the Erbendorf Body.

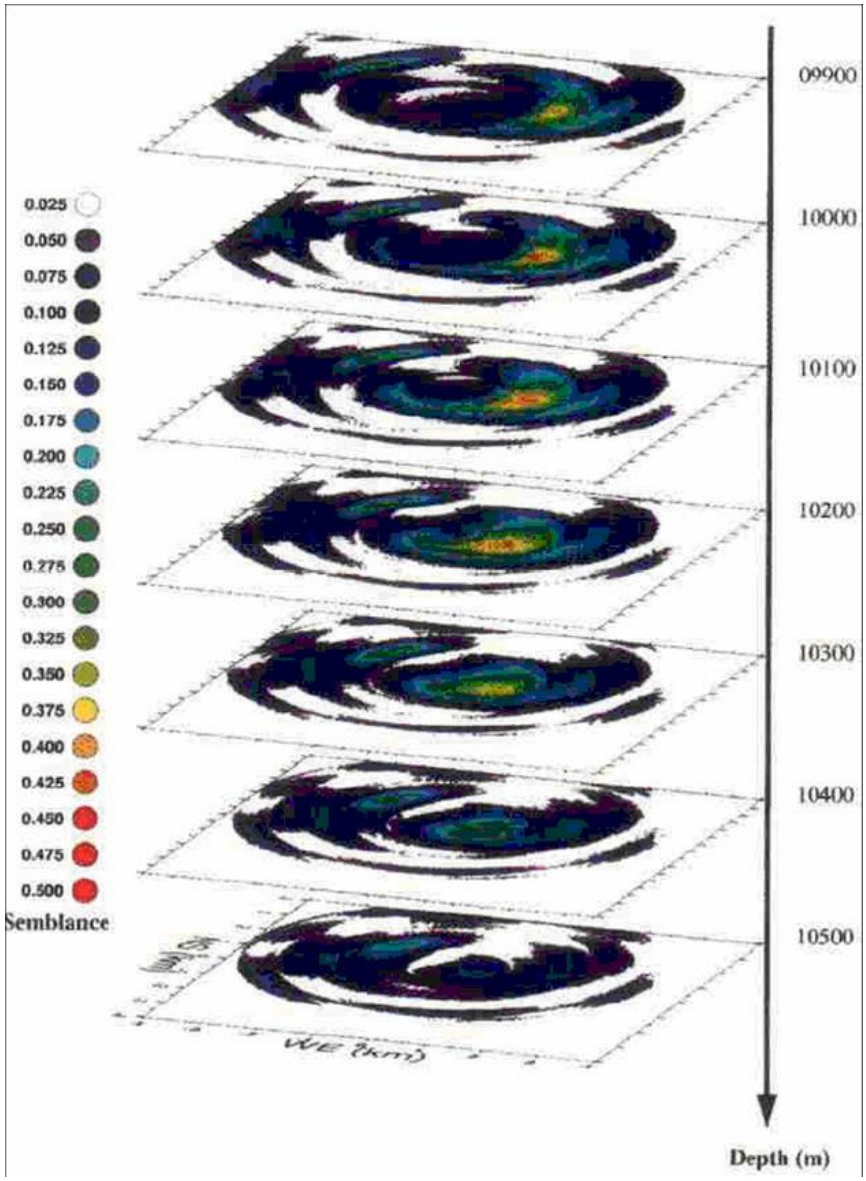

Figure 2.8: Depth distribution of the semblance coefficient for a small seismic array in Germany. Red values of the semblance coefficient correspond to coherent arrivals; the white values indicate random noise (after Rietbrock and Scherbaum 1999).

2.7. Shallow seismic imaging

Reflection methods developed by the petroleum industry have been modified over the past 30 years to suit the needs of shallow seismic studies (Lanz et al. 1996, Hunter et al. 1984, Miller et al. 1989, Bachrach and Mukerji 2004, Schtivelman et al. 1998, Baker et al. 1999, Spitzer et al. 2003, Buker et al. 1998). These studies usually target the upper 100-150 m of the subsurface, and are a potential tool for environmental and engineering site characterization. Shallow seismic reflection (SSR) was first reported by Schepers (1975, Germany). A couple of years later Hunter and Hobson (1977) reported observed shallow reflections during a refraction experiment conducted in North America. This set the beginning of quick development in shallow seismic reflection studies. SSR techniques today face two major challenges related to the complexity of the near surface structures. The first one is the interference of shallow reflected waves with other source-generated coherent noise such as ground roll, or airwaves. Hunter et al. (1984) proposed the optimum window technique for optimizing the time separation between the direct and surface waves. In addition to the optimum window, there are a number of different techniques developed to suppress ground roll. One is through frequency filtering. It is efficient only if surface waves have very different frequency than the reflected waves. Another way is to apply an AGC (Amplitude Gain Control) function, or to use a low-cut filter prior to analog-to-digital conversion (Miller et al. 1989).

The second challenge for SSR is the high cost associated with obtaining three-dimensional high resolution images. It is defined by dominant frequency, shot-receiver spacing, timing accuracy, and accuracy of calculated average velocities. Sub-meter resolution images have been obtained, but at a very high acquisition cost (Lanz et al.

1996, Buker et al. 1998). For example, Buker et al. (1998) report that it took 85 days and a crew of five to eight people to obtain a 432x357m 3D high-resolution reflection cube. In addition, the seismic wavelength must be small enough to enable target resolution (Bachrach and Mukerji 2004). Extensive signal processing usually follows the acquisition. In order to obtain a high-resolution 3D cube Bachrach and Mukerji (2004) had to apply band pass filter, first-arrival mute, NMO corrections, 3D binning, 3D stacking, and trace mixing to the data. Compared to this, the semblance method described in this thesis has minimal signal processing; it can be applied to a sparse array, i.e. does not have the resolution of the migration method, but has much lower cost; it can provide much broader coverage than migration (which is usually the technique used for shallow seismic surveys). The coverage of migration is limited by the coverage of the midpoint bin, while the semblance method coverage extends far beyond the source-receiver layout.

Table 2.1: Comparison of the different methods used for three-dimensional imaging

METHOD	ADVANTAGES	DISADVANTAGES
Slant-stack	Applicable to sparse arrays; Uses back-azimuth and slowness information, as addition to travel times	**Plane wave assumption; sensitive to wrong theoretical back-azimuth or slowness; calculates the back azimuth and the slowness separately**
Double-beam	Uses back-azimuth and slowness information, as addition to travel times	**Plane wave assumption; calculates the back azimuth and the slowness separately**
Frequency-wavenumber (f-k)	Applicable to sparse arrays, large aperture arrays; calculates the back azimuth and the slowness simultaneously; fast computation since it is performed in the spectral domain	**Sensitive mainly to waves with vertical incidence; plane wave approximation; limited in resolution for small aperture arrays; applicable only to time windows containing a single phase**
migration	Provides very high resolution images; enhances steeply dipping reflectors without affecting the horizontal ones	**Requires dense arrays; image coverage is limited to the CMP bin, i.e. smaller than the size of the source-receiver layout; only P-waves are used in most cases; based only on travel time information; poor depth coverage for small slownesses, i.e. steep incidence angles**
semblance	Applicable to sparse arrays; image coverage extends far beyond the source-receiver layout; calculates the back azimuth and the slowness simultaneously; applicable to time windows containing multiple phases	**Plane wave assumption; lower resolution**

CHAPTER 3

EXPERIMENT DESIGN

Before a survey begins, it has to be designed to provide the best quality data for achieving the objective of the research. Factors that affect that quality include type of equipment, acquisition parameters, and choice of a test site. Before designing a survey, the first step is to clearly state its objective. The following four sub-sections of this chapter describe the steps taken in designing this experiment.

3.1. Step 1 – Define the objective

The general objective of this work was to develop and test a technique for imaging shallow scatterers in crystalline rock. The technique had to be non-invasive for protection of the environment, and economical. The ultimate goal was to obtain 3D images of the upper few tens of meters of the subsurface, and test the technique in different environments (a rock outcrop, and a soil site). One application of the technique is the detection of water bearing fractures. For this reason, an ideal environment for testing the semblance analysis is one with well-known distribution of shallow-water bearing fractures.

3.2. Step 2 – Choice of equipment

The three main components in the equipment for any seismic survey are: the source, the receivers, and the data acquisition system. Typical data acquisition systems for digital data consist of an amplifier, A-D conversion board, and a data storage unit.

The choice of each of these components is defined by the objective of the research and the resolution needed to achieve this objective. All acquisition parameters are summarized in Table 3.1.

Seismic source

The seismic source provides a sudden release of energy that causes rapid dynamic stressing of the surrounding medium. Seismic sources are characterized by their energy level and frequency characteristics. There are three main types of seismic sources for land use – impulsive (dynamite), vibratory (Vibroseis), and impact (weight-drop). The use of dynamite can be very damaging to the environment. Also, dynamite requires special permission, storage, and transportation, which all lead to an increase in the cost (Sheriff and Geldart 1982). Since our objective was to develop a technique that is environmentally friendly and economically efficient, dynamite was ruled out as a possible source. The vibratory type of source is environmentally friendly, but is also too costly as it is used in large-scale surveys, sampling hundreds of meters to several kilometers in distance. This limited our choice to a weight-drop source. It is not harmful to the environment and there is no additional cost associated with its use. The weight-drop consists of a weight that drops on the ground or strike plate. The simplest weight drop is a 2-4 kg sledge hammer, used when the survey area is not bigger than a few tens of meters in diameter. The source used in our survey is shown on Figure 3.1. It was designed as a hollow metal cylinder with diameter of 0.11 m, height of 0.32 m, and weight of about 5 kg. The cylinder slides down a metal pipe (2.54 cm in diameter), and strikes a plate attached to two metal bars. The operator may stand on the metal bars or weights may be applied to them to improve coupling. It is dropped from about half a

meter height. Elastic bands are utilized to accelerate the mass to simulate a higher drop height. The entire source can be placed on a base. The material of the base is chosen depending on the desired frequency content of the data. For example, a metal base would produce higher frequencies than a wood base. If no base is used, the frequency content is defined by the land surface where the force is applied. For the data acquisition on the outcrop no base was used. The granite was a natural base for generating high frequency waves. In the second experiment, on the soil site, we used a rubber base.

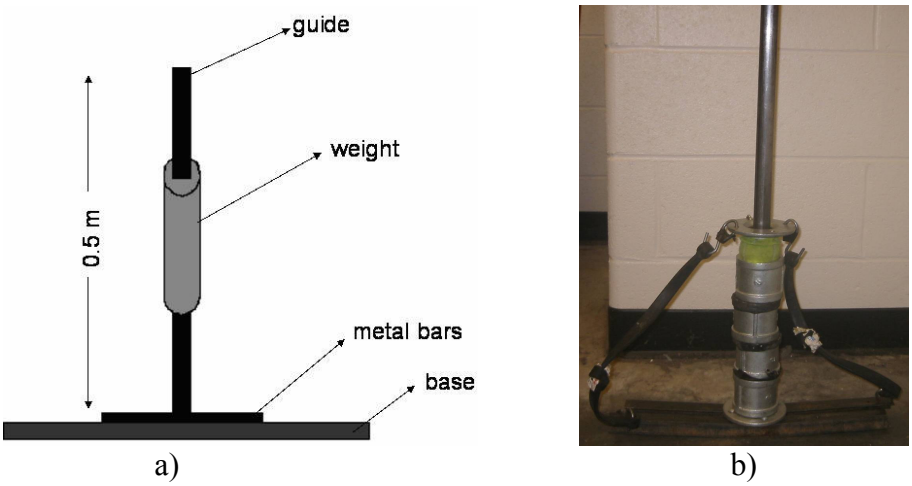

Figure 3.1: Weight-drop source. a) Schematic view – the weight (about 5 kg) is a hollow metal cylinder, sliding down a metal guide (pipe), from about 0.5 m height. It falls on two metal bars. The entire source is placed on a base, which could be made of rubber, wood or metal; b) a picture of the source.

Seismic sensors

The next important components in the seismic equipment are the receivers. For controlled source (active) seismic surveys, the most popular type of receiver is the geophone. It is preferred mainly because of its portability. The modern geophones are of electromagnetic type (fig.3.2a). A cylindrical coil is suspended from a spring support in the field of a permanent magnet. The magnet is attached to the instrument casing. The

suspended coil represents an oscillatory system with its resonant frequency determined by the mass of the coil and the stiffness of its spring suspension. A shunt resistor is connected across the coil terminals to control the damping of the oscillatory motion of the coil. If the coil moves relative to the magnet, voltage is induced and current will flow in the external circuit. The voltage is proportional to the rate of change in

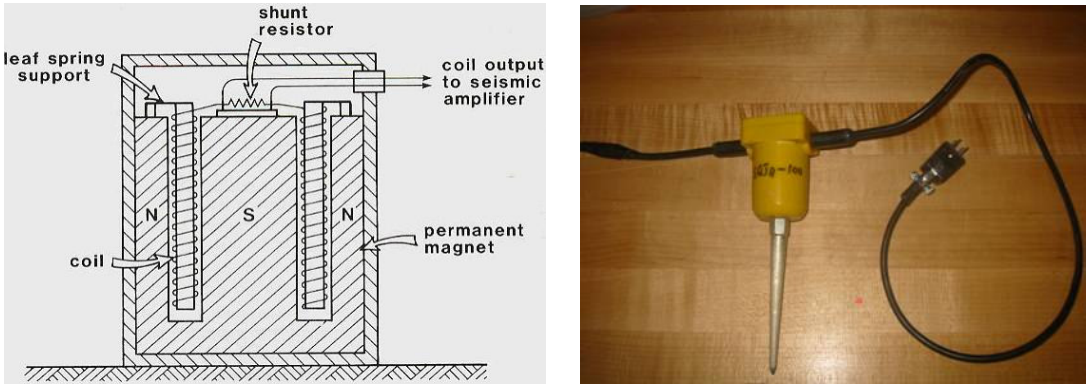

a) b)

Figure 3.2: Vertical geophone. a) schematic view – a coil is wound around a magnet, attached to the casting. The relative movement of coil with respect to casting induces voltages (Kearey and Brooks 1991); b) picture of the geophones used in our survey.

the magnetic flux inside the coil, and for frequencies they have a flat frequency response to particle velocity above the natural frequency. For a vertical geophone the coil is oriented so it is constrained to vibrate only vertically. This gives maximum sensitivity to P waves, as well as to vertically polarized S waves, and Rayleigh waves. For a horizontal geophone the coil is oriented so it is constrained to vibrate only horizontally, making it most sensitive to horizontally polarized S waves, and Love waves. In addition, every geophone is designed with a certain frequency response. In most seismic reflection exploration applications the compressional waves of interest are in the 15 to 60 Hz range. For reflection data the conventional geophone has a natural frequency of 15 Hz so that the response is flat to particle velocity above 15 Hz. Hence, surface waves (ground roll)

which are in the range of 1 to 10 Hz from the large explosions used in seismic reflection exploration are suppressed. In near-surface reflection seismic data acquisition, higher frequencies are required to give a finer resolution. In this study, 100 Hz geophones were used (response curve shown in Figure 3.3). Frequencies below 100 Hz fall off at 12 dB per octave. We used sixteen vertical geophones (Figure 3.2b).

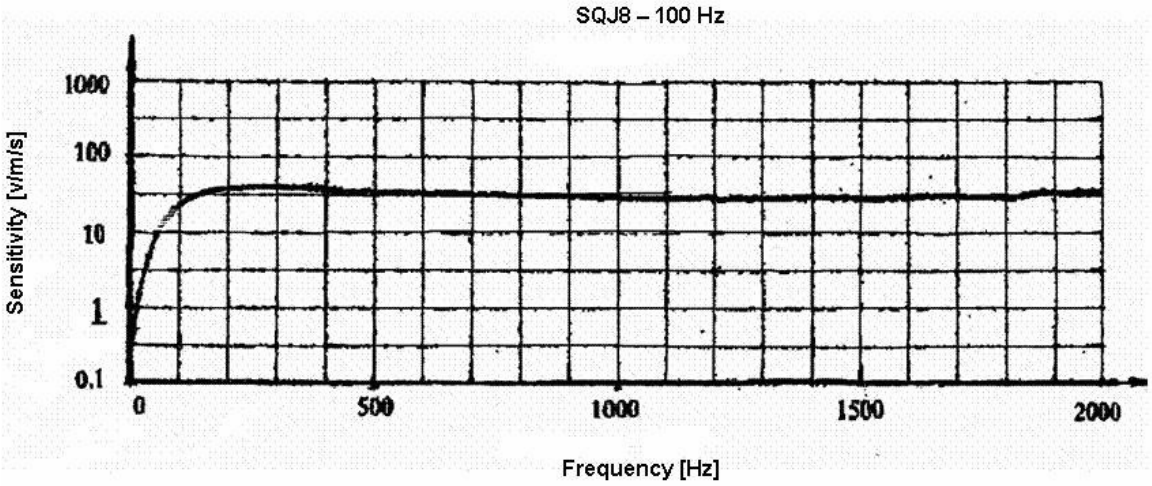

Figure 3.3: Response curve of the vertical geophones, used in this survey. Frequencies below 100 Hz are attenuated. All signals between 100 Hz and 2 KHz are passed.

Data acquisition system

The energy released by the source reaches the geophones and is converted to an electrical signal. This signal goes to a data acquisition system. The data acquisition system performs a number of functions. It amplifies the signals through a parallel set of 16 amplifiers, and converts them to digital form through an analog-to-digital converter (ADC). There are two parameters that are important here: the sampling precision (dynamic range) and the sampling frequency. The choice of each of these parameters is defined by the objective of the research and the environmental conditions for the data acquisition. We planned on using an impact type of source, applied to the earth surface.

This meant that some very strong surface waves could be generated. Because our weight-drop source was not very powerful, we expected the amplitude of the scattered waves to be small compared to the amplitude of surface waves. This implied that we needed an acquisition system with large dynamic range. We used a 16 bit digitizer.

The second important parameter is the sampling interval, or time between successive digital samples. The minimum sampling interval is defined by the highest frequency of interest. On the other hand, when a single digitizer is multiplexed, the sampling rate of a single channel is defined by the maximum sampling rate divided by the number of channels in the system. We had sixteen channels and were interested in recording frequencies over a few hundred Hertz. The required switching rate of an ADC is defined by the sampling interval and the number of channels. The ADC board used in this research was Keithley (KPCMCIA-I6AI-C). This is a 16 channel 16-bit board. The 16 analog channels are sequentially scanned at a frequency of 100 kHz (i.e. switching rate of 10 μs). This way every channel is sampled every 0.16 ms, i.e. the channel sampling frequency is 6250 Hz (Chen and Long 2004). Sampling at this rate preserves all frequencies up to 3125 Hz (the Nyquest frequency).

The last function of the acquisition system is to store the data. Because the dynamic range of the digitized data is determined only by the length of the binary word, the only limitation on the dynamic range will be the number of bits recorded. This is directly linked to the speed of recording and the available data storage. We used a Dell Inspiron 2650 field laptop, with 1.8 GHz CPU, 256 MB RAM and 37 GB of hard disk. The small number of channels and the short duration of the seismic records (0.67 s) allowed us to use this very cost efficient data storage unit.

The software used to acquire, analyze and then display the data was the Georgia Tech seismic acquisition program GT-SDAP (Chen and Long, 2004), developed for refraction and reflection studies of modest size field sites (source – sensor separation of up to 100 m). The program allows data files to be reviewed, edited, filtered, and converted to one of the two standard formats – Seismic Unix (SU) or SEG-Y. In this study the program was mainly used for the acquisition of the data, and some basic processing (removal of DC offset). The seismic data files are written as an ASCII format header file and a binary data array attached to it (Chen and Long 2004).

Table 3.1: Acquisition parameters for 3D imaging of scatterers

Item	Parameter
Source	**5 kg metal weight**
Source spacing	**max 70 m**
Receivers	**100 Hz vertical geophones**
Receiver geometry	**Circular array, 15 m aperture**
Number of channels	**16**
ADC board	**Keithley (KPCMCIA-16AI-C)**
Sampling precision	**16-bit**
Dynamic range	**90.3 dB**
Switching rate	**10 µs**
A/D conversion time	**8 µs**
Sampling interval for one channel	**0.16 ms**
Record length	**0.67 s**
Data storage unit	**Dell Inspiron 2650; 4-M CPU 1.8 GHz; 256 MB RAM; 37 GB Hitachi_DK23EB-40**

3.3. Step 3 – Field site

In every field acquisition of data, it is highly desirable to have a quiet environment, with nearly no urban noise. In addition, the choice of a field site is defined by the objective of the research. For the testing of the technique, we chose Panola Mountain Research Watershed (PMWR) located about 25 km SE of Atlanta, GA. PMRW is part of the Georgia Piedmont, which is known to be underlain by fractured and unweathered crystalline rock (Williams L. 2003). The area is about 41-hectare, of which 93% is forested and 7% are granite outcrop (Figure 3.4). Maximum altitude of the area is 279 m above sea level and the relief is 55 m. The Panola granite has granodiorite composition. The granite was intruded into a hornblende biotite gneiss which also occurs as inclusion within the granite (Peters et all. 2000). We chose this site for a number of reasons:

- PMRW is closed to the general public, which significantly reduces the urban noise.
- Our study was aiming at imaging shallow scatterers, which could be water productive fractures. PMRW is part of Rockdale county, an area that was subjected to a detail study of its water bearing features, conducted by USGS (Williams and Burton 2005). The objective of Williams and Burton (2005) was to assess the depth, nature, and yield of fractures, joints, weathered veins, and faults as potential pathways for underground water. Data from a few geophysical logs show several different water bearing features. The most common are the steeply dipping joints. They play major role in providing vertical pathways for water into and out of the bedrock. Sheet fractures (or stress-relief fractures) are observed at several wells as well as on the surface of the

outcropping of unweathered granite. These are nearly subhorizontal openings, usually ten to several tens of meters below the saprolite-rock interface (Williams and Burton 2005). Such fracture was observed at Panola well 155. The depth to the fracture is 22.5m. We chose that well to be the location for testing the technique at a soil site. This is field site 3 on Figure 3.4. The experimental layout of the data acquisition is shown on Figure 3.5.

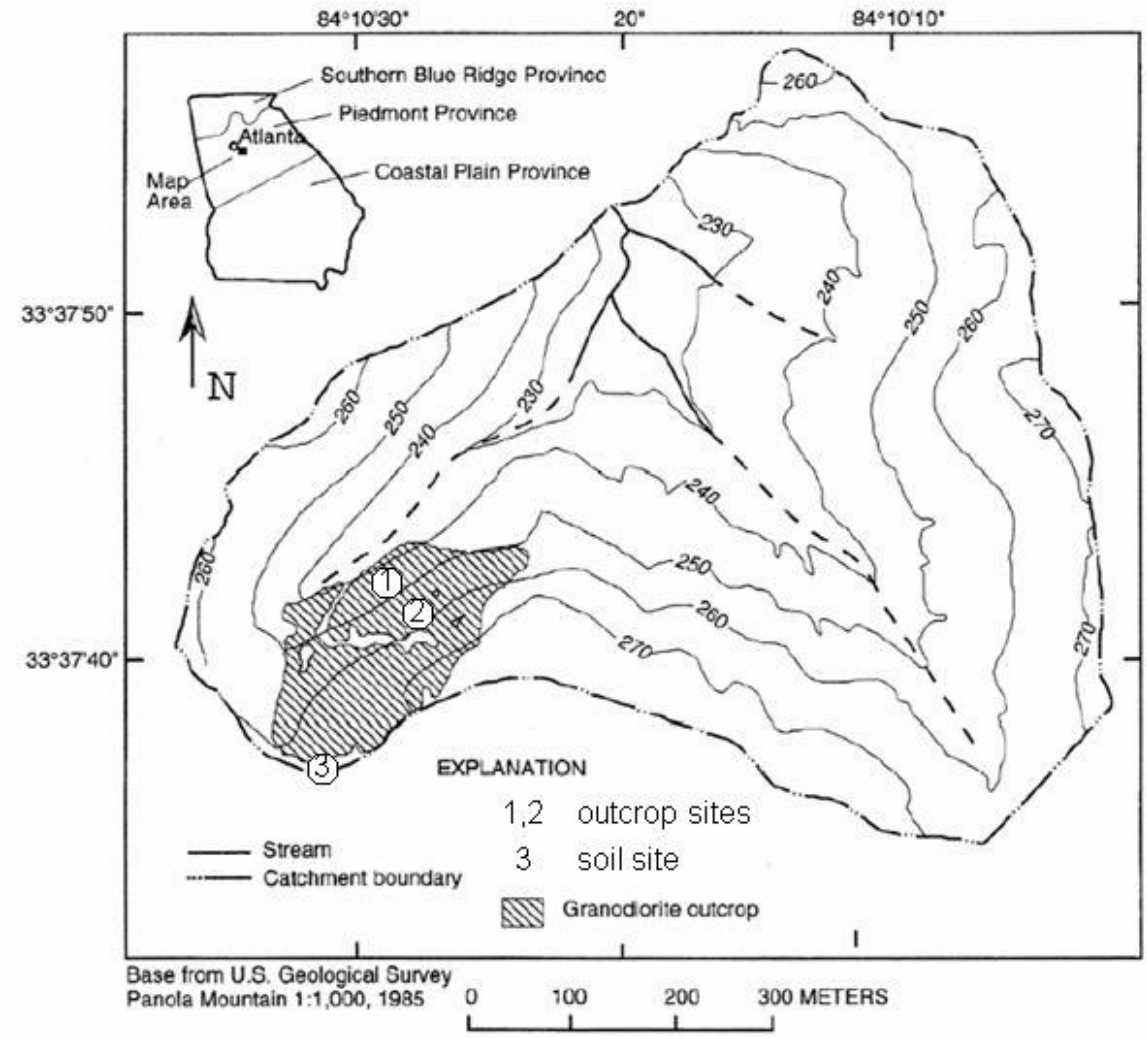

Figure 3.4: Map of Panola Mountain Research Watershed. The grey area shows the granite outcrop. The numbered circles denote the locations of our geophone arrays. Two experiments were conducted on the outcrop (circles 1,2), and one on a soil site (circle 3). Adopted from White et al. (2002).

- The existence of a small granite outcrop was another advantage of PMRW. When data are acquired at a soil site, and a weight drop source is used, not only very strong surface waves are generated but they also exhibit dispersion. Dispersed surface waves could interfere with waves scattered from shallow fractures. This could result in adding noise to the images of the subsurface scatterers. We expected to reduce the amount of dispersion by acquiring data on the rock.

3.4. Step 4 – Experimental layout

The size, spacing, and orientation of the geophone array must be selected on the basis of the properties of the noise to be cancelled and the desired resolution (Kearey and Brooks 1991). Every vibration that is not part of the signal is termed noise which can be either random or coherent. Random noise comes from highly variable sources including the movement of people near the geophones, wind moving vegetation, coupling with the ground, stones ejected from the source, ocean waves beating on seashore and so on. It is usually possible to suppress random noise by stacking. The coherent noise is "shot generated" (Kearey and Brooks 1991, Sheriff and Geldart 1982, Telford et al. 1990). It comes as surface waves (ground roll), multiples, waves reflected from near-surface irregularities and inhomogeneities, such as boulders, or small faults and so forth.

The geometry of the array affects differently waves traveling from different directions. If the geophones are placed along a line, equally spaced, a wave traveling horizontally will reach each geophone at a different time, so if the records are vertically stacked, there will be a certain degree of destructive interference. On the other hand, if the wave approaches the surface in vertical direction, it will arrive at each geophone

simultaneously, so the outputs will combine constructively. Areal arrays may be used to suppress horizontal noise coming from different directions, and to amplify vertical signal coming from different directions. This was our motivation in choosing a circular array. Such geophone geometry will enhance coherent signal coming from a full range of azimuths and suppress horizontal noise coming from all direction.

In addition, a seismic survey is designed to provide a specified depth of penetration and subsurface resolution, both vertical and horizontal. The vertical resolution is a measure of the ability to recognize individual closely spaced reflectors (Kearey and Brooks 1991). The maximum vertical resolution is defined as a quarter to one eight of the wavelength of the reflected pulse. In our survey the central frequency of the recorded signal was 400 Hz for the outcrop data, the velocity of P waves was 4400 m/s, hence the wavelength of scattered P waves was 11 m. We chose a very conservative estimate of vertical resolution – three meters. The horizontal resolution for a flat lying reflector is one half of the spacing between geophones, which in our case was 1.5 m. These estimated limits of the vertical and horizontal resolution were taken into account in choosing the cell size for generating the images of subsurface scatterers.

We first tested the technique at field site 1 (Figure 3.4, and 3.5a). The geophones were placed in a near circular array, with aperture of 15 m. The array was located 15-20 m above a small creek, running at the bottom of the outcrop (Figure 3.6, blue triangles and stars), where we expected to see some strong surface wave scattering. The source was moved around the array clockwise, at distances of 10 to 50 m. Because the rock could not be drilled, a non-invasive technique was needed to secure the geophones to the outcrop. Initially, we moulded small cement platforms on the rock and attached the

geophones to the cement. This did not provide sufficient coupling. We observed undamped resonances in the range of 200 to 800 Hz. (Figure 3.7a). Sandbags used to cover the geophones were only partially successful at reducing the resonances (Figure 3.7b). Our best results were obtained by using modeling clay to attach the geophones to the rock and cement platform and by covering the geophones with sand bags. We used about 3kg of sand per geophone. This gave us significant reduction of the undamped resonances and we were able to register seismic signals with reasonable quality (Figure 3.7c). A few traces developed resonances during the field test. These may have been caused by the clay drying out and the geophone breaking loose. We excluded six traces, to assure that the results will not be contaminated by undamped resonances.

The initial images of scatterers, obtained from this experiment showed a strong zone of scattering associated with the creek, and two others, about 40-50 m from the array in E65S direction. This led to the decision to conduct a second test. The second array was placed near the E65S scattering areas (Figure 3.6, and 3.5b, green triangles and stars). The source was moved in parallel lines, with 10 and 20 m offsets.

To test the limitation of the technique when applied to two different environments we conducted a third test at a soil site near well Panola155 (Figure 3.5c). The geometry of the array was preserved as in the previous two tests. Most of the geophones were placed on a cement trail, yet some were on soil. The source array consisted of three parallel lines, at offsets of 10m. The source was moved at distances of 5m. The well was located about 18m from the geophone array in S62W direction. The data from the semblance imaging were compared with log data from Panola155.

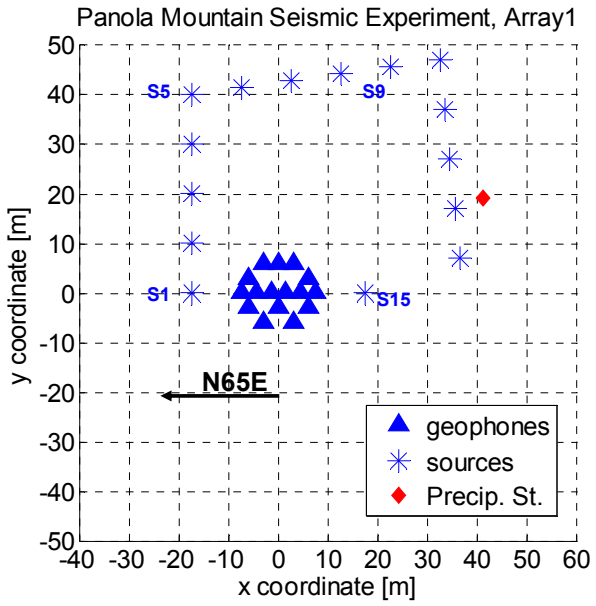

a)

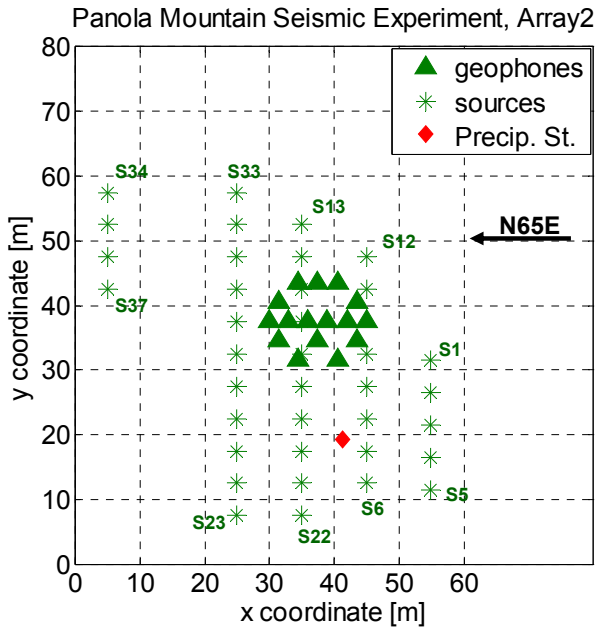

b)

Figure 3.5: Experimental layout of the three arrays. Geophones are denoted by triangles and source positions are denoted by stars. (a) Array1 –The notation S1…S15 stands for source#1 to source#15, the red diamond shows the position of a precipitation station; (b) Array2 - The notation S1…S37 stands for source#1 to source#37, the red diamond is again the location of the same precipitation station; (c) Array3 - The notation S1…S29 stands for source#1 to source#29, the green cross denotes the location of the USGS well.

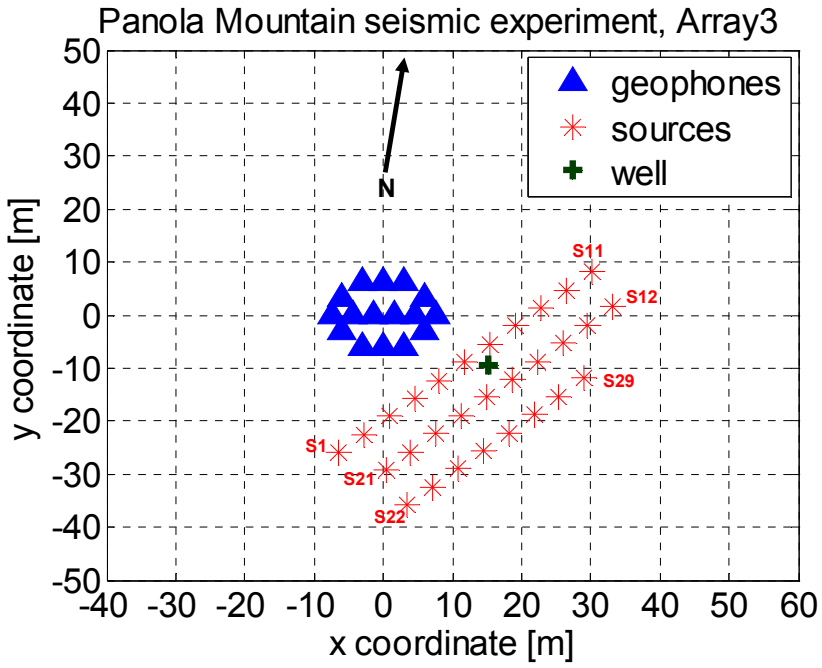

c)

Figure 3.5: Continued

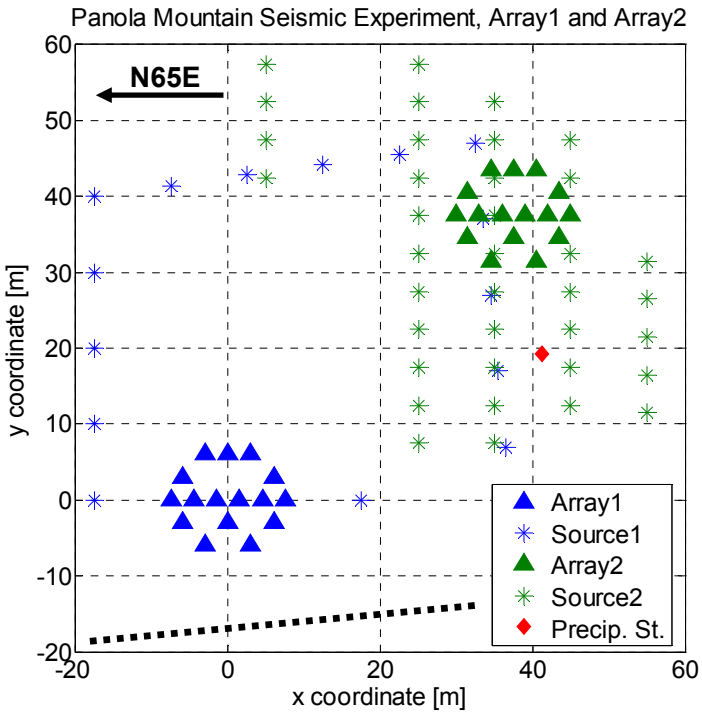

Figure 3.6: Experimental layout for the outcrop data acquisition. This experiment was conducted in two phases. First, the geophones (blue triangles) were placed in a near circular array, and the source (blue stars) was moved around the array clockwise, at distances of 10 to 50 m. In the second phase, the geophones (green triangles) were placed in the same near circular geometry, and the source (green stars) was moved around the array at parallel lines. The dashed line represents the approximate location of a small creek, running at the bottom of the outcrop.

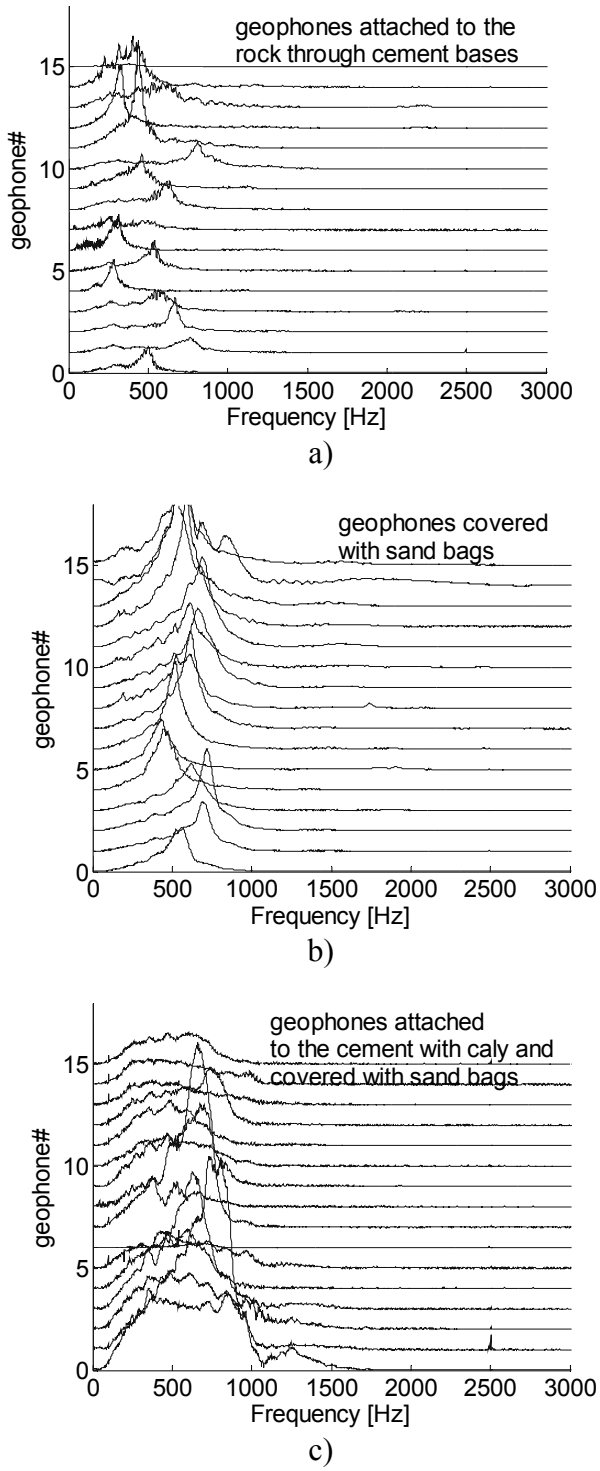

Figure 3.7: Spectrum of the recorded seismic data during the first test (Array 1). Amplitude is normalized to the maximum amplitude for each geophone. a) geophones are attached to the rock only through cement bases. b) geophones are covered with sand bags (about 3kg per geophone); c) geophones are attached to the rock through clay and cement bases, and also covered with sand bags.

CHAPTER 4

SEMBLANCE ANALYSIS

4.1. Introduction

When seismic energy propagates through real medium, the signal trajectory is distorted by the velocity heterogeneity, but the spatial coherence of the signal is preserved. Such spatial coherence is expressed as a correlation of the propagating energy from channel to channel if data are recorded by a seismic array. The idea of employing a correlation-like technique to a set of seismic traces in order to look for coherence in the emerging seismic wave field was first proposed and used by Rieber (1936). He developed a system of "controlled directional sensitivity" that targeted sharply folded and faulted regions. Two components of direction were recorded on sound track records, which were then fed through an "analyzer". The role of the "analyzer" was to break down the complex seismic record, by optical and electrical adjustments. In this way individual waves coming from a specific direction are enhanced, and waves coming from all other directions are suppressed. The raw seismic record was run through this "analyzer" multiple times, as every time the maximum sensitivity factor of the system was directed toward a different azimuth. This is, perhaps, the first published method for identifying waves coming from different azimuths. Later Simpson (1967) proposed a similar technique called the "traveling" S/N ratio method. He calculated the S/N ratio for overlapping or adjacent time intervals. His method predated extensive use of computers (computers in oil industry did not come in general use until very late 60's and early 70's) and was developed for analog equipment. The work of Simpson was followed by the

"velocity spectral display" method of Tanner and Koehler (1969), for identifying primary reflections and stacking velocities. This method is based on the application of a multichannel filter (called by the authors – semblance filter) to generate the common signal power as a function of incidence time and apparent velocity. The semblance filter is applied to the seismic records for a sliding time window and a range of apparent velocities. This is, perhaps, the first paper that introduces semblance as a coherency measure. Neidell and Taner (1971) introduced the concept of semblance in more detail, compared to other similarity measures, such as un-normalized cross-correlation, and summing (also known as stacking). The test was performed for two noise-free coherent signals, having 40ms Ricker wavelets. Calculations were performed with a 12 ms time step, and a 50ft/sec. velocity increment. Sampling rate of the data was 4ms. It was found that out of the three measures of similarity, the semblance coefficient had the best performance for resolution and parameter identification, for this specific test case. In addition to this work, Douze and Laster (1979) presented the first discussion on the statistical properties of semblance. Their research is discussed in more detail in section 4.5.

In this thesis I use the definition of semblance proposed by Neidell and Tanner (1971) to calculate the semblance coefficient as a function of arrival time, apparent velocity, and azimuth (section 4.4). The analysis is applied to three sets of seismic data. The first two sets were acquired on a rock outcrop (Array1 and Array2), and the third one was acquired on a soil site (Array3). The exact geometries and locations of the three arrays were discussed in Chapter3, and shown on Figure 3.5. Further, we investigated the effects of different factors, such as resonance noise, width of the time window, and

frequency filtering, on the computation of the semblance coefficient (section 4.5). The results of this evaluation were critical in preparing the data for the imaging algorithm (Chapter 5). Different processing approaches had to be developed for the different arrays, due to the different quality and characteristics of the acquired data. The output of the semblance analysis is later used to generate 3-D images of the distribution of scatterers for the areas where the three arrays were placed (Chapter5).

4.2. Description of the semblance algorithm

The semblance coefficient was defined by Neidell and Taner (1971) as the normalized ratio of the output to input energy:

$$S(\alpha, v) = \frac{\sum_{j=1}^{T} \left(\sum_{i=1}^{N} f_{ij}(\tau_i) \right)^2}{N \sum_{j=1}^{T} \sum_{i=1}^{N} f_{ij}(\tau_i)^2}, \qquad \text{(eq.4.1)}$$

Where α is the azimuth or direction of propagation of the wave, v is the velocity of propagation, f_{ij} is the amplitude of the i^{th} trace at the j^{th} time, τ_i is the time shift applied to the i^{th} trace to correct for moveout (defined by the apparent velocity v and the azimuth α), T is the duration of the time interval in number of data points, and N is the number of channels used in the analysis. Three main assumptions are made in the calculation of the semblance coefficient S: (1) plane wave propagation; (2) elastic waves; (3) all noise is random, i.e. the noise sum over all channels is zero. The value of the semblance coefficient varies between zero and one. A value of one would mean that all incident energy is transmitted, i.e. there is no loss of energy. A value of zero means there is no coherent signal present.

For every source position and time interval in the seismic trace we calculate the semblance coefficient as a function of apparent velocity and azimuth. Azimuth is referenced to the direction of propagation. The algorithm for this calculation is described in Table 4.1, in the form of a flow chart. The computation consists of four main steps. The first step is to read the raw seismograms in seismic unix format. In the second step a number of input parameters are introduced, some of which are acquisition parameters (such as number of channels, sampling interval, coordinates of the channels and the center of the array). The rest of the input parameters are specific for every array (these include number of time intervals, number of time samples in each interval, and the apparent velocity vector). In the third step, two more parameters are calculated – D(i) and β (Figure 4.1). D(i) is the distance from the center of the array to the i^{th} geophone, and β is the angle from the center of the array to the ith geophone and the reference direction in the horizontal (surface) plane of the array. The fourth step is a nested loop over different time intervals, apparent velocities, azimuths, time samples, and channels, for which the semblance coefficient is calculated. This flow chart represents the calculation of the semblance coefficient for one source position and a number of time intervals. Figure 4.2 shows how the time window is moved along the time axis. The example shown is for source#1, Array1. The gray rectangles indicate the width of the time window (in this case - 2ms). The time window is referenced to the center of the geophone array, and moved along the time axis until the desired time interval is covered. The procedure is repeated for every source position. The width of the time interval is different for different arrays. It depends on the dominant frequency of the wavelets for which semblance is being computed (this is further discussed in section 4.5).

Table 4.1: Flow chart of the semblance algorithm. This flow chart represents the calculation of the semblance coefficient for one source position. It has to be repeated for every source position.

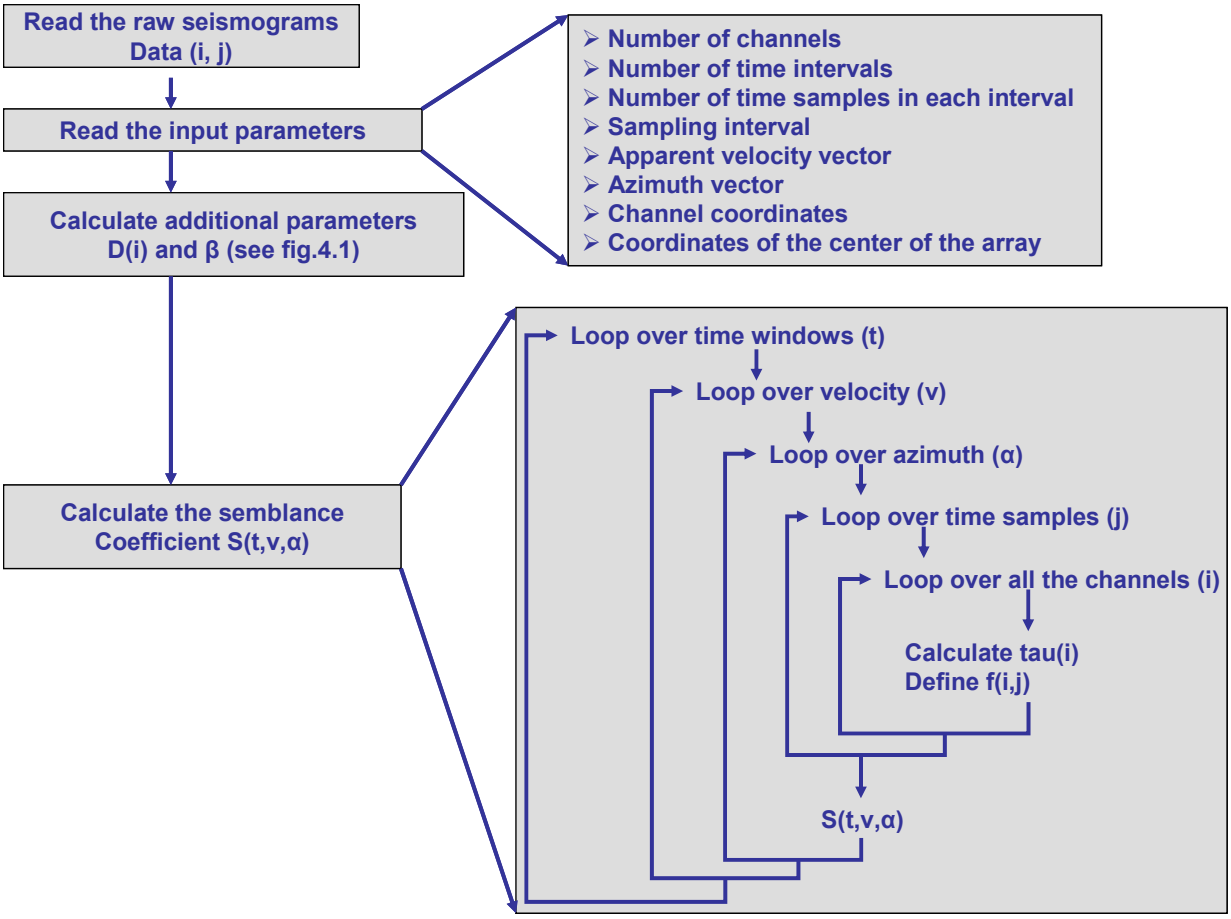

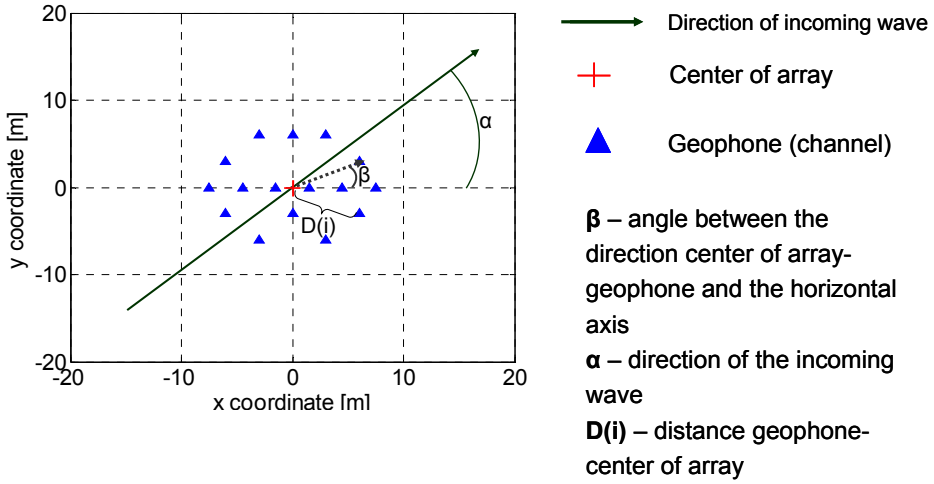

Figure 4.1: Explanation of some parameters used in the semblance algorithm (see Table 4.1). The blue triangles denote the different channels (i.e. geophones), the red cross is the center of the array, the angle between the direction geophone(i)-center of array and the horizontal axis is β, the azimuth (or direction towards which the wave propagates) is denoted as α, D(i) is the distance geophone (i) to the center of the array.

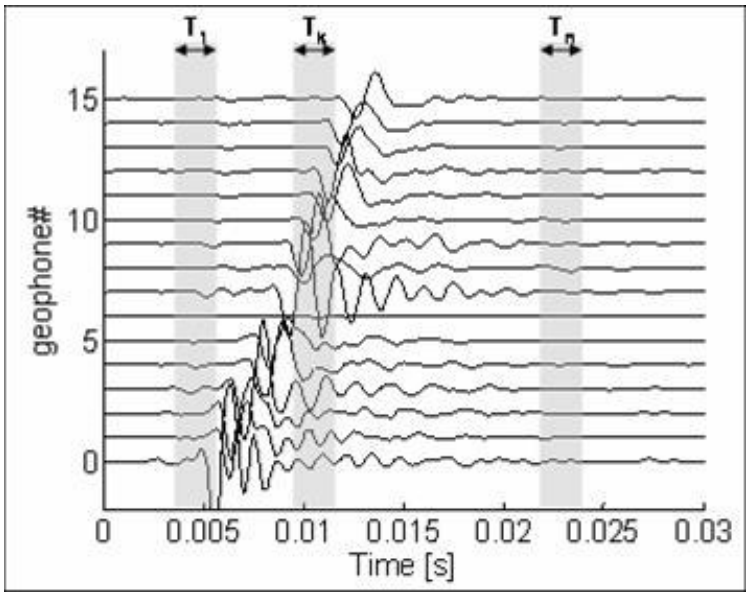

Figure 4.2: Choosing the time window. The example shown is for source#1, Array1. Here the gray rectangles indicate the width of the time window (2ms). It was calculated for each source position, for a number of time intervals ($T_1 \ldots T_k \ldots T_n$). The time window is referenced to the center of the geophone array.

4.3. Preliminary analysis of the seismic data

The preliminary analysis consisted of three steps.

STEP1: The raw binary data were corrected for DC offset using the Georgia Tech seismic acquisition program GT-SDAP.

STEP2: The corrected data were converted to Seismic Unix format (SU) using GT-SDAP.

STEP3: Visual examination of raw seismic records and their spectrum is performed, to identify any noise or acquisition problems. Then a decision is made, which traces are to be used. There were two weight-drops per source position for Array1 and Array3, so we could pick the better record. For Array2 though, we had only one weight-drop per source position. Examples of raw records for each of the arrays are shown on Figure 4.3 (Array1), Figure 4.4 (array2), Figure 4.5 (Array3). Even though these are recordings from two very different sites, there is one common feature that is immediately evident from the raw seismograms. The surface waves are not only dominating the records but they are the only clear arrivals that could be identified through visual inspection. The distant source positions on the soil site are an exception. The direct surface waves are not clearly observed because their amplitudes are quickly attenuated in the soil layer (Figure 4.5b). An increase in the gain of twenty-five times is necessary to be able to observe direct surface waves on some channels. Scattered waves are at the noise level and could not be distinguished on the raw seismograms for all field sites. The outcrop data (Figure 4.3 and Figure 4.4) show very little dispersion of the surface waves, while the soil data (Figure 4.5) are characterized by very strong dispersion, as was expected for a low-velocity surface layer over a high-velocity half space. More differences emerge as we plot the

spectrum of these raw seismograms. An example of the spectrum for two different source positions for each array is shown on Figure 4.6 (Array1), Figure 4.7 (Array2), and Figure 4.8 (Array3). For the outcrop data (Figure 4.6, and Figure 4.7) the recording signal spans a broad range of frequencies – from 100 to over 1000 Hz. The central frequency for the close source positions (up to 25m from the center of the array) is around 500 Hz and shifts towards lower frequencies as the source moves further from the array (due to attenuation of the high frequencies). For Array1, one channel, geophone #6, was not working, as it is seen from Figure 4.3. On the other hand, six more geophones (numbers 1, 4, 8, 9, 10, and 13) showed resonance frequencies (Figure 4.6), and were also excluded from the semblance analysis. Resonances are caused by undamped vibrations of the geophone housing that may correlate poorly between different geophones. Out of sixteen channels, only nine were used for calculating the semblance coefficient. For Array2, some spectral peaks in the seismic amplitude were observed for the source positions closer to the array, for frequencies around 1000Hz. These were initially interpreted as resonances. Later analysis proved that conclusion wrong (see section 4.5). In addition, two channels – #2 and #6, were not working. These were excluded from the analysis. For Array3, no resonance frequencies were observed. One channel (#14) was flat, and one more (#5) was not responding to the signal. These two channels were excluded from the analysis.

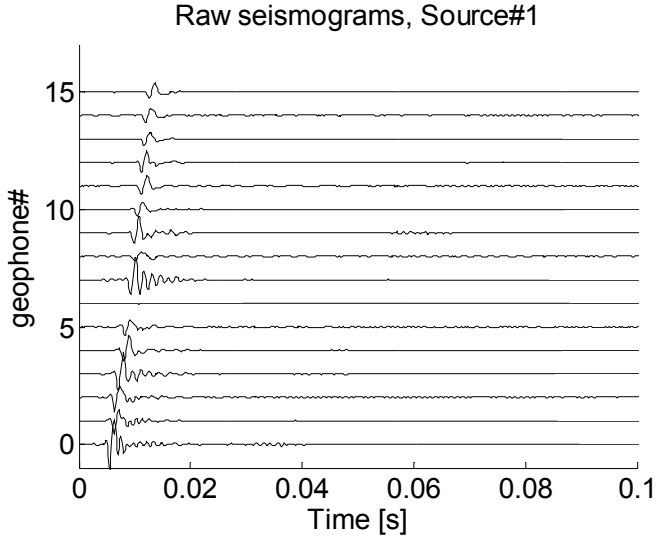

a)

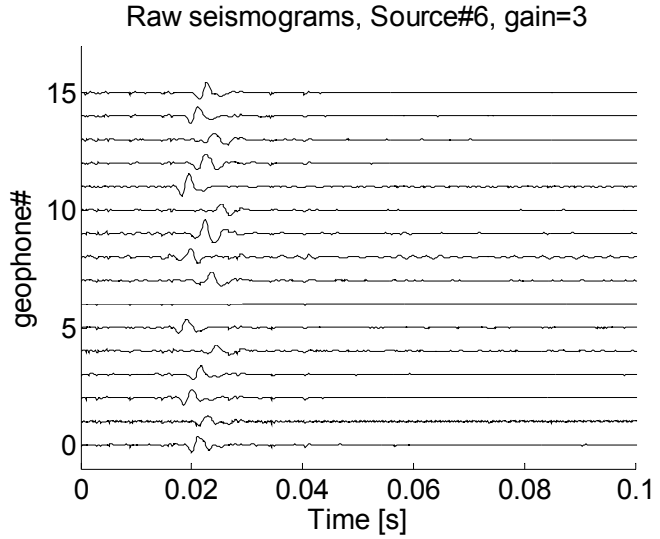

b)

Figure 4.3: Examples of two seismic records, at two different source positions, for Array1. (a) Source position#1 is 17.5m from the center of the array (refer to Figure 3.5a); (b) Source position#6 is 42m from the center of the array. This record shows some spiky noise, which was observed also at source positions # 4, 5, 7, 10, 13, and 14. Both records are showing very strong presence of surface waves and no visible scattered waves.

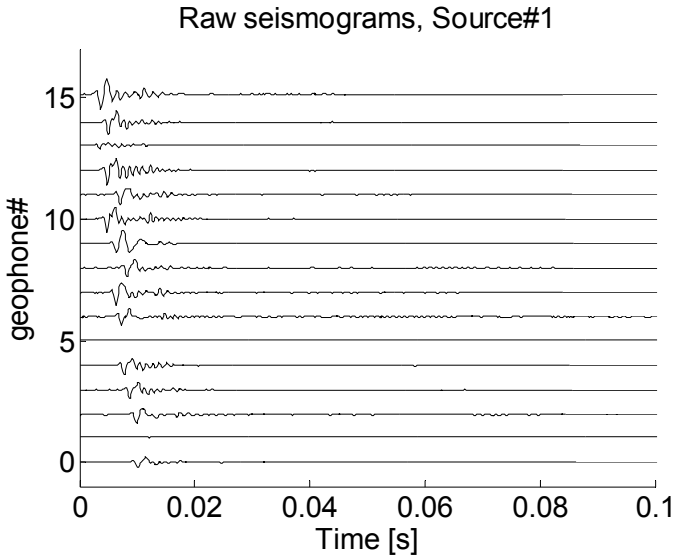

a)

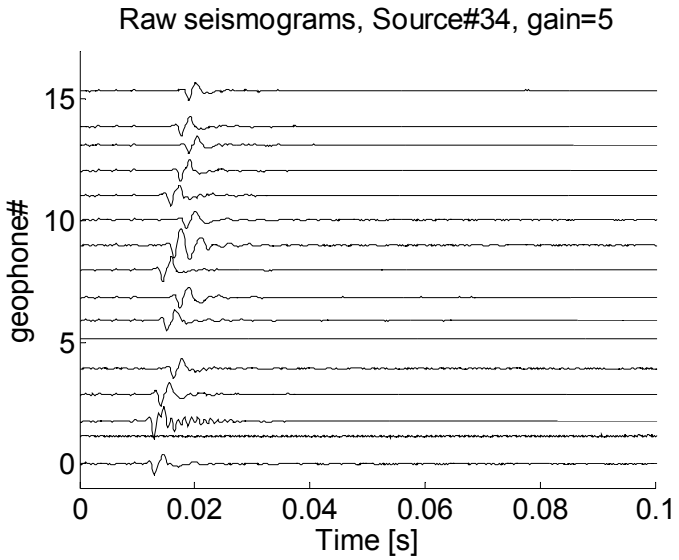

b)

Figure 4.4: Examples of two seismic records, at two different source positions, for Array2. (a) Source position#1 is ~20m from the center of the array (refer to Figure 3.5b); (b) Source position#34 is 40m from the center of the array. Both records are showing very strong presence of surface waves and no visible scattered waves.

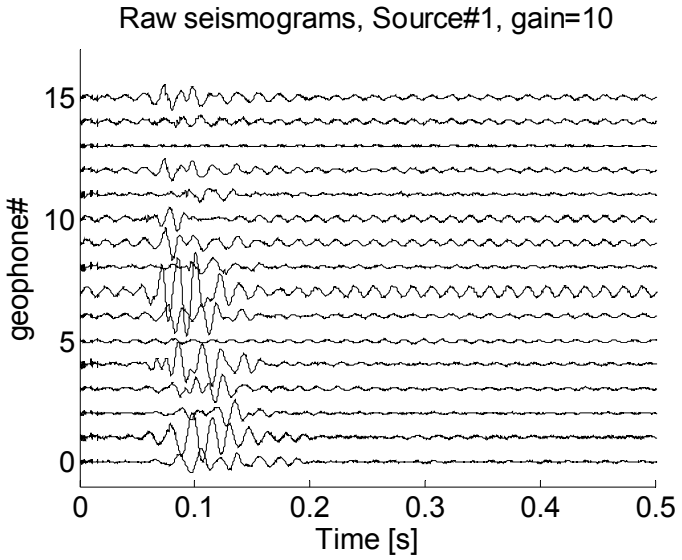

a)

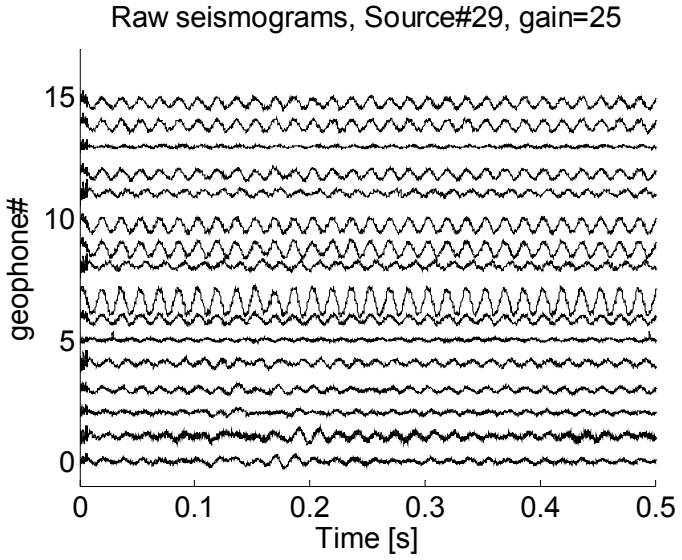

b)

Figure 4.5: Examples of two seismic records, at two different source positions, for Array3. (a) Source position#1 is 20m from the center of the array (refer to Figure 3.5c). The surface waves have very strong presence; (b) Source position#29 is 40m from the center of the array at. Surface waves can be identified on only a couple channels (the first two), and only after increasing the gain twenty-five times. Scattered waves are not seen on either of the two records.

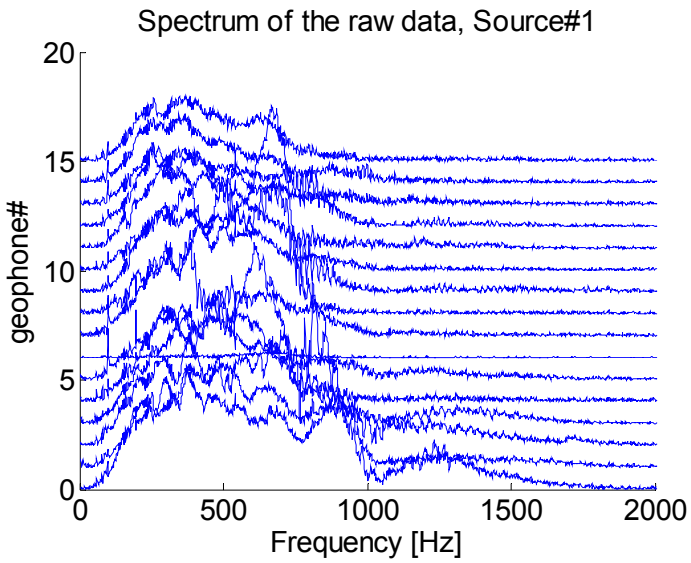

a)

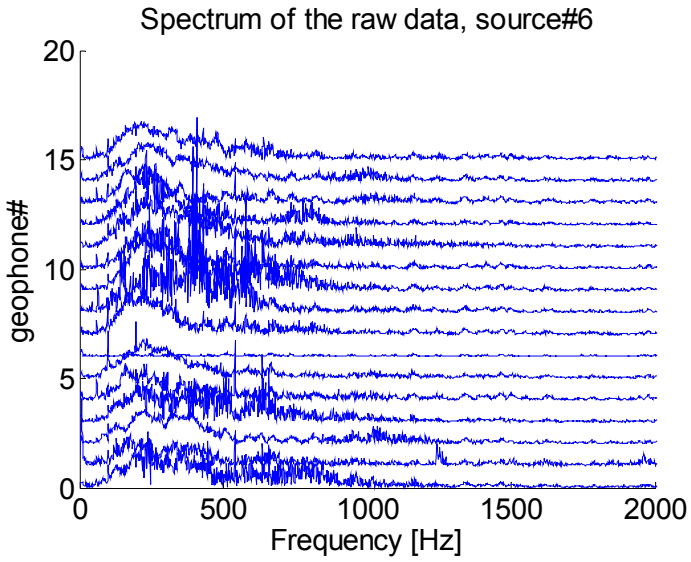

b)

Figure 4.6: Spectrum of the raw data from fig.4.3 (Array1). (a) for source positions closer to the center of the array (here source#1 is 17.5m from the array center), the observed spectrum spans from 100 to 1000 Hz. The central frequency is at 500 Hz; (b) as the source moves away from the center of the array, the higher frequencies are attenuated and the central frequency shifts to 250 Hz.

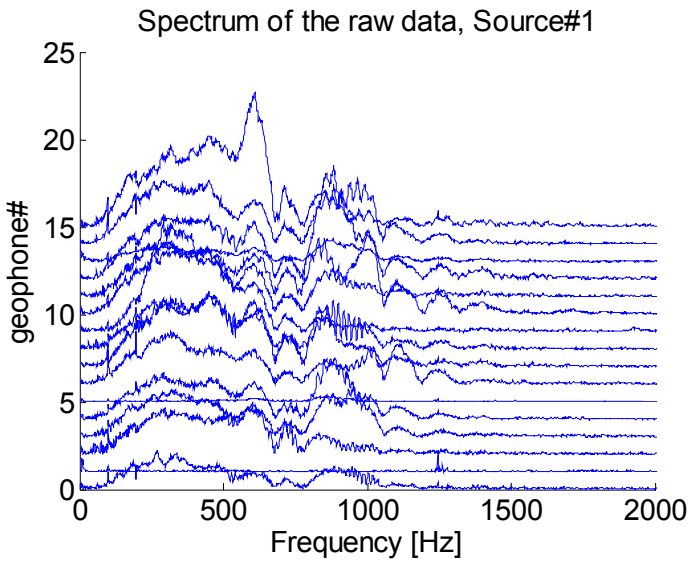

a)

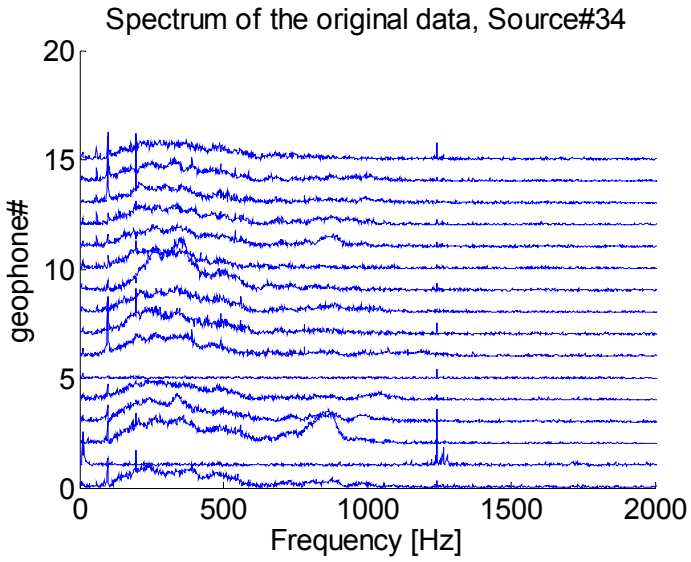

a)

Figure 4.7: Spectrum of the raw data from fig.4.4 (Array2). (a) for source positions closer to the center of the array, the observed spectrum spans from 100 to 1000 Hz. The central frequency is at 500 Hz; (b) as the source moves away from the center of the array, the higher frequencies are attenuated and the central frequency shifts to 250 Hz.

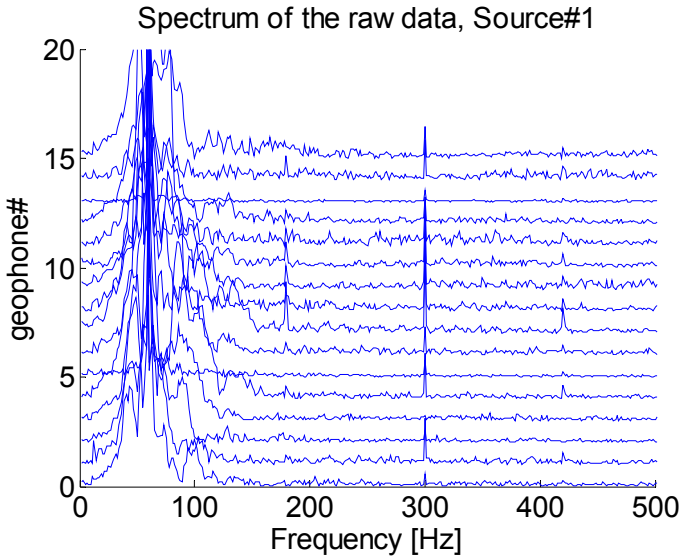

a)

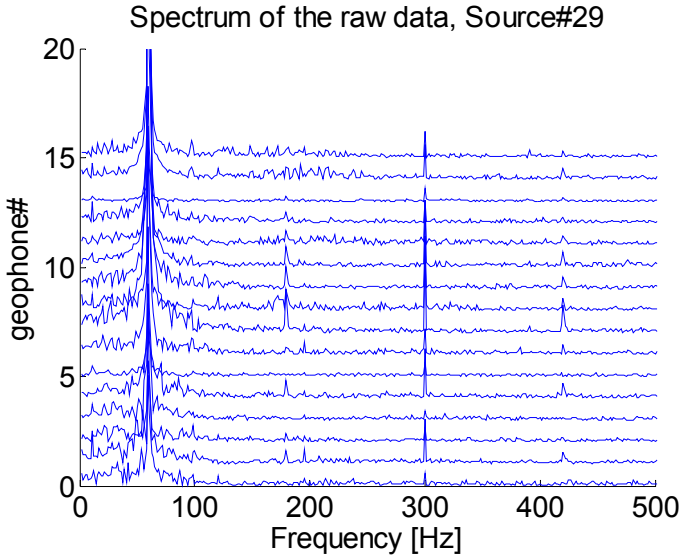

b)

Figure 4.8: Spectrum of the raw data from fig.4.5 (Array3). (a) source#1 is at 22m from the center of the array, the observed spectrum spans from 10 to 120 Hz. The central frequency is at 60 Hz; (b) source#29 is at 40m from the center of the array, frequencies above 60Hz are significantly attenuated. The 60Hz signal is probably due to electrical interference.

4.4. Testing the semblance algorithm

The testing of the semblance algorithm was done in two steps. In the first step, synthetic seismograms were generated, assuming plane wave propagation and the geometry of our geophone array. Figure 4.9 shows a set of synthetic traces (Figure 4.9a) and the calculated semblance coefficient (Figure 4.9b). Three plane waves (400Hz Ricker wavelet) were generated. Two waves are traveling towards the array (i.e. azimuth=0° (or 360°.), with apparent velocities of 2000m/s and 4000m/s and a third wave, traveling away from the array (i.e. azimuth of 180°), with 2000m/s apparent velocity. It must be noted here, that the "azimuth" is the direction of wave propagation, it is not back-azimuth, i.e. it does not indicate the azimuth to the source. Assuming that the waves propagate in a straight line, the back-azimuth (i.e. the azimuth of the source) will be 180° off the direction of propagation (here referred to as "azimuth"). For example, the two waves that are propagating in direction 0° (or 360°) with respect to the center of the array, where two of the maximums of the semblance coefficient are observed, are coming from a back-azimuth of 180°. Respectively, the wave that travels in direction of 180° with respect to the array, is coming from a back-azimuth of 0° (or 360°). However, ray curvature could cause the back azimuth to point in a direction different from the direction to the source. With other words, we assume no ray curvature here. Random noise was added to the seismograms at a level of 25% of the peak amplitude. We can clearly distinguish the three maximums of the semblance coefficient, associated with each of the waves (Figure 4.9b). The semblance technique resolves the azimuth to within +/- 5°. This confirms that the velocity did not vary sufficiently along the propagation path to cause

curvature in the raypath. The uncertainty in apparent velocity varies between +/- 50m/s (for waves traveling at 2000m/s) and +/- 400m/s (for waves traveling at 4000m/s).

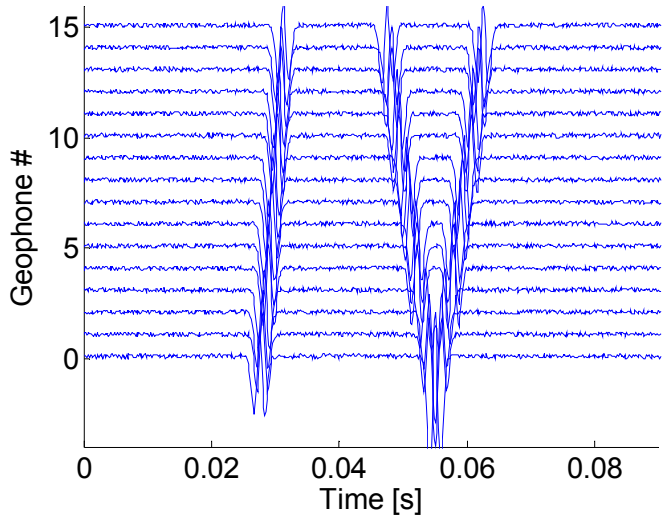

a)

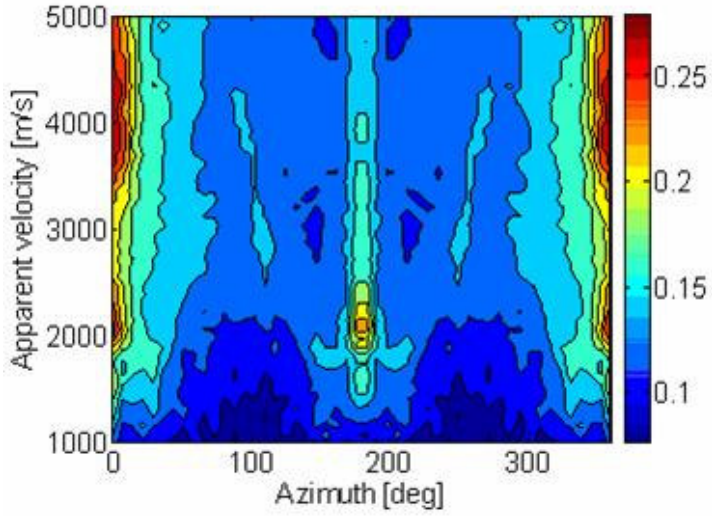

b)

Figure 4.9: a) Raw synthetic seismograms with three plane waves (400Hz Ricker wavelet). Two waves are propagating towards the array (i.e. at azimuth 0°), and a third wave is propagating away from the array (i.e. at azimuth of 180°). Two waves are traveling with 2000m/s apparent velocity, and a third one – with 4000 m/s; b) contour plot of the semblance coefficient, calculated as a function of apparent velocity and azimuth, for the time interval 0.025-0.06 sec. (this interval includes all the three waves).

In the second step, the algorithm was tested with real data, with the direct surface waves. Because surface waves were so prominent on the seismograms, it was easy to define their velocity from the travel-time curve. For Array1 and Array2 the direct surface wave velocity was calculated to be 2100m/s. The semblance coefficient was calculated for a range of apparent velocities (2000-8000m/s) and azimuths (0° to 360°). The step in apparent velocity was chosen to be 100m/s, and the step in azimuth – 6°. The time interval was selected to consist only of the direct surface waves and had duration of 5ms.

Figure 4.10 shows the results for Array1. The maximum of the semblance coefficient is observed at 2100 m/s, which is the surface wave velocity that we calculated from the travel time curve. It also corresponds to a direction of propagation that is in excellent correlation (with a standard deviation of less than 1°) with the back-azimuth of the source positions. We observe how the azimuth of maximum semblance changes as the source is moved around the array, but the apparent velocity does not. For Source#1 (Figure 4.10a), the maximum of semblance is at 0° (or 360°), therefore the back-azimuth of the source will be at 180°. Respectively, for Source#7, the maximum in the semblance coefficient is at 262°. (Figure 4.10b), therefore the back-azimuth of the source is at 82°; for Source#13, the azimuth is at 216° (Figure 4.10c), therefore the back-azimuth is at 36°. The correlation between the real back-azimuth of the source position and the back-azimuth calculated based on the maximum of the semblance coefficient, is observed for all source positions (Figure 4.11). For twelve out of fifteen source positions, the accuracy in azimuth is within 1°, for two source positions (source#2, and source#15) it is 3°, and for source#14 we have the lowest accuracy of 6°. The uncertainty in defining the apparent velocity of the direct surface waves is on average +/- 70m/s.

The two tests show that the assumption for plane wave propagation is reasonable and the semblance technique proves to be able to identify the apparent velocity and azimuth of the coherent arrivals with acceptable uncertainty. Similar results were observed for the data collected from Array2. Since Array3 was conducted on soil, the observed dispersion in the surface waves significantly complicated the definition of the direct arrivals, using the semblance algorithm. This problem is further discussed in section 4.6.

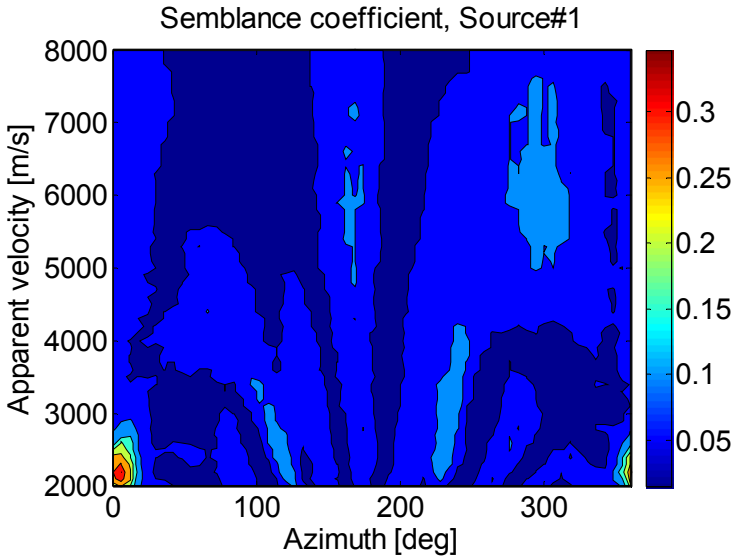

a)

Figure 4.10: Examples of contour plots of the semblance coefficient for direct surface waves, as a function of the apparent velocity and azimuth (i.e. direction of propagation) for Array1. (a) source#1; (b) source#7; and (c) source#13. The horizontal axis indicates azimuth in degrees. This is 180° off the back-azimuth of the source (assuming plane wave propagation). For example, for Source#1 (a), the maximum of the semblance coefficient is at azimuth of 0°, therefore the back-azimuth of the source is at 180°. The vertical axis shows the apparent velocity, and the color bar indicates the value of the semblance coefficient (red-highest, and blue-lowest). The plots demonstrate the ability to resolve the apparent velocity and azimuth of the direct surface waves.

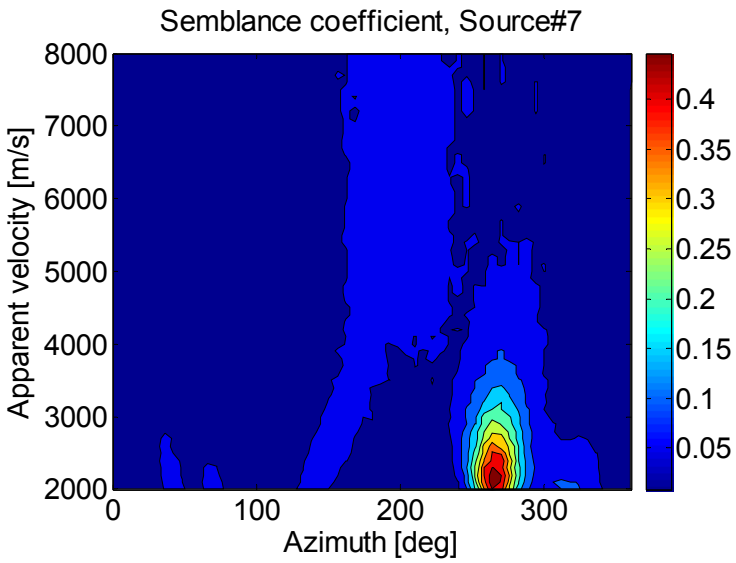

b)

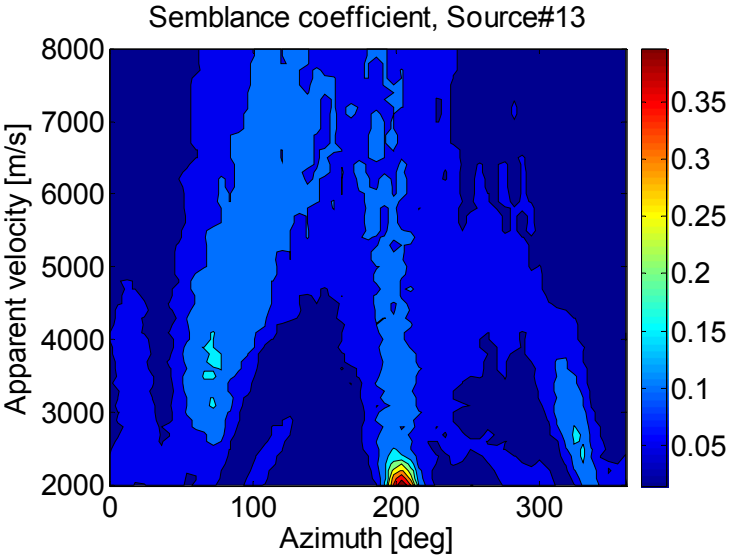

c)

Figure 4.10: Continued

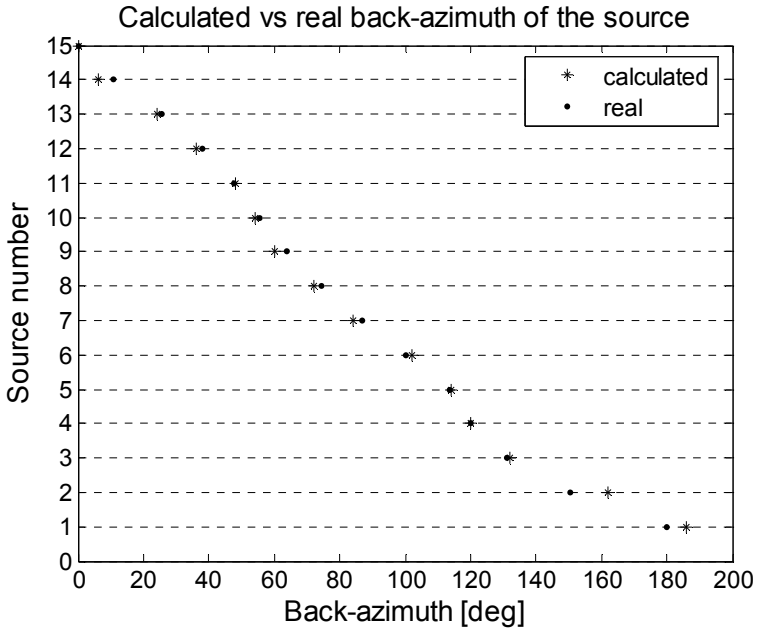

Figure 4.11: Comparison of the calculated and the real back-azimuth of the source, for Array1. The horizontal axis shows the source number (refer to Figure 3.1a for the location of the source with respect to the array), the vertical axis is the back-azimuth in degrees. The calculated back-azimuth is based on the maximum of the semblance coefficient from the semblance plots (stars), for direct surface waves, generated for each source position. The value for the "calculated" azimuth was taken as the maximum value from the azimuthal distribution, for velocity of 2100 m/s. The real back-azimuth of the source (dots) is estimated based on the coordinates of the source and the coordinates of the center of the array.

4.5. Effect of different factors on the semblance coefficient

Even though semblance has been used extensively in exploration geophysics, as a measure of the coherence of multichannel data, starting in the 1960s, it was not until the end of the 1970s when the statistical significance of semblance was examined. Douze and Laster (1979) offered the first evaluation of semblance as a statistical measure of the coherence of multiple channels. Their work is showing the effect of different factors such as number of channels, bandwidth, time window width, or S/N ratio on the performance of the semblance coefficient as a measure of the coherence of the signal. The number of

channels (tests were performed with 6 and 24 receivers) was found to not have significant effect on the semblance, if no signal is present (i.e. S/N=0). The other three factors though affect semblance significantly. For example, if either the bandwidth or the width of the time window decreases, the probability that S will exceed 0.05 nearly doubles (in the absence of coherent signal). For random noise, the semblance will have a two times higher value than if the time window or the bandwidth is narrowed. On the other hand, if coherent signal is present an increase in S/N ratio of 4 times, leads to an increase of 20% in the probability of semblance to exceed 0.1. Another important result of this study is the fact that the probability of semblance to exceed 0.1, for the lowest S/N ratio is 80%. This sets a low threshold level for the imaging algorithm, described in Chapter 5. Based on the study of Douze and Laster (1979), we can consider a value of semblance of 0.1 or higher to be an indication of the presence of a coherent signal. The same threshold was used by Bannister and Melhuish (1997).

Here, we study the effect of noisy channels, time window width, and frequency filtering on the data collected on the granite outcrop. The data obtained on unweathered rock (Array1 and Array2) have much higher frequency content, and the results of these tests will be a contribution to the work described above. In addition, these results will provide the processing steps for obtaining high semblance scattered waves, which is essential for the 3-D imaging algorithm.

The processing of the data from the soil site (Array3) will be covered in section 4.6. The dispersion of surface waves is significant factor to be considered in the calculation of scattered waves at sites with a significant overburden of lower velocity soils.

4.5.1. Effect of "noisy" channels.

The "noisy" channels are considered channels that show resonance noise. We observed six such channels for Array1. In addition, here we add to this category channels that are flat (such as channels #2, and #6, for Array2), or channels that are showing only a single frequency peak (such as channel#6 – 60Hz, for Array3). This 60Hz peak in the spectra is due to electrical interference.

The test was performed for 5ms width of the time window. The values and uncertainty in the semblance coefficient were compared for: (1) using all available channels; and (2) using only the channels that were selected as "good" after the preliminary analysis of the seismic data. The test was performed for different time windows, in order to study the effect of "noisy" channels on direct surface waves, direct body waves (P or S), and scattered waves. The results were very consistent among the different arrays. The consistency extends to different phases as well.

Array1

We generated semblance plots for time intervals for the first 0.05s of the seismic record (with time window of 5ms, and an overlap of 2ms between time windows. This time interval includes the direct, and scattered body waves and the surface waves. For the time intervals, covering the arrival of direct surface waves, we observed that for half of the source positions, the use of all channels led to lower value of the semblance coefficient, and for some of them also to bigger uncertainty in defining the azimuth and the apparent velocity. For the other half of the source positions, there was no significant change in the value of the semblance coefficient, but we did observe an increase in the uncertainty, when the "noisy" channels were used (Figure 4.12). In summary, if the

"noisy" channels are excluded from the analysis, the resolution in defining the apparent velocity and azimuth will either improve, or not change at all.

The semblance technique failed to identify the apparent velocity and azimuth of direct body waves, for most source positions. There were only four exceptions – for source positions 8, 12, 13, and 14 (refer to Figure 3.5a, Chapter3 for the exact locations of these source positions with respect to the geophone array). When we compare the calculations made with all channels and without "noisy" channels, we observed the same trend as the one for the direct surface waves. The semblance coefficient had lower value and higher uncertainty if all channels were used. For source#8 in fact, the P wave was clearly observed only if the "noisy" channels were excluded (see Figure 4.13).

The semblance plots generated for direct surface waves revealed the existence of "near-source" reverberations. The end of the reverberations was chosen to be the first time intervals for scattered waves. The effect of "noisy" channels was found to be the same as the one observed for direct surface and body waves. Overall, the semblance coefficients for scattered waves were observed to be much lower than the ones for the direct waves. For most source positions, the value was below 0.2, and the uncertainty was very large, to the extent that individual phases were not resolvable. Fig.4.14 shows an example of the effect of the removal of the "noisy" channels on scattered shear waves, for source position#13. This source position had the highest value of semblance for scattered waves. The figure shows that if all channels are used, the value of semblance is lower, but so is the uncertainty in defining apparent velocity and azimuth for the scattered shear waves.

Array2

The test performed for Array1 was repeated for Array2. For the sources located close to the center of the array (up to 25m), frequencies above 1000Hz were observed and initially interpreted as resonances. Figure 4.15 shows the spectrum of source#4, which had nine channels with resonance-like noise (Figure 4.15a, in red). They are considered the "noisy" channels in the tests here. The calculated semblance coefficient, for the case when the "noisy" channels were excluded is presented on Figure 4.15b. No pick is observed at the expected velocity and azimuth of the direct surface waves. If all channels were used (Figure 4.15c), the pick appears at the right position. Similar effect was observed for the other source positions that were close to the center of the array, regardless of their azimuthal distribution. Because most of the source positions were at close distances to the center of the array, we make the conclusion that the 1000 Hz picks are not due to resonances, but rather due to high frequency signal, not yet attenuated. Additional tests are showing that if only channels #2 and #6 (flat) are excluded from the analysis, this leads to higher values of the semblance coefficient for the direct surface waves.

The direct body waves were observed for very few source positions, just like for Array1. These very few source positions were in fact farther away from the center of the array. This is possibly due to the fact that the time separation between body waves and surface waves increases with distance – hence interference from surface waves up close limits the ability to resolve body waves. The semblance coefficient has higher values and lower uncertainty if channels #2 and #6 are excluded. The semblance coefficient for

scattered waves is observed to be very low in general, below 0.15. It is slightly higher if channels #2 and #6 are excluded.

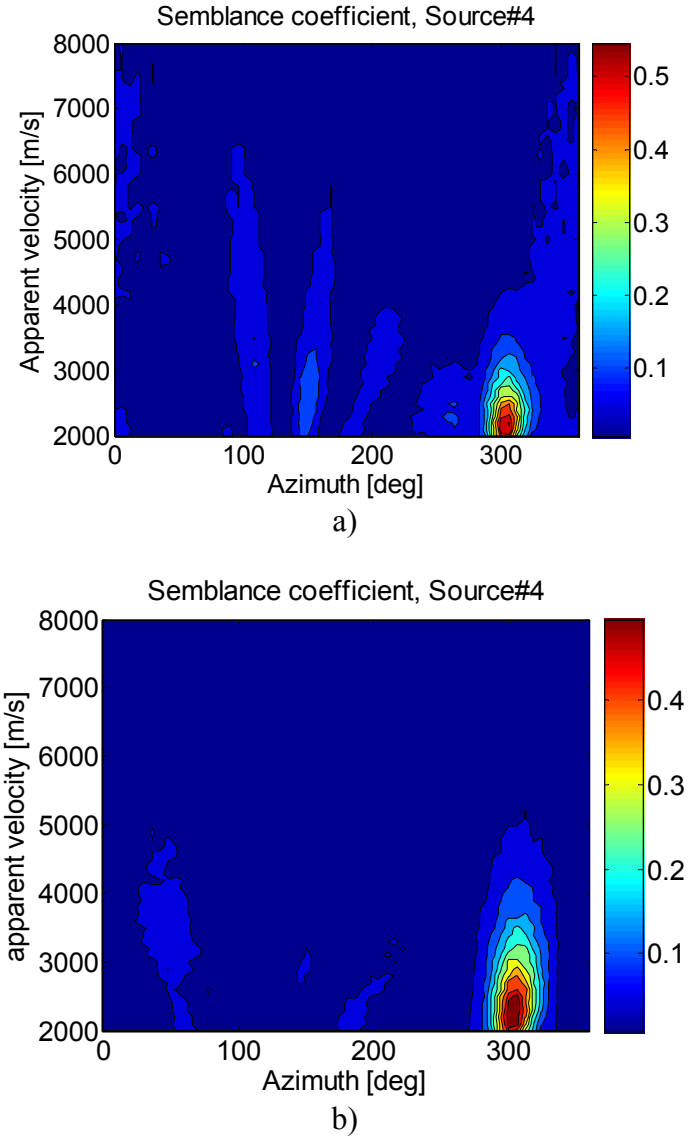

Figure 4.12: Semblance coefficient of direct surface waves, source#4, Array1, calculated for width of the time window of 5ms, using (a) only the nine "good" channels and (b) all channels (i.e. including the once that resonate). If all channels are used, the semblance coefficient has much lower value and much bigger uncertainty.

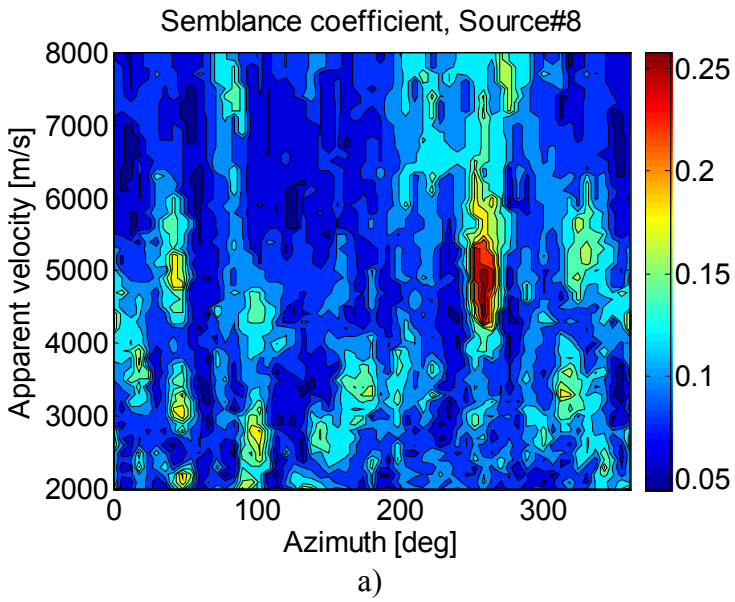

a)

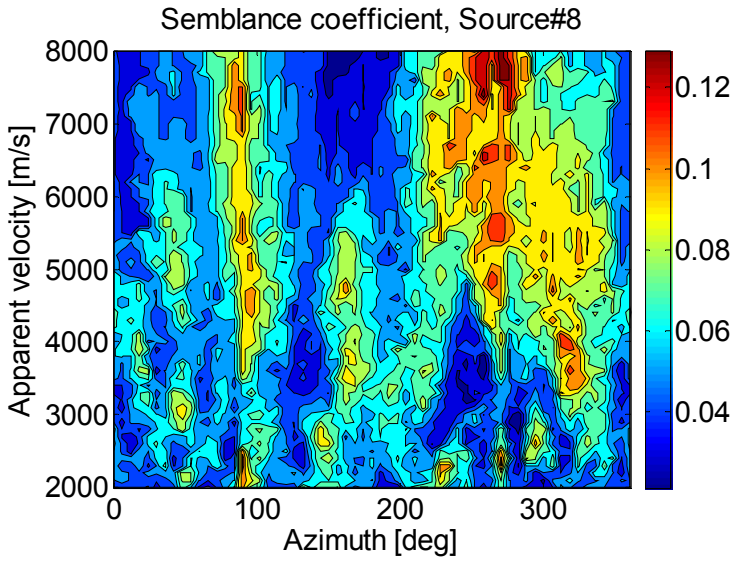

b)

Figure 4.13: Semblance coefficient of direct body waves, source#8, Array1, calculated for time window of 5ms, using (a) only "good" channels; (b) all channels. If the channels with significant resonance noise are used, the direct P-arrival is completely obscured (b).

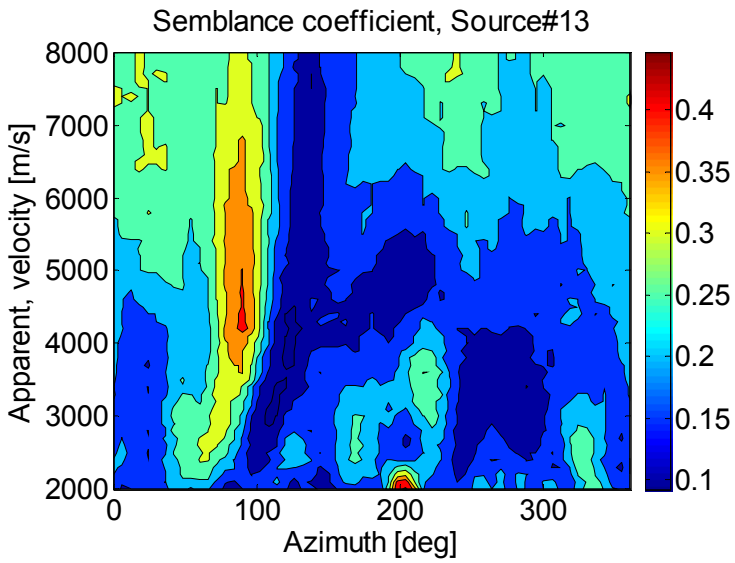

a)

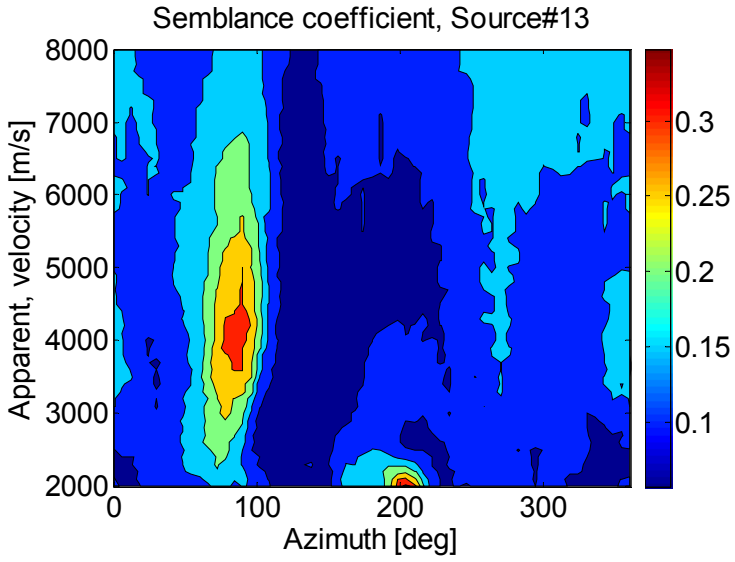

b)

Figure 4.14: Semblance coefficient of scattered waves (t=0.0355s), source#13, Array1, calculated using (a) only the nine "good" channels, and (b) all channels. The "all channels" case (b) shows bigger uncertainty in defining the azimuth and apparent velocity of the scattered waves, and lower value for the semblance coefficient.

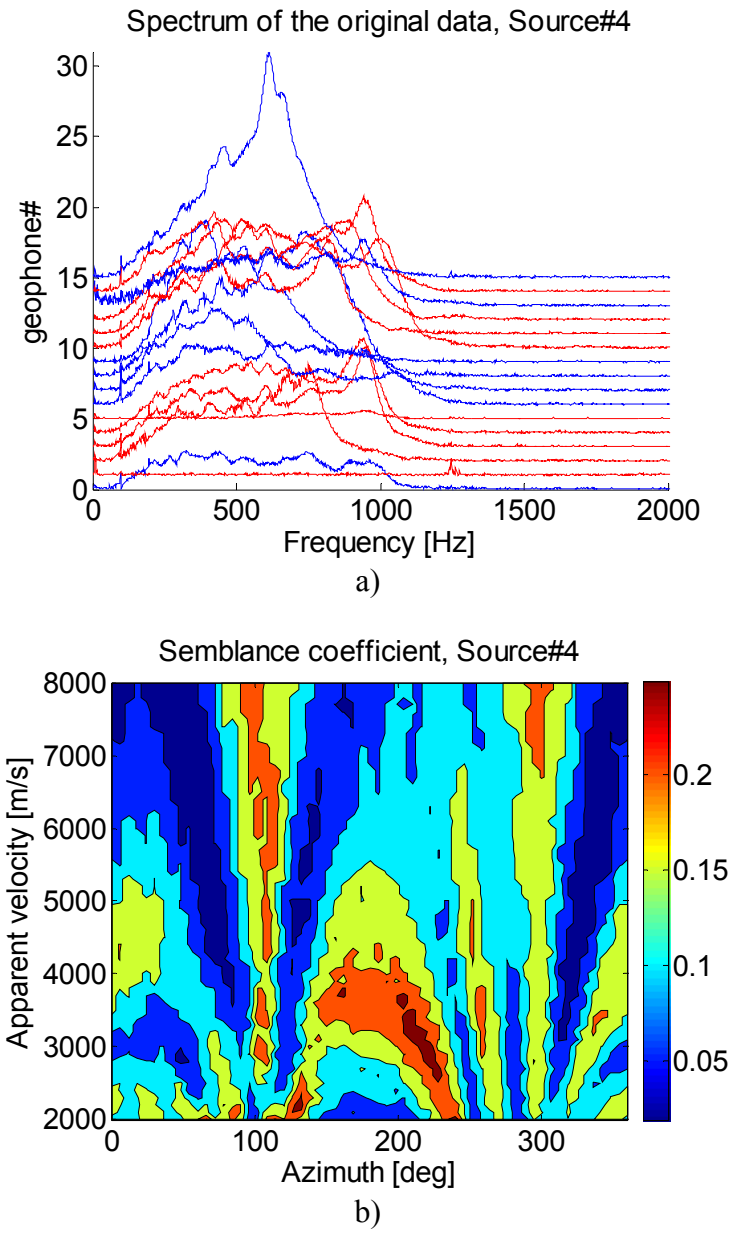

Figure 4.15: (a) spectrum of the data recorded at source position#4, Array2. (b) semblance coefficient for direct surface waves, for time window of 5ms, calculated if the channels in red were excluded. (c) the semblance coefficient calculated if all channels were used.

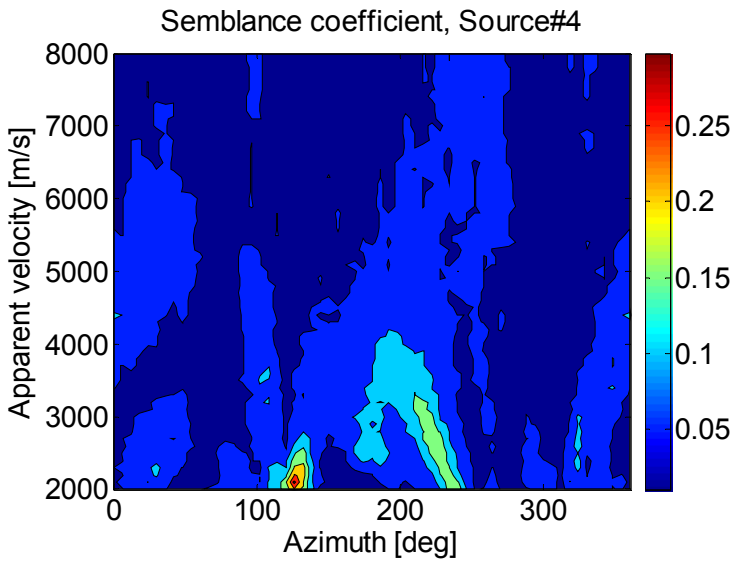

c)

Figure 4.15: Continued

4.5.2. Effect of the width of the time window

This test was performed for width of the time window of 2ms, using only the channels classified as "good", based on the preliminary analysis and the results from the test described in section 4.5.1.

Array1

For the time of arrival of direct surface waves, for all source positions, the maximum value of the semblance was higher if calculated with 2ms time window than the one calculated with 5ms time window. This becomes clear when we compare Figure 4.16 (2ms time window) and Figure 4.12 (5ms time window). The maximum value of semblance for 5ms window is 0.53, and for 2ms window – it is 0.6, i.e. there is an increase of 13% due to the narrower time window.

Similar comparison can be done for direct body waves, Figure 4.17 (2ms time window) and Figure 4.13 (5ms time window). The maximum value of the semblance is

nearly three times higher when the narrower time window is used. In addition to that, we observe slightly higher resolution in the azimuth, but the same uncertainty in the apparent velocity. For some source positions we observed even stronger effect of the narrow time window. For example, the semblance plot for the arrival time of direct body waves for source#1 does not show any P or S arrivals if 5ms time window is used (Figure 4.18b). These arrivals appear as a very clear maximum of the semblance coefficient if 2ms time window is used (Figure 4.18a). The maximum is observed at apparent velocity of 5100m/s and azimuth of 0 degrees, and is very prominent (0.7). This value of semblance is comparable to the values obtained for most of the direct surface waves. It must be noted here, that the direct P and S waves had amplitude very close to the noise amplitude, and yet they are characterized with a semblance coefficient comparable to that of direct surface waves. This is due to a wavelet length factor. If the seismic waves are in a wavelet of 2 ms for example, then a window wider than 2 ms will exhibit a decreasing semblance as the window increases – because other wavelets can interfere. Hence there is an interference factor also recognized as a resolution factor for two wavelets coming in from different directions.

The test on scattered waves shows the same trend as for direct surface and body waves. For example, for source position#13, the maximum of the semblance of scattered P waves (Figure 4.19) is 33% higher than the maximum value obtained by using 5ms time window (Figure 4.14a). This effect was observed for all source positions.

Array2

For Array2, the semblance coefficient for direct surface waves was observed to be higher if 2ms window is used. Figure 4.20 shows the calculated semblance coefficient for source#34. Its maximum value is 17% higher than it was when the calculation was performed for 5ms width of the time window (see Figure 4.15c). This trend was observed for all source positions. The difference in the maximum value of semblance varied in the range of 8-70%, for most source positions it was around 20%.

The same effect was observed for direct P and S waves. Figure 4.21 shows an example of the effect of 2ms time window, calculated for the time of arrival of direct body waves, for source#23. The narrowing of the time window leads to an increase of more than three times in the maximum of the semblance coefficient. It also results in a decrease in the uncertainty in azimuth and apparent velocity.

The narrowing of the time window leads to higher semblance coefficient for scattered waves as well. Figure 4.22 shows an example of such a difference, for source#23. The observed shear and surface waves have 54% higher maximum value of the semblance coefficient if calculated with 2 ms window than with 5 ms window.

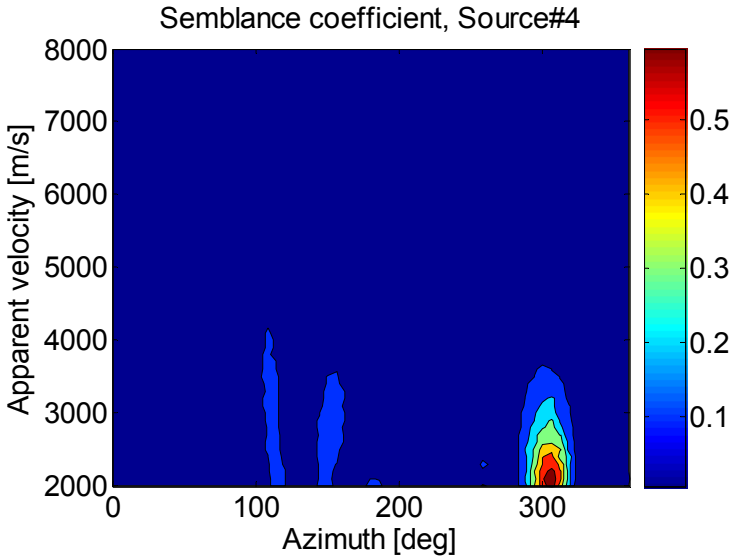

Figure 4.16: Semblance coefficient for direct surface waves, source#4, Array1, calculated for 2ms width of the time window, source#4, Array1. The maximum value of the semblance is higher than the maximum value calculated when the width of the time window is 5ms (see fig. 4.12).

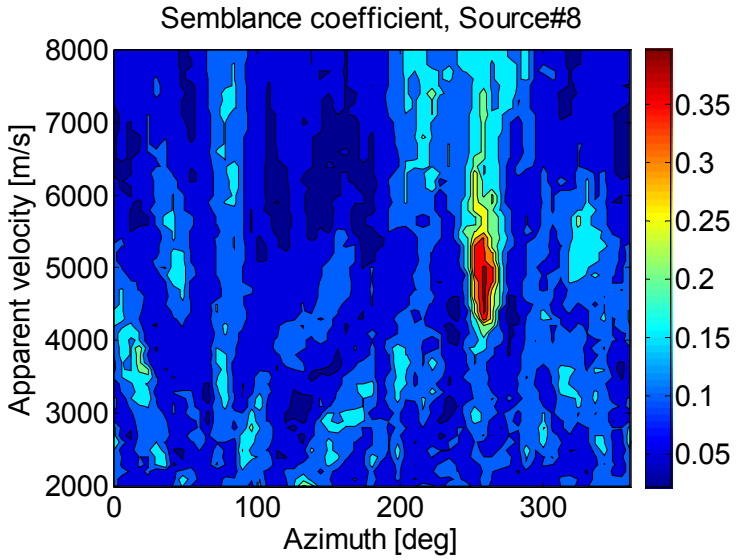

Figure 4.17: Semblance coefficient of direct body waves, source#8, Array1, calculated with 2ms time window. The direct P waves are observed to have a sharp peak in the semblance coefficient at apparent velocity of 5100 m/s.

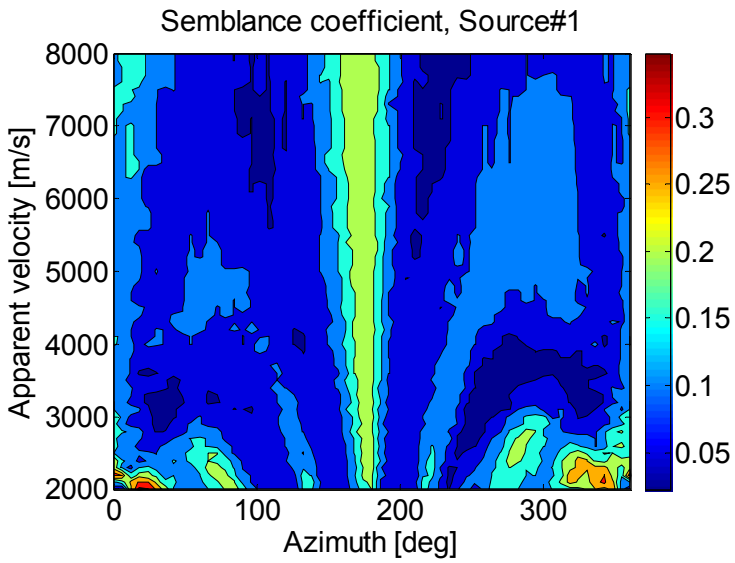

a)

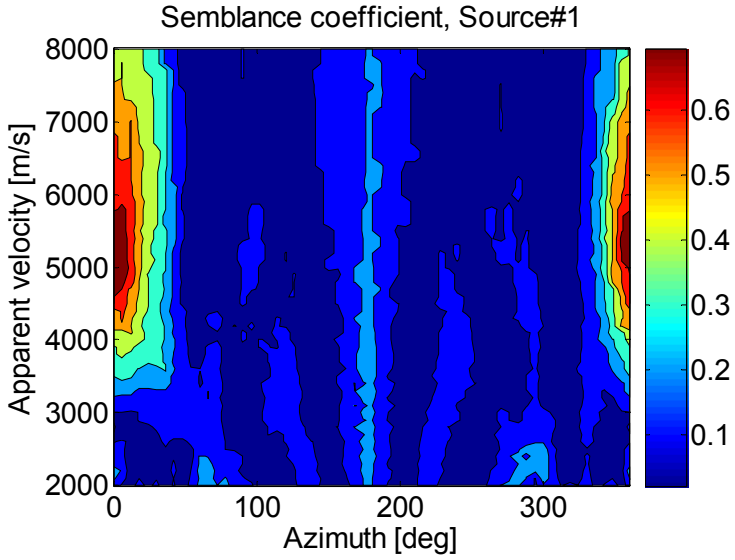

b)

Figure 4.18: Semblance coefficient for direct body waves, for source#1, Array1, calculated with (a) 5ms time window; and (b) 2ms time window. The narrower time window results in a very distinct peak in the semblance coefficient that corresponds to the azimuth and apparent velocity of the direct body waves. That is when the window is widened to include some surface waves, the body waves are not resolved such as the case with (b).

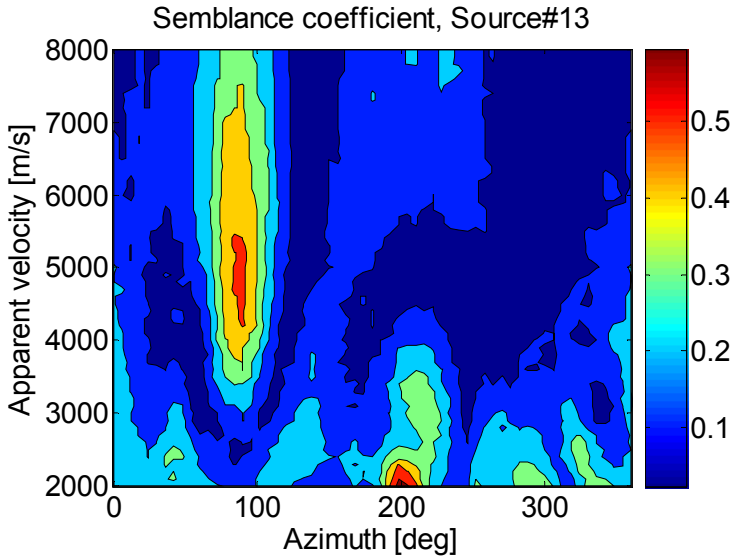

Figure 4.19: Semblance coefficient of scattered waves, source#13, Array1, calculated with 2ms time window. The maximum value of semblance is at 0.6, which is 33% higher than the maximum value obtained with 5ms time window.

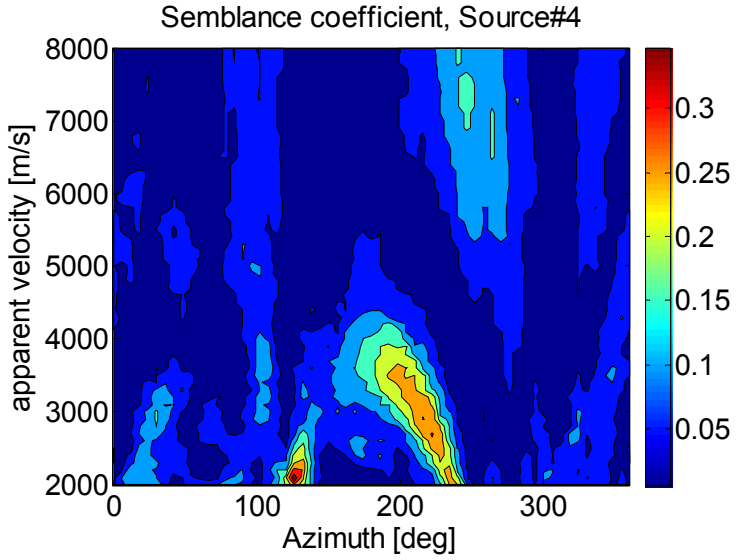

Figure 4.20: Semblance coefficient for direct surface waves, source#4, Array2, calculated with time window width of 2ms. The semblance coefficient is 17% higher than the one calculated for 5ms time window (see Figure 4.15c).

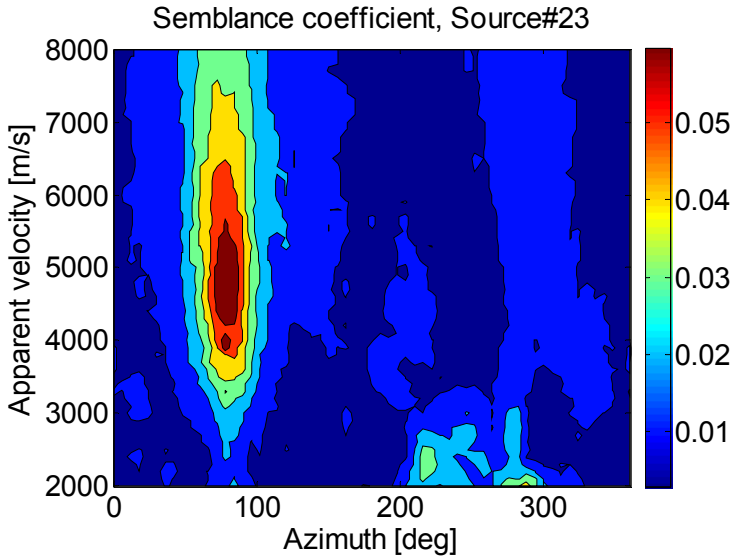

a)

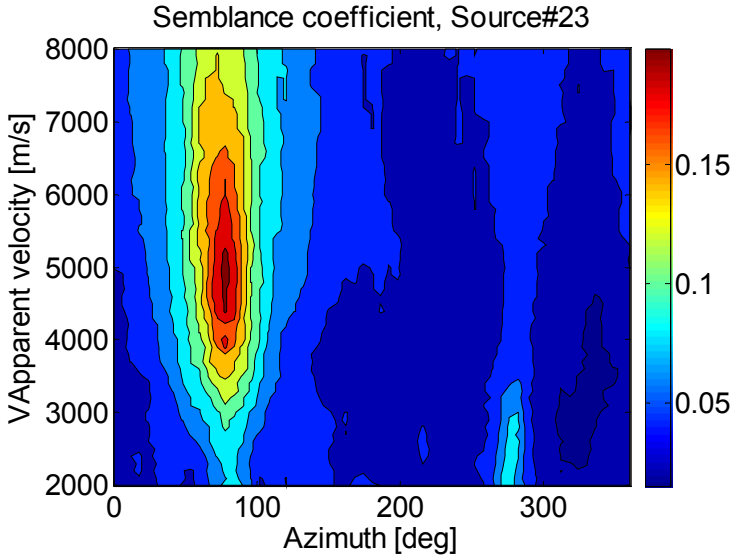

b)

Figure 4.21: Semblance coefficient for direct P waves, source#23, Array2, calculated with (a) 5 ms time window; and (b) 2 ms time window. The narrowing of the time window leads to an increase of more than three times in the maximum value of the semblance coefficient, as well as significant decrease in the uncertainty of that maximum value.

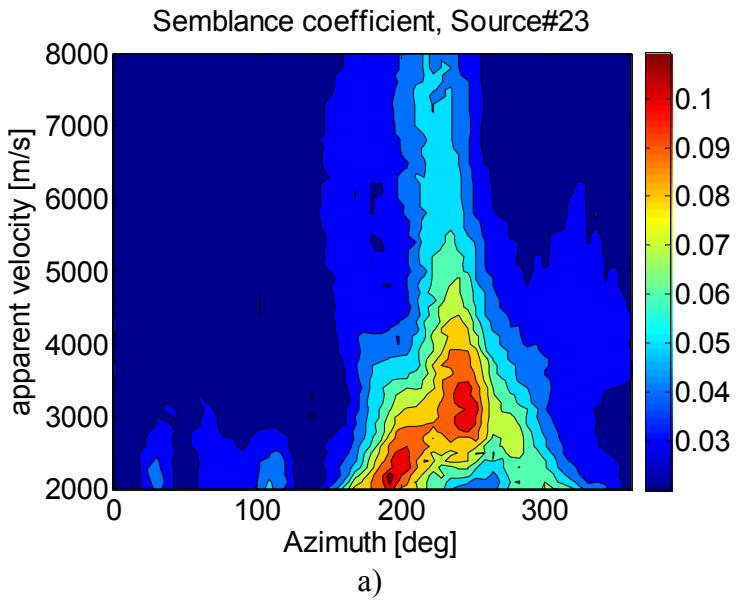

a)

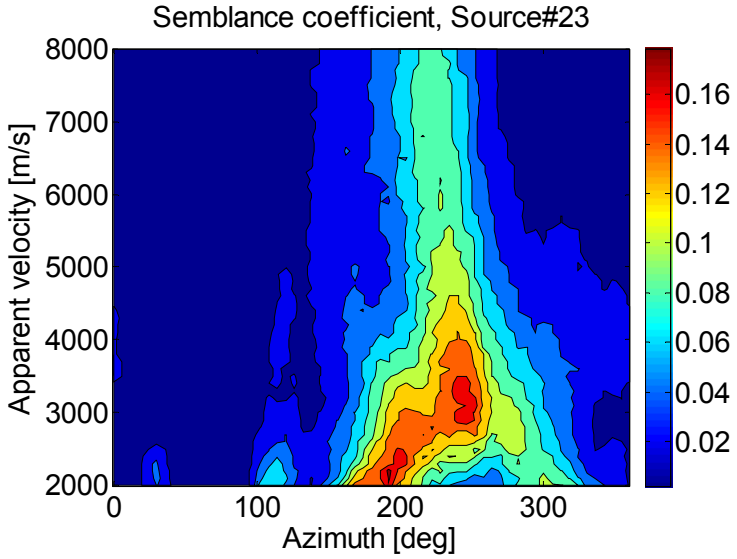

b)

Figure 4.22: Semblance coefficient for scattered waves, source#23, Array2, calculated for (a) 5ms time window; (b) 2ms time window. Scattered shear and surface waves are observed to have 54% higher maximum value of the semblance coefficient if calculated with 2ms window than with 5ms window.

4.5.3. Effect of the frequency filtering.

To study the effect of frequency filtering we applied Gaussian filter with different central frequencies to the data before semblance coefficient was calculated. For direct surface waves, the filter was centered at 200 Hz, with standard deviation of 30 Hz. For direct and scattered P and S waves, the central frequency was at 500 Hz, and standard deviation of 100 Hz. We later found out that 400 Hz central frequency leads to better results.

Array1

Figure 4.23 shows an example of the effect of 200 Hz Gaussian filter on direct surface waves for source#1. If semblance is calculated after the data are filtered, it has a maximum value of 25% higher than the value calculated if data are not filtered. Hence filtering is a way to focus on the frequency content of the wavelet and to eliminate other frequencies that may be dominated by noise.

To study the effect of filtering on direct body waves, data were filtered at 500 Hz central frequency, with standard deviation of 100 Hz. For source#1 (see Figure 4.18 for semblance obtained without filtering) we observed lower maximum value of the semblance coefficient. The test was repeated with central frequency of 400 Hz, and the same standard deviation (Figure 4.24). The maximum value of S appeared the same as in the case of "no filtering", but the uncertainty in apparent velocity and azimuth was significantly reduced. This effect was observed at all source position.

The same 400 Hz central frequency Gaussian filter was applied to the scattered arrivals. Figure 4.25 shows the effect that filtering had on scattered waves recorded at source#13. When compare this plot with the semblance calculated without filtering

(Figure 4.19), we notice that the value of the semblance coefficient is only slightly increased due to the filtering, but the uncertainty in the apparent velocity and azimuth is significantly lower. For some source positions though, filtering had much more significant effect (Figure 4.26). For source#6, semblance of scattered waves had a very high value, but no individual scattered phases could be distinguished. In other words, the uncertainty in apparent velocity and azimuth was unacceptable (Figure 4.26a), however filtering reduces this uncertainty significantly (Figure 4.26b).

Array2

The same effect of filtering was observed for the data from the second outcrop array. Figure 4.27 shows the semblance coefficient of direct surface waves for source#4. If compare this result with the value of semblance obtained without filtering (Figure 4.20) and with filtering (Figure 4.27), we observe an increase of 91% in the maximum value of S due to the filtering. Semblance of direct body waves is even more significantly affected by the frequency filtering. An increase of 250% in the maximum value of semblance is observed for source#23 (compare semblance coefficient obtained before and after filtering in Figures 4.21 and 4.28, respectively). Similar effects are observed for scattered waves. For example, for source#23, filtering at 400 Hz leads to an increase of 94% in the maximum value of semblance (compare semblance before filtering (Figure 4.22b), and after filtering (Figure 4.29). In addition, the picks in semblance are associated with different apparent velocities and azimuths.

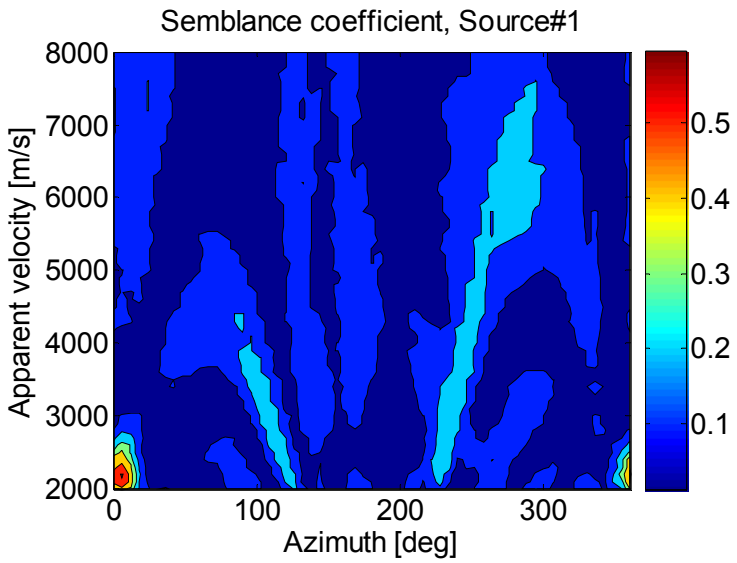

a)

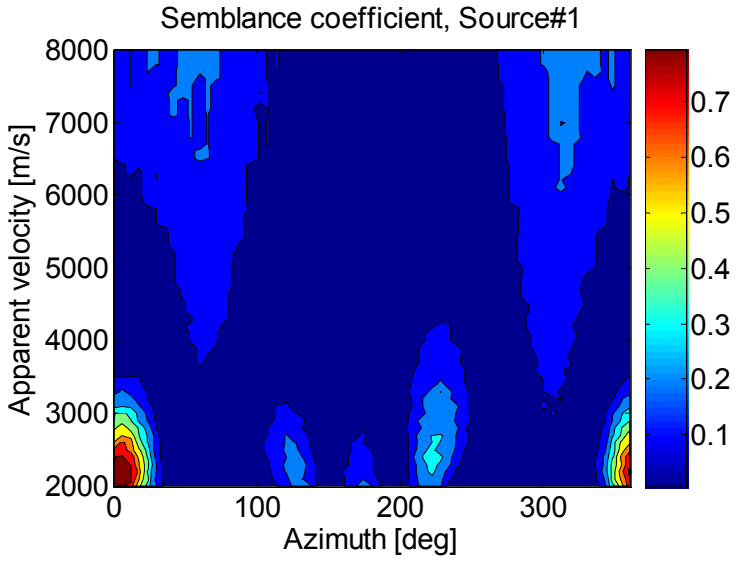

b)

Figure 4.23: Semblance coefficient for direct surface waves, source#1, Array1, calculated (a) before filtering; (b) after 200 Hz Gaussian filter. The filtering at the frequency of the direct surface waves leads to an increase in the maximum value of the semblance coefficient of 25%.

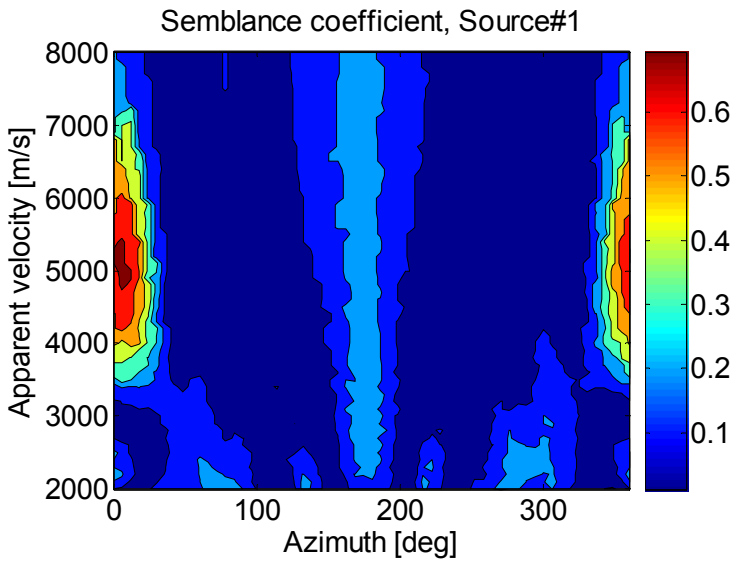

Figure 4.24: Semblance coefficient for direct body waves, source#1, Array1, calculated from data filtered at 400 Hz central frequency (Gaussian filter). The maximum value obtained here is the same as for the case of no filtering (see Figure 4.18), but the uncertainty in defining the apparent velocity and azimuth of the *P*-waves is much higher.

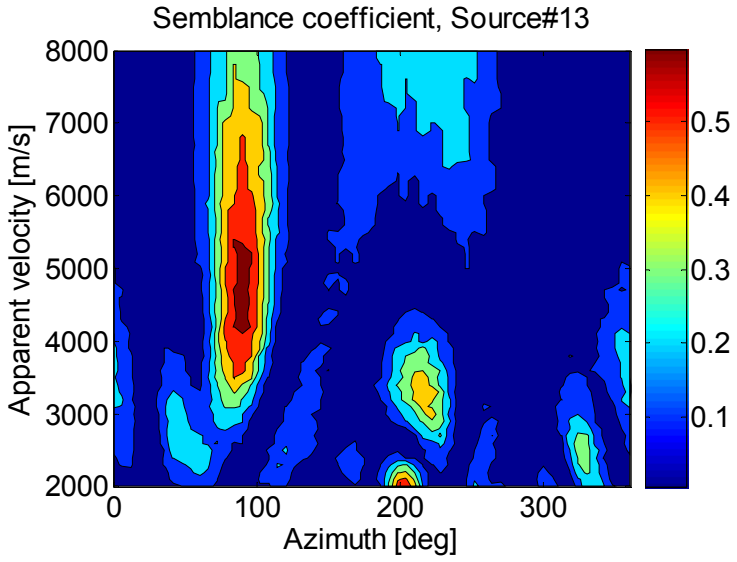

Figure 4.25: Semblance coefficient of scattered waves, source#13, Array1, calculated after 400 Hz Gaussian filtering. The filtering did cause slight increase in the maximum value of the semblance coefficient (compare with Figure 4.19 – no filtering). In addition, here we see one more scattered phase, traveling with apparent velocity of 3000 m/s and azimuth of 210º.

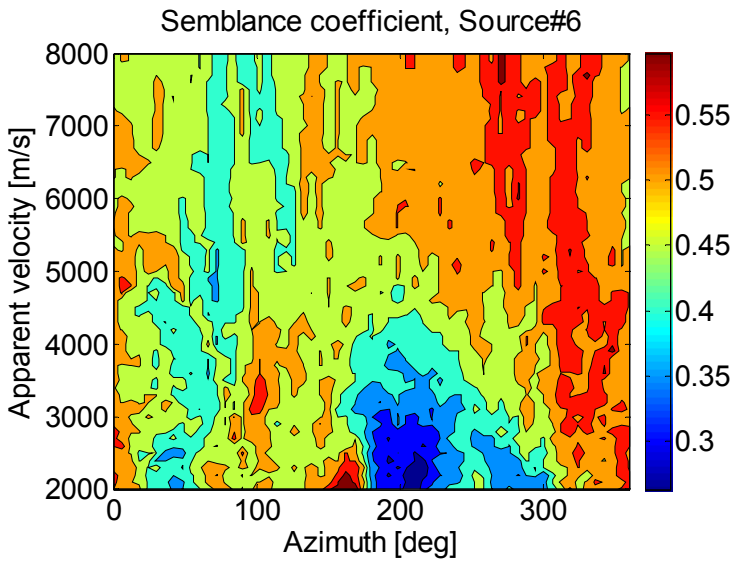

a)

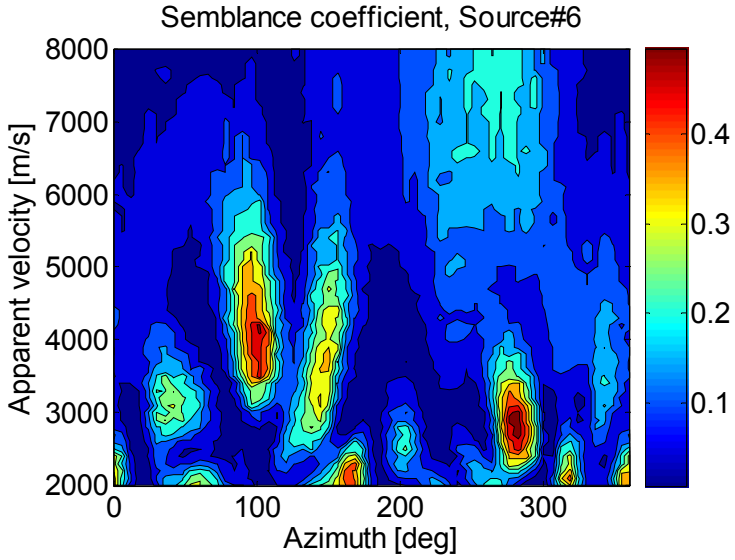

b)

Figure 4.26: Semblance coefficient of scattered waves, source#6, Array1, calculated with (a) no filter applied; (b) applied 400 Hz Gaussian filter. The maximum value of semblance in fact decreases due to the filtering, but so does the uncertainty. While no individual scattered phases can be distinguished before filtering (a), after applying the filter, there are three scattered shear waves that can be identified as traveling with different apparent velocities and in different directions.

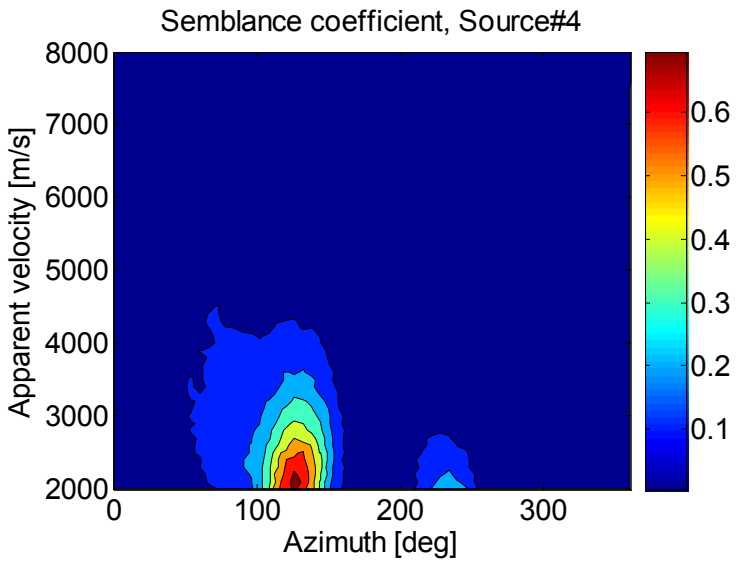

Figure 4.27: Semblance coefficient for direct surface waves, source#4, Array2, calculated after 200 Hz Gaussian filter of the raw records.

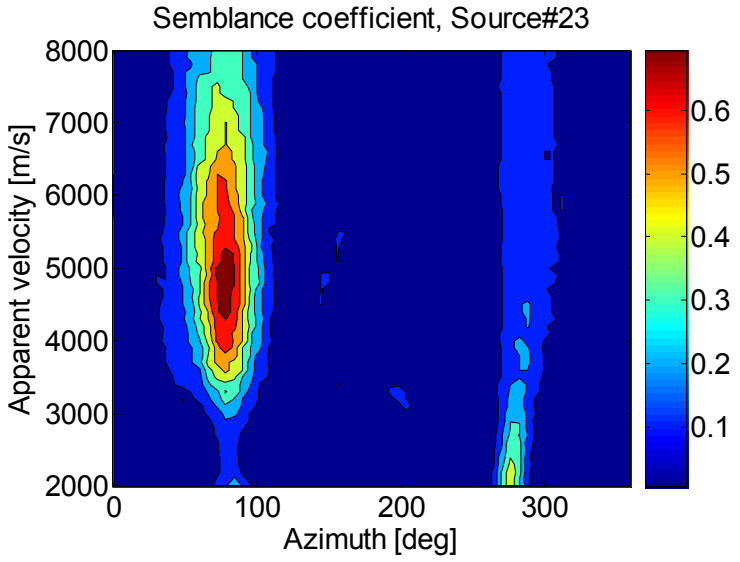

Figure 4.28: Semblance coefficient for direct body waves, source#23, Array2, calculated after 200 Hz Gaussian filtering of the raw records.

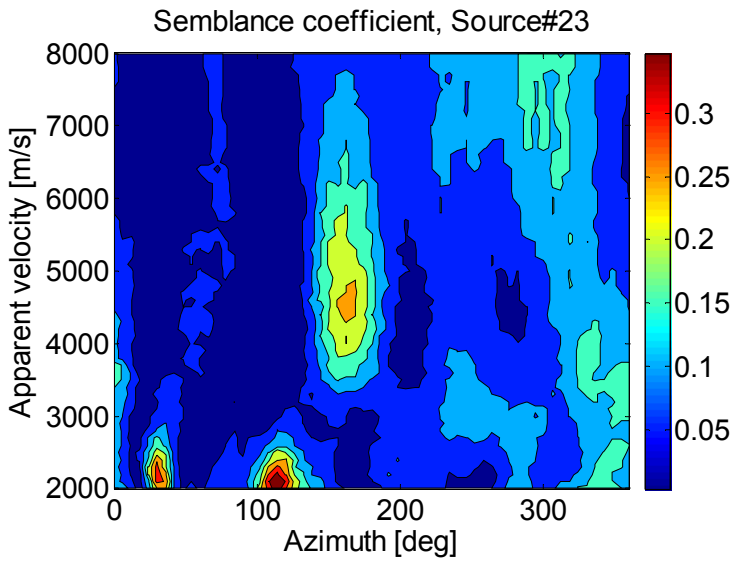

Figure 4.29: Semblance coefficient of scattered waves, source#23, Array2, calculated after data are filtered at 400 Hz (Gaussian filter).

4.6. Data processing of the soil site (Array3)

The semblance algorithm was applied to the data from Array3, which were acquired at a soil site, with a USGS well nearby (see Figure 3.5c for the array geometry and the location of the well). Initially the semblance was calculated without any processing of the raw seismograms. Channels #6, and #14 were excluded from the analysis. Due to the lower frequency content of the data, the time window was initially chosen to be 20 ms wide. The apparent velocity was varied between 200 and 900 m/s (step of 12 m/s). Figure 4.30a shows an example of the semblance plot obtained for source#12. The arrival of the direct surface waves is not marked with a peak in the semblance coefficient. The back-azimuth of source#12 is at 5 degrees, so a maximum of semblance was expected at 185°. The calculation was carried out for time of arrival 0.06-0.07 s, (see Figure 4.5a, for comparison with the raw seismograms). This effect was observed for all source positions. The maximum of semblance corresponding to the

apparent velocity and direction of propagation of surface waves was not observed on any of the semblance plots. The calculation was repeated with time window of 10ms, since previous results from the processing of Array1 and Array2 showed that the narrowing of the time window leads to significant improvement in more precise identification of apparent velocity and azimuth of the incoming direct arrivals. Figure 4.30b shows that semblance did have higher values, but the arrival of direct surface waves was still not observed. The next step was to apply Gaussian filter. We filtered data at 20, 30, 40, 50, and 60 Hz, with standard deviation of 5 Hz. Figure 2.30c shows the effect of a 20 Hz filter on the semblance coefficient. The direct surface waves are marked by a sharp peak (~0.9) of the semblance coefficient, near 185°. The apparent velocity of direct surface waves is defined to be 290 m/s (at 20 Hz). Even though most of the energy was observed at 50-60 Hz (probably due to electrical interference, see spectrum plots on fig. 4.8a), the direct surface waves are having highest semblance coefficient at 20 Hz. Figure 4.31 shows the semblance coefficient calculated for different frequencies, for source#4. Figure 4.32 shows the variation of the maximum value of semblance (taken for a range of velocities between 250 m/s and 350 m/s), as a function of frequency. The same effect was observed for the rest of the source positions. It is independent of source-receiver offset and azimuth. This leads us to the conclusion that direct surface waves have frequency of 20 Hz, and the observed peak at 50-60 Hz is due to electrical interference. To define the frequency of scattered body waves, we filtered the raw seismograms at 70, 80, 90, and 100 Hz. The velocity of direct surface waves was found to be between 260 m/s and 300 m/s. For this reason the velocity of scattered body waves was varied between 350 m/s and 2000 m/s. The tests show that highest semblance with lowest uncertainty is achieved

when data are Gaussian filtered at 100 Hz. Figure 4.33 shows an example of the effect of filtering on scattered waves, for source#1, time of arrival 0.41-0.42 s.

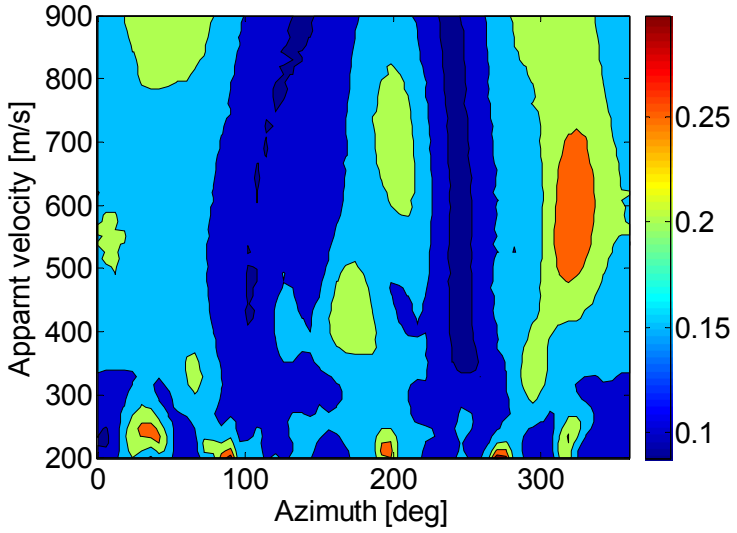

a)

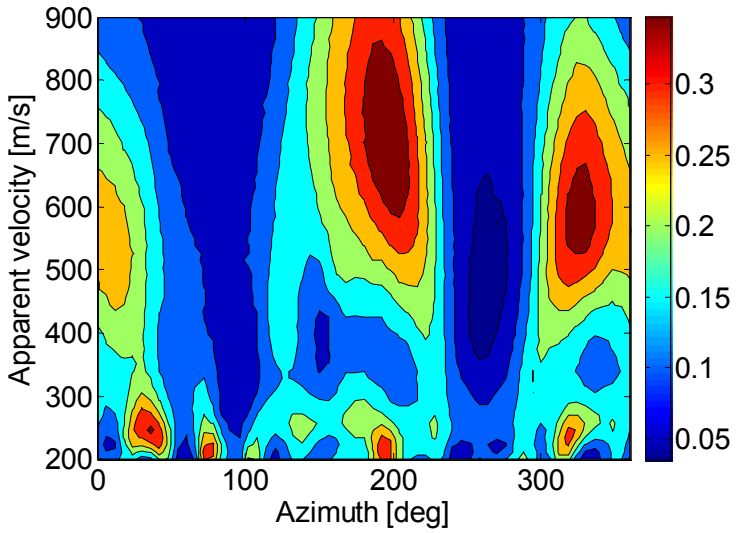

b)

Figure 4.30: Semblance of direct surface waves, source#12, Array3, calculated with a) time window of 20 ms; b) time window of 10 ms.; c) data are filtered at 20 Hz (Gaussian filter), with standard deviation of 10 Hz, time window of 10 ms. The direct surface waves are not identified until narrow filter is applied to the data. All semblance plots are generated for arrival time 0.06-0.07 s. (see Figure 4.5a to compare with raw seismograms).

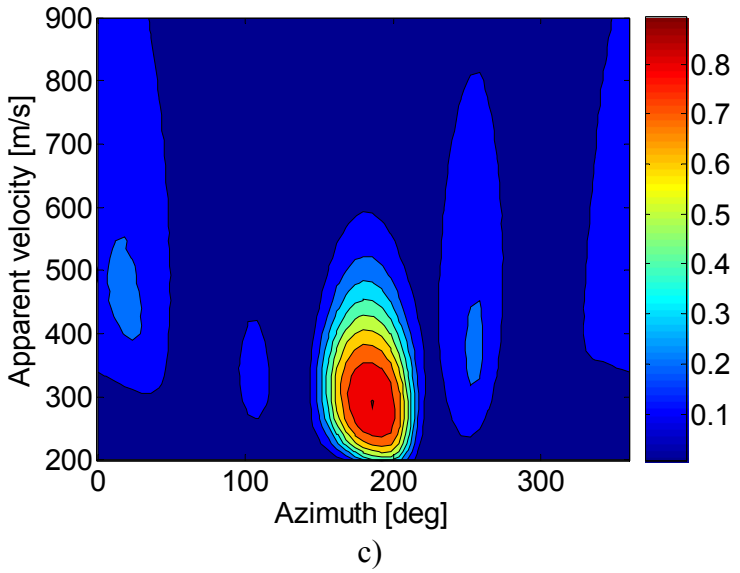

c)

Figure 4.30: Continued

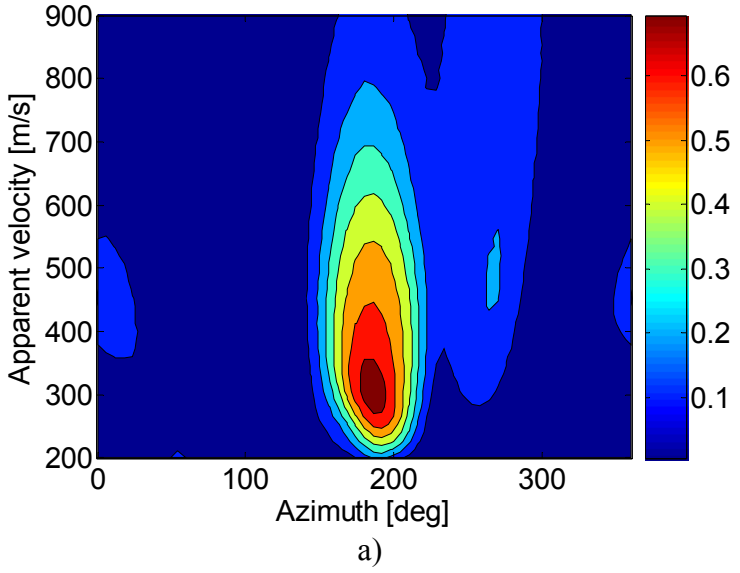

a)

Figure 4.31: Semblance coefficient of direct surface waves, source#4, Array3, calculated for data with a Gaussian filter (5 Hz standard deviation) at a) 30 Hz; b) 40 Hz; c) 50 Hz and d) 60 Hz. The calculation is carried out for time of arrival 0.1-0.11 sec. The semblance coefficient for direct surface waves drops abruptly above 30 Hz, obscuring the direct surface waves. Instead, there are a number of phases arriving with different apparent velocities and azimuths.

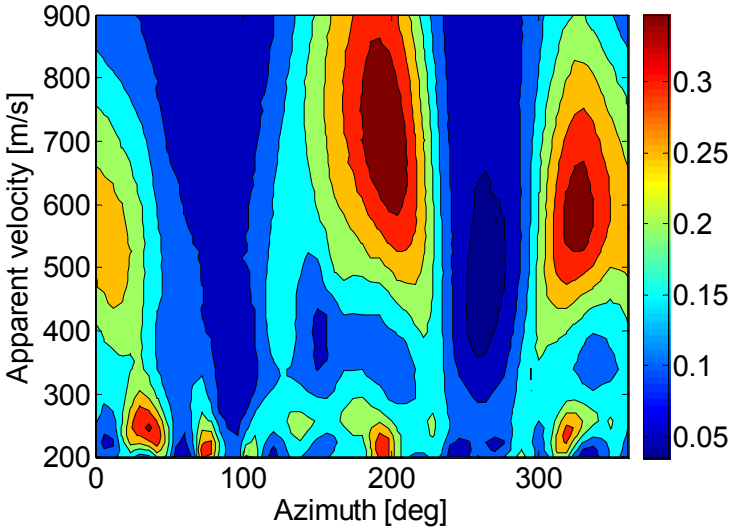

b)

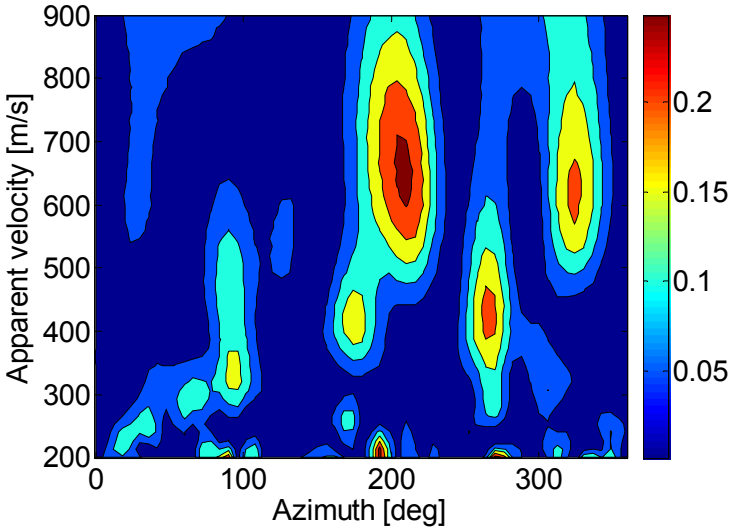

c)

Figure 4.31: Continued

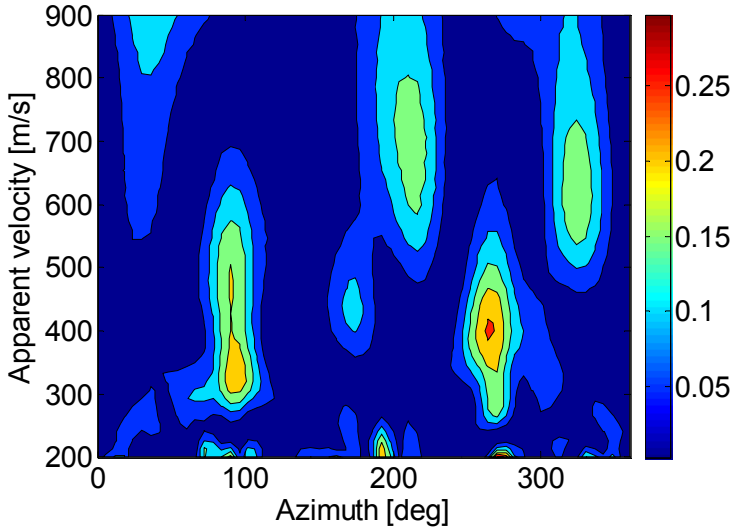

d)

Figure 4.31: Continued

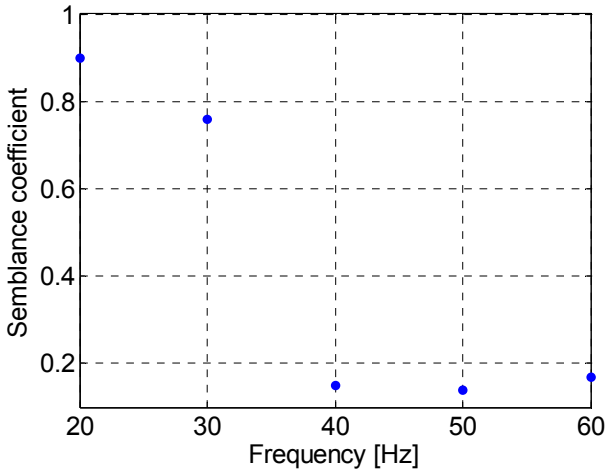

Figure 4.32: Semblance coefficient for direct surface waves, as a function of frequency, source#4, Array3. The maximum of the semblance coefficient is observed at 20 Hz, and it drops abruptly at 40 Hz. This maximum is taken for a range of velocities between 250 and 320 m/s.

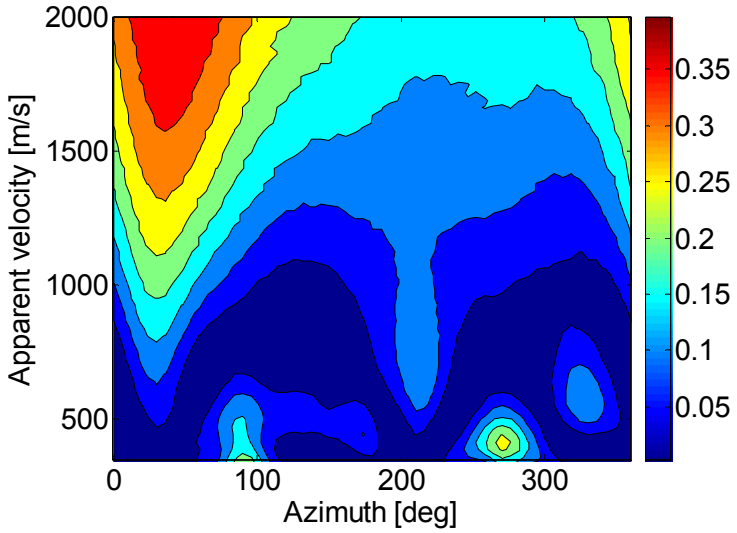

a)

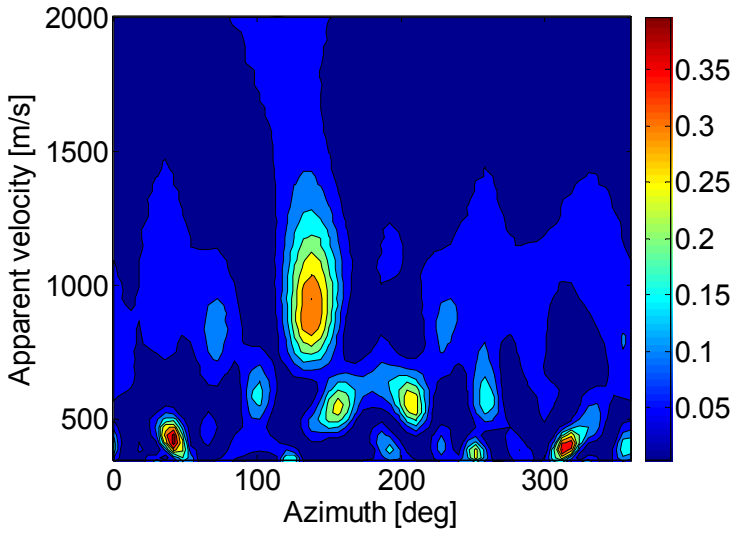

b)

Figure 4.33: Semblance coefficient of scattered waves, source#1, Array3, calculated for time of arrival 0.41-0.42 s. a) data are filtered at 70 Hz; b) data are filtered at 100 Hz;

4.7. Summary

Fig.4.34 presents the effect of all different factors on the direct surface waves, recorded at Array1. The 5ms time window is related to the lowest value of the maximum of the semblance coefficient. It is particularly low for the first four positions of the

source. The narrowing of the time window leads to slight increase in the maximum of semblance for all source positions, except source#1 (it does not change). This increase is 7 % on average, but varies between 0 % and 28 %. The filtering at 200 Hz (which is the frequency of the direct surface waves) has the most significant effect. In fact, it brings all source positions to having maximum semblance near 0.9. The increase compared to the 2ms calculation is on average 17 %, with a minimum of 0 % and a maximum of 54 %. At this point we can conclude that the 2ms window, followed by the filtering of the data is the prerequisite for obtaining high value and low uncertainty semblance plots for direct surface waves. Figure 4.35 shows similar plot for the direct body waves. When data are processed with 5 ms time window, only four source positions show distinct direct *P* or *S* wave arrival. The narrowing of the time window improves the semblance plots significantly, while filtering at 400 Hz additionally increases semblance. Here we observe a decrease though for two source positions. For example for source#12, the highest semblance is observed for 5 ms window, while the filtered data show lowest semblance. It must be noted, that the high maximum semblance at 5 ms is in expense of the resolution. The uncertainty in azimuth and apparent velocity is higher than it is for data obtained with 2ms window and for the filtered data. The same applies to the observed lower semblance (after filtering) for source position#1. An interesting phenomenon in calculating the semblance of body waves is the observed zero semblances (no arrivals) for four of the source positions (#3, 4, 6, and 7). This luck of direct body wave arrivals does not improve with narrowing the time window or applying 400 Hz Gaussian filter to the data. The data from this four source positions were additionally processed with different central frequencies of the Gaussian filter (250, 300, and 350 Hz), but no

improvement was observed. There is nothing peculiar about the spectrum of these data, or the raw seismic records. The lack of improvement could be explained if the time window overlaps the larger surface waves and the semblance is controlled by the surface wave amplitude.

The same test was performed for Array2. The results for direct surface waves are summarized on Figure 4.37. The filtering at 200 Hz leads to a significant increase in the maximum value of the semblance coefficient, just like in the case of Array1. The change between 5 ms and 2 ms window is on average 20 %, but spans between 2 and 62 %. Here, the test is performed for nine source positions (out of 37), with different distances and azimuths with respect to the center of the array. In general, even after filtering, the maximum value of semblance is lower than the values obtained for Array1, for all source positions, except source#37. This, we believe is due to the fact that most source positions for Array2 were much closer to the center of the array (up to 25 m), while most source positions for Array1 were at greater distance from the center. The close positions are probably contaminated with high frequencies that interfere with the direct surface waves. This conclusion is supported by the spectrum of the Array2 data. For the close positions, there are some very high frequencies present, as high as 1000 Hz. The same trend is observed for direct body waves. Because source positions 1, 12, 19, and 28 were at very close distance to the source, the direct *P* (or *S*) waves were not observed.

The same test was performed for semblance coefficient for scattered waves for both Array1 (Figure 4.36) and Array2 (Figure 4.39). For the first array, the filtering at 400 Hz (the frequency of the direct body waves) leads to an increase in the maximum of semblance, on average 94 %. For four source positions (#6, 7, 12, and 14) we observe a

decrease. An example of a semblance plot is shown on Figure 4.26. Even though the maximum of the semblance coefficient is higher before filtering, the uncertainty is so big that no clear scattered phases can be recognized. After filtering, the semblance coefficient drops, but the resolution increases significantly. This was observed for all source positions that showed a drop in the semblance coefficient as a result of the filtering.

The tests performed on the data from Array3, show that clear direct and scattered phases are identified only after subjecting the data to a narrow Gaussian filter. The direct surface waves are found to have a frequency of 20 Hz. The pick at 50-60 Hz on the spectrum of the raw seismograms is contributed to electrical interference. Scattered waves have highest semblance coefficient and lowest uncertainty if filtered at 100 Hz.

In conclusion, when sources of noise can be filtered out and when the spectra and duration of the pulse is known, proper use of window length and filtering can significantly improve the response of the semblance operator. The length of the time window is chosen to be equal to one cycle of the predominant frequency. In doing so, we assume a single cycle wavelet. To obtain images of scatterers using the data collected from Array1 and Array2, seismograms have to be filtered at 400 Hz, and the time window must be 2ms. To obtain images of scattered waves from the soil site (Array3), the seismograms must be filtered at 100 Hz, and the time window to be at 10ms. These are the input parameters that will be used to obtain 3-D images, for each of the field sites. The results will be presented in the next chapter.

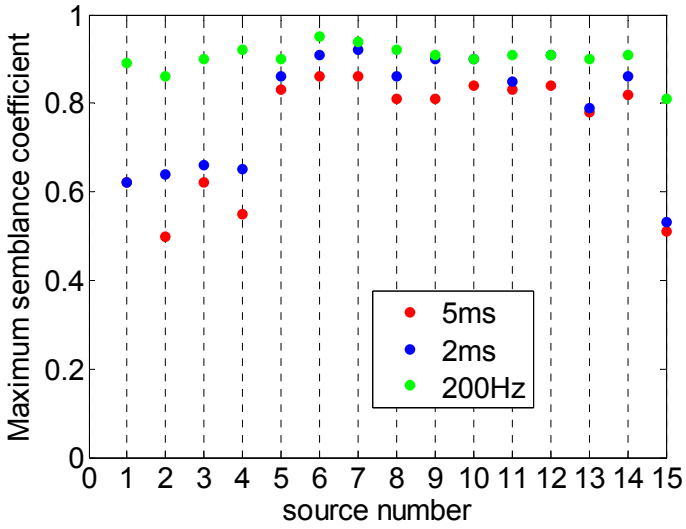

Figure 4.34: Effect of different factors on the maximum value of the semblance coefficient for direct surface waves, Array1. The red dots denote the values of the maximum of semblance for each source position, when calculations are performed with 5ms time window, blue dots correspond to 2 ms time window, and green dots correspond to filtered data at 200 Hz (frequency of direct surface waves).

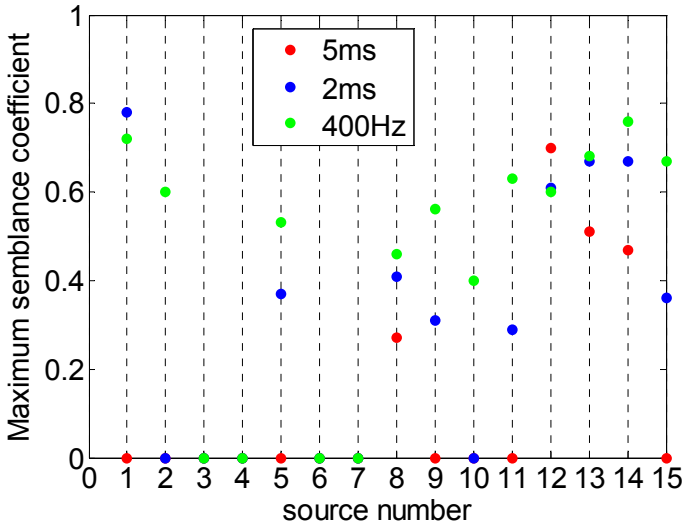

Figure 4.35: Effect of different factors on the maximum value of the semblance coefficient for direct body waves, Array1. The red dots denote the values of the maximum of semblance for each source position, when calculations are performed with 5 ms time window, blue dots correspond to 2 ms time window, and green dots correspond to filtered data at 400 Hz (frequency of direct body waves). Some of the values of semblance are showing to be zero, which means that no body waves were distinguished on the semblance plots for that source position.

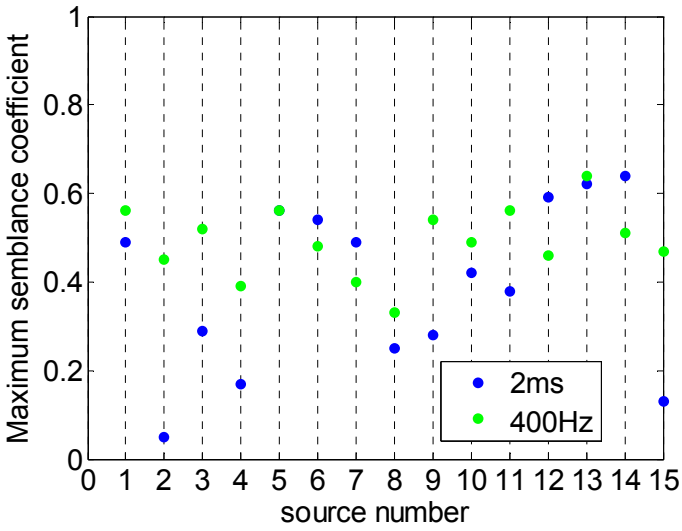

Figure 4.36: Effect of filtering on the maximum value of the semblance coefficient for scattered waves, Array1. The blue dots correspond to 2ms time window, and green dots correspond to filtered data at 400 Hz.

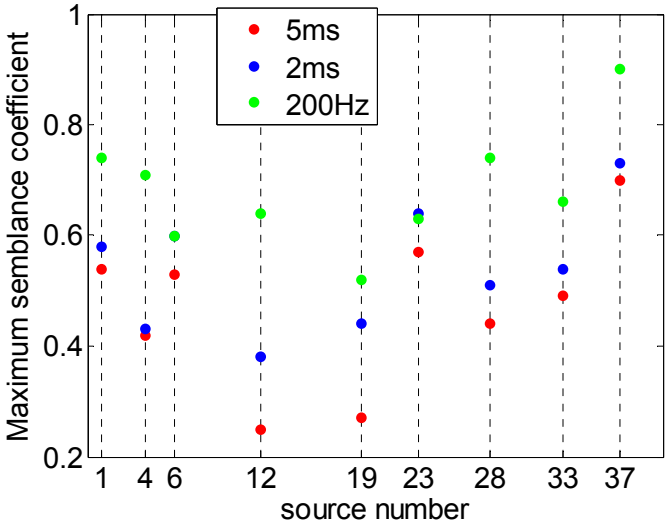

Figure 4.37: Effect of different factors on the maximum value of the semblance coefficient for direct surface waves, Array2. The red dots denote the values of the maximum of semblance for each source position, when calculations are performed with 5 ms time window, blue dots correspond to 2 ms time window, and green dots correspond to filtered data at 200 Hz (frequency of direct surface waves).

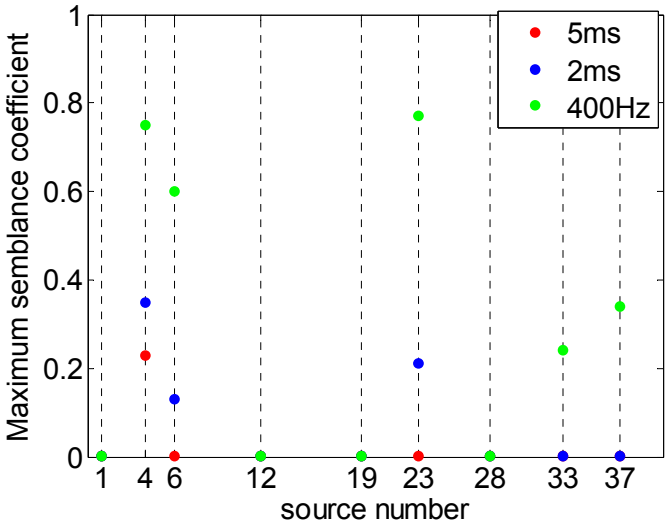

Figure 4.38: Effect of different factors on the maximum value of the semblance coefficient for direct body waves, Array2. The red dots denote the values of the maximum of semblance for each source position, when calculations are performed with 5 ms time window, blue dots correspond to 2 ms time window, and green dots correspond to filtered data at 400 Hz (frequency of direct surface waves). Some of the values of semblance are showing to be zero, which means that no body waves were distinguished on the semblance plots for that source position.

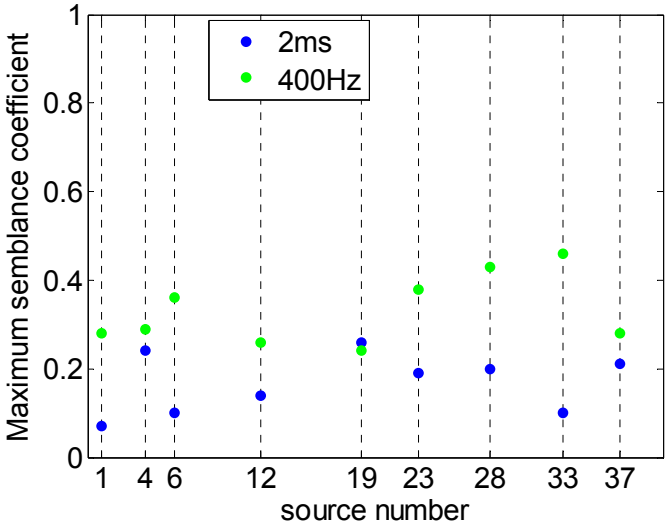

Figure 4.39: Effect of filtering on the maximum value of the semblance coefficient for scattered waves, Array2. The blue dots correspond to 2 ms time window, and green dots correspond to filtered data at 400 Hz (frequency of direct body waves).

CHAPTER 5

THREE-DIMENSIONAL IMAGING ALGORITHM

5.1. Description of the semblance-based imaging algorithm

The second part of the semblance-based imaging technique was to project the semblance coefficient, obtained as a function of arrival time, apparent velocity and azimuth (described in Chapter 4) into a 3-D grid. Only significantly large semblance coefficients provide meaningful evidence of scattering objects. For this reason, the first step here was to determine the minimum threshold for a meaningful semblance coefficient. Douze and Laster (1979) found a threshold of 0.1. The same threshold was determined by Bannister and Melhuish (1997), using the background noise level. Here we adopted the same criteria.

Each value of the semblance coefficient is defined by time of arrival, apparent velocity, and azimuth. To image the scatterers we assumed single scattering and constant seismic velocity. Significant velocity changes would require ray tracing to associate arrival times of scattered waves. Each scattering point was imaged as a point along a constant travel-time ellipse with foci defined as the source and the center of the geophone array (Figure 5.1). The semimajor and semiminor axes a and b, are calculated as follows:

$$a = \frac{tv}{2},\ b = \sqrt{a^2 - f^2} \qquad \text{(eq.5.1)}$$

Where v is the apparent velocity of the seismic waves, t is the time of arrival, and f is half the distance between the two foci. The 3-D location of the scatterer is defined by distance and azimuth with respect to the center of the geophone array. The distance that the

scattered wave travels is from source to scatterer to receiver, i.e. this is the distance from one focus to a point along the ellipse to the second focus (Figure 5.1). The back-azimuth of the semblance coefficient defines the direction from which the wave arrives, i.e. the direction of the scatterer with respect to the center of the array. In order to define the third dimension - the depth of the scatterer, we used the relationship between true and apparent velocity:

$$\sin(i) = \frac{v_{true}}{v_{apparent}} \qquad \text{(eq5.2, (Aki and Richards 2002))}$$

where i is the angle of incidence, i.e. the angle between the wave front and the vertical to the spread of geophones (Figure 5.2). The dip θ will be 90º-i. The true velocity will be the velocity of waves propagating parallel to the array (at θ=0º, Figure 5.2c).

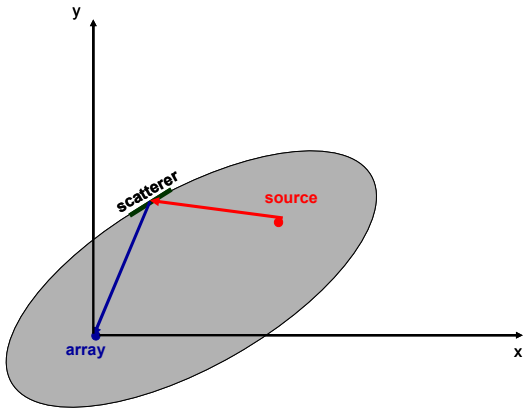

Figure 5.1: Principle of imaging of scatterers. The arrival time, and the apparent velocity of a scattered wave defines the semimajor axis of an ellipse with the center of the geophone array in one of its foci, and the source at the other focus. The distance traveled by the scattered wave is the distance from the source (red dot) to the scatterer (green line) to the receiver (blue dot). The direction from which the scattered wave arrives is defined by high values of the semblance coefficient.

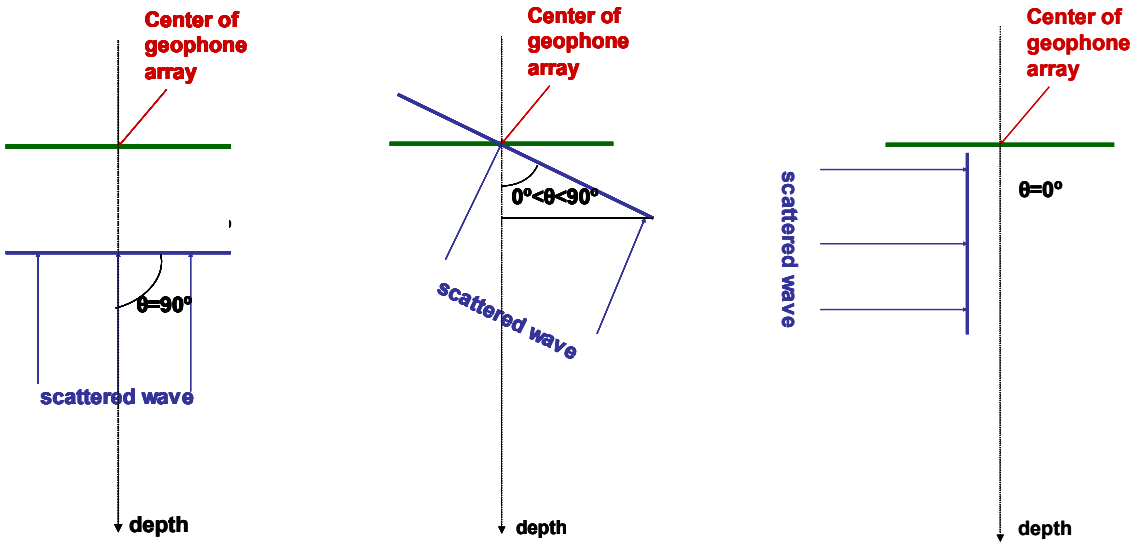

a) b) c)

Figure 5.2: The angle of incidence i of the ray path that is used to define the depth of the scattering point, is determined by the ratio of true to apparent velocity (eq.5.2). (a) for θ=90º, the apparent velocity approaches infinity; (b) for dips less than 90 degrees the $V_{app}>V_{true}$; (c) for θ=0º V_{app} is equal to the true velocity; The horizontal green line represents the earth surface, the thin black line is the vertical with respect to which the wave incidence is measured.

Defining the true velocity for the outcrop data (Array1 and Array2)

We used a few semblance plots (obtained for Array1) with clear strong semblance values for arrivals of surface, P, and S phases, and we calculated the average of these peak semblance coefficients as a function of apparent velocity (Fig. 5.3). The average is a proxy for the frequency of occurrence of strong semblance values at each velocity. The contributions from each phase is clearly observed on that plot as a characteristic distribution in frequency-of-occurrence of semblance values as a function of apparent velocity. At 2100 m/s the maximum in the frequency-of-occurrence curve corresponds to surface waves. A peak in the frequency of occurrence of the semblance coefficients for an apparent velocity of 3300m/s corresponds to scattered shear waves. The frequency of occurrence curve for S-wave semblance coefficients has a minimum at 2700 m/s and this

was used as a lower bound and hence true velocity for the shear waves. The upper bound for the shear waves was chosen to be 4300m/s. At this apparent velocity and higher, the P waves contribute to the semblance coefficients and cannot be distinguished from the S waves. Because, on vertical geophones, the shear wave at near-vertical incidence should exhibit only weak signals the contributions from S waves at apparent velocities above 4300m/s should be minimal. The P wave's minimum frequency-of-occurrence of semblance values occurres at an apparent velocity of 4400m/s. This is the lower bound for the P wave apparent velocity. The upper bound is unlimited, but set here at 8000m/s for computational simplicity.

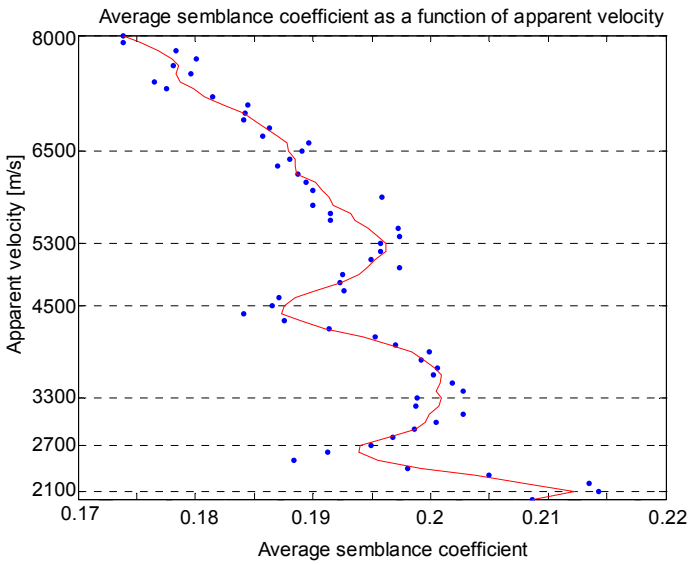

Figure 5.3: Average of peak semblance coefficients (a proxy for frequency-of-occurrence) as a function of apparent velocity. Blue dots denote average semblance for each velocity value, the red line is a five point moving average.

Generating 3-D images

Seismic waves traveling within exposed and unweathered granite exhibited little variation in velocity and hence a homogeneous velocity model is an appropriate assumption. We generated 3-D semblance images using both P and S waves. The image volume was broken into blocks and the semblance images consisted of the average semblance value for waves scattered in each block. The semblance coefficient was calculated first as a function of apparent P or S velocity. For computation, the dip of the ellipse was varied with a step of two degrees. The semblance coefficient is calculated for a range of apparent velocities that are dependent on the true velocity (i.e. the homogeneous velocity). Initially the 3-D images were obtained based on a full range of dips (from 0 to 90º). Because some very high coherence noise for apparent velocity on the order of a few tens of km/s were observed (at θ=90º), we restricted the dip for P waves to vary from 0 to 60º. The dip for S waves was restricted to vary between 0º and 52º, so the apparent velocity of shear waves would be in the range of 2700 m/s and 4300 m/s.

The resolution of the 3-D images was defined by the ¼ wavelength criteria (Kearey and Brooks, 1991). The dominant frequency for body waves was 400Hz, with velocity of propagation of 4400m/s for P waves and 2700m/s for shear waves. From here, we have wavelength between 11 and 7m. The grid size was set to 3x3m. The semblance coefficient in each grid cell is calculated as average semblance normalized by number of hits for that cell. For this reason the maximum semblance from the three-dimensional images (0.14) is much lower than the maximum semblance from the individual semblance plots (0.9).

5.2 Images from the granite outcrop

Surface Waves

We used scattered surface waves, recorded by Array1 to image surface scatterers over an area of 100x100 m. This image was generated for waves traveling with velocity of 2100m/s and arriving after the end of the near-source reverberations. The grid size was chosen to be 5x5m, based on the ½ wavelength criteria for surface waves (Kearey and Brooks, 1991). The predominant frequency of surface waves was 200 Hz, and their apparent velocity of propagation was 2100 m/s, hence the dominant wavelength is 10m. A few zones of high scattering (i.e. high semblance coefficients) were observed (Figure 5.4, shown in red). The strongest zone of scattering was observed at about 20m north of the array. This correlates with the location of a small creek, which runs at the bottom of the outcrop. In addition, we observe a few other areas of high semblance. One is about 20m from the array, in N65E direction – it correlates with the location of a small ridge (about 4m long). An exfoliation sheet (about 10m long and 3-4m high) is identified by a zone of scattering east of the array. Two tree islands, 40-50m from the array, in E65S direction, are also identified. These results are further discussed in Chapter6.

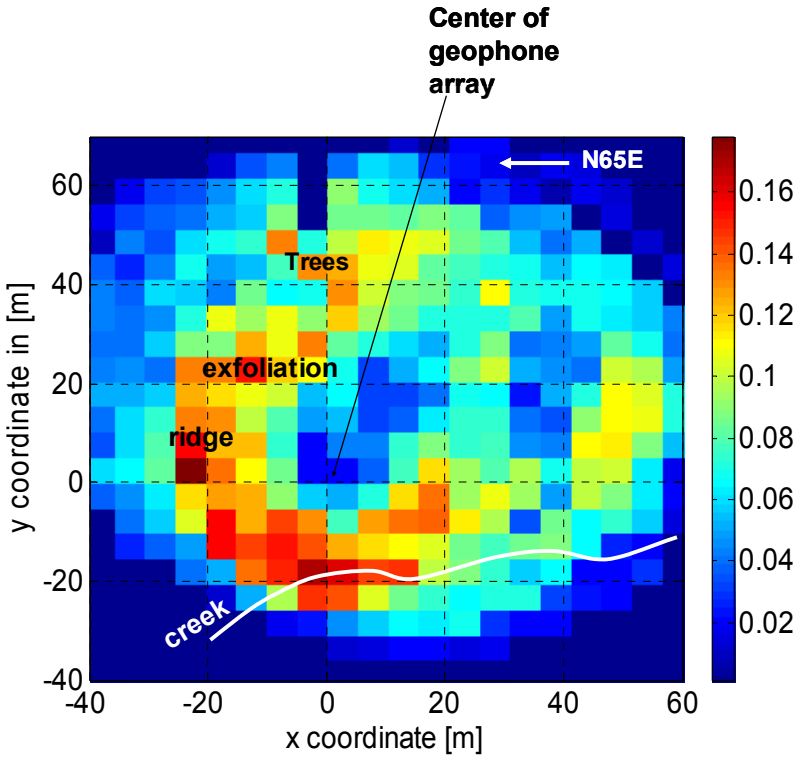

Figure 5.4: Image of surface scatterers. The color bar denotes the value of the normalized semblance coefficient. Red and blue areas show strong scattering (high semblance) and low-to-no scattering, respectively. A few zones of strong scattering are observed with the biggest below a small creek (white). A 4m long ridge is identified NE from the center of the array, exfoliation sheet (10m long and 3-4m high) is marked by a zone of scattering east of the array. Two tree islands are also identified 40-50 m south of the array.

Body Waves

The average semblance coefficient from P and S waves, for different depths was generated initially without filtering of the raw data. Figure 5.5a,b shows the result for two different depths – 5m and 20m. Besides the strong zone of scattering, associated with the location of the small creek (20m in north direction with respect to the center of the array), there are two other zones that are located at distances of 50m and 80m from the center of the array, in E65S direction. This was the reason for making the decision to acquire additional data (Array2), with source and geophone positions near these two zones. Later, we found out that the narrow Gaussian filtering leads to much better resolution in

identifying scattered phases (as was discussed in Chapter4). Images obtained after filtering at 400Hz are shown on Figure 5.5c,d. These images show much more detail in identifying different zones of scattering, and most importantly, the two zones in E65S direction are not present. These results correlate with the semblance images obtained after processing the data acquired with Array2 (Figure 5.6). There is very low scattering observed south of the array.

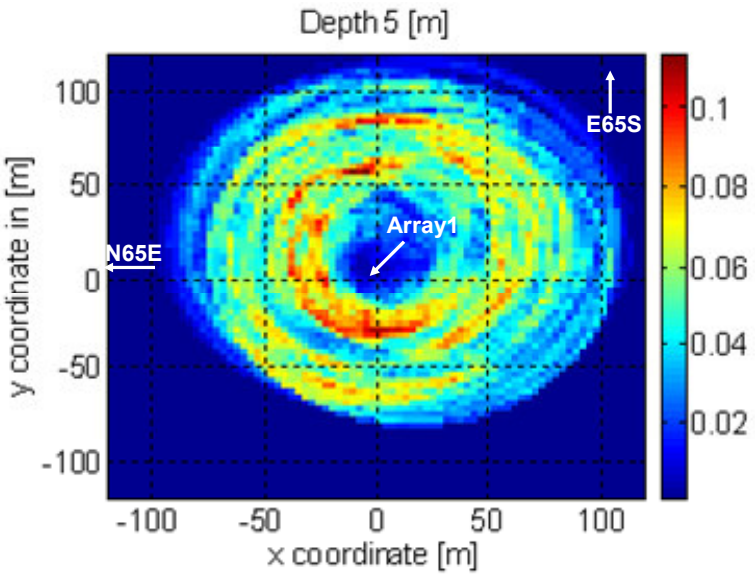

a)

Figure 5.5: (a) average semblance from P and S waves, at 5m depth, without filtering; (b) average semblance from P and S waves, at 20m depth, without filtering; (c) average semblance from P and S waves, at 5m depth, with a 400 Hz Gaussian filter; (d) average semblance from P and S waves, at 20m depth, with a 400 Hz Gaussian filter.

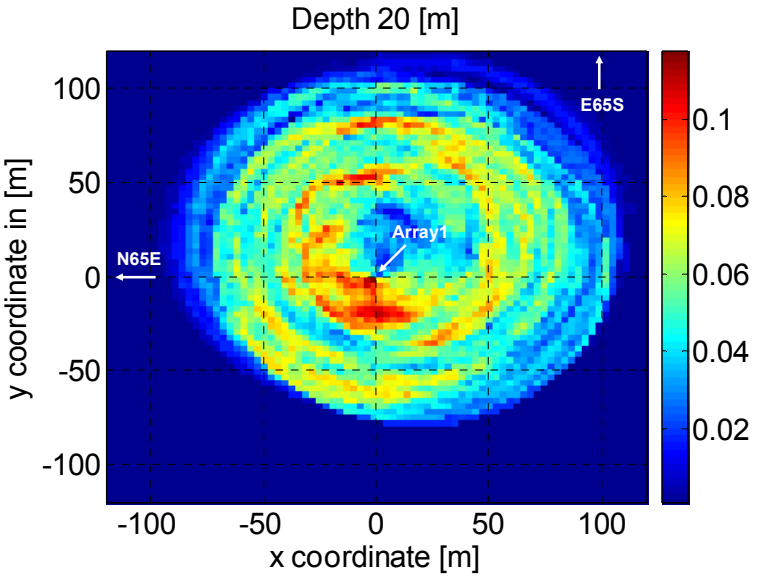

b)

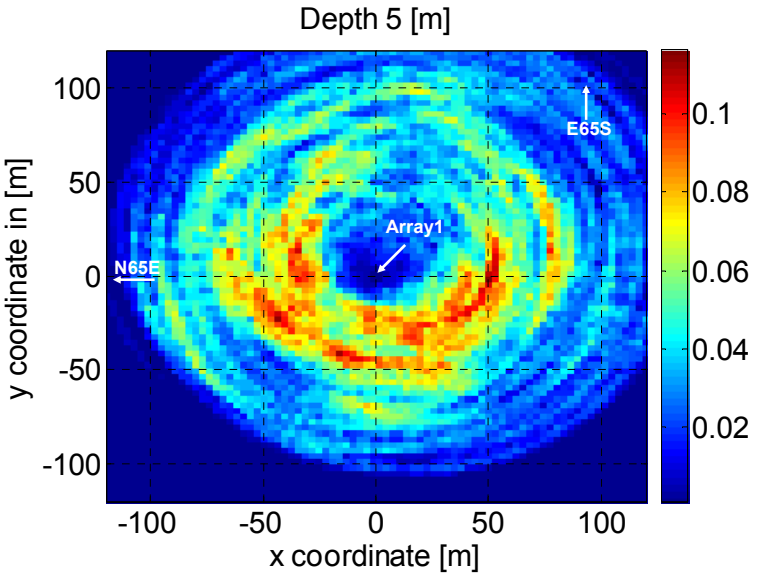

c)

Figure 5.5: Continued

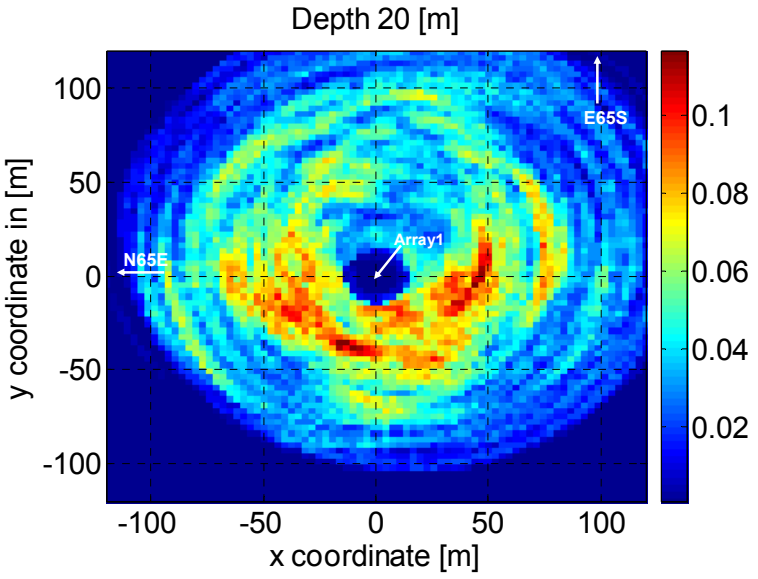

d)

Figure 5.5: Continued

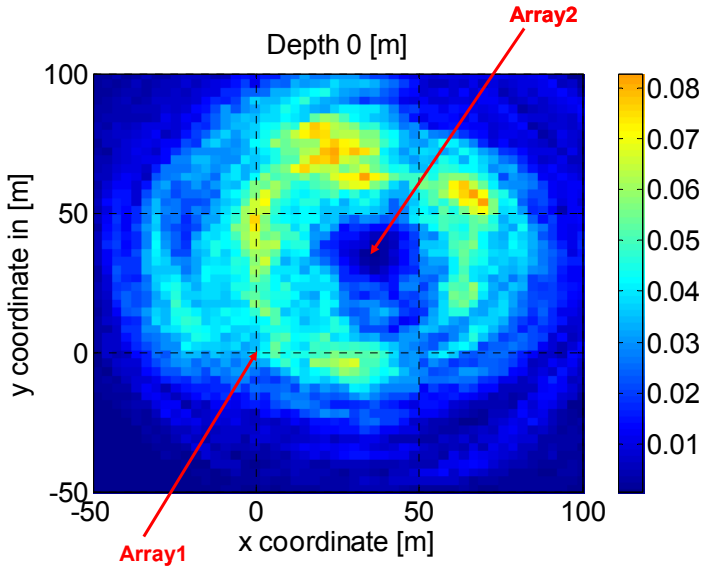

a)

Figure 5.6: Depth images obtained from Array2. (a) at 0m depth, red arrows denote the locations of the centers of Array1 and Array2; (b) at 5m depth (compare with fig.5.3a – the image obtained from Array1); (c) at 20m depth (compare to fig.5.3.b – the image obtained from Array1).

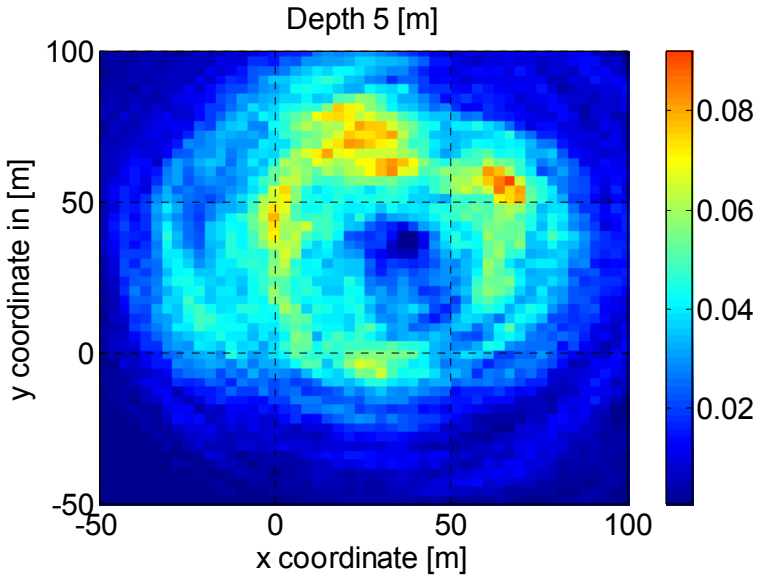

b)

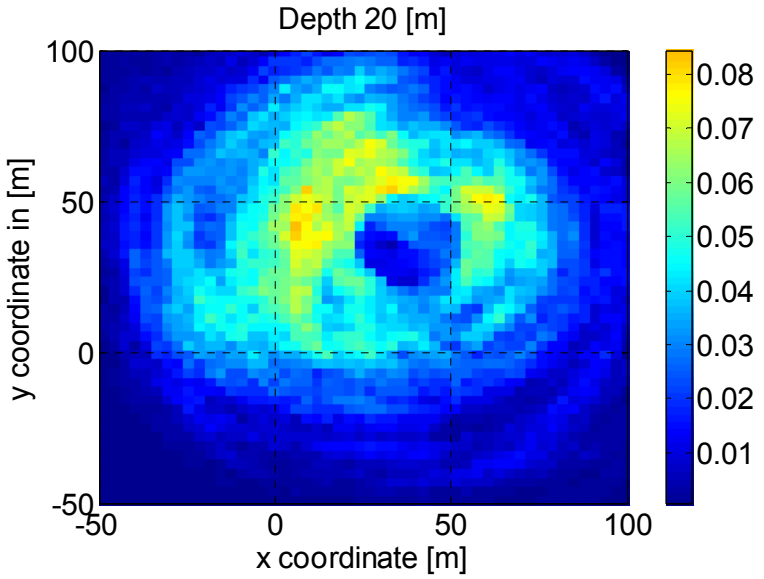

c)

Figure 5.6: Continued

The images of the subsurface scatterers show correlation with the subsurface geology of the study area. Figure 5.7a shows a vertical cross-section along E65S direction, down to a depth of 40m. The area around the creek is the strongest zone of scattering. This area is considered to be controlled by a zone of joints and fractures

(further discussed in Chapter6). Figure 5.7b shows a vertical cross-section along N65ºE direction, which is nearly parallel to the creek (N55ºE). This cross-section is also taken at distance of 20m from the center of the array, i.e. coincides with the location of the creek. We see here a more continuous zone of scattering, along the cross-section, and also in depth. Figure 5.8 shows that the scattering from the creek is connected to other scattering zones that span a range of nearly 180 degrees (from east to west). Cross-sections at distance of 50m (and -50m) from Array1, in E65S direction show scattering as strong as the one from the creek. To obtain a clearer image of the connection between these zones, we plotted an image of the semblance coefficient ≥0.09 (Figure 5.9). In fact, we observe continuity of the scattering areas over a range of 180 degrees, which is particularly prominent at depth of 30m. This "semi-ring" of high scattering is further discussed in Chapter6, as related to the available geological data for the area.

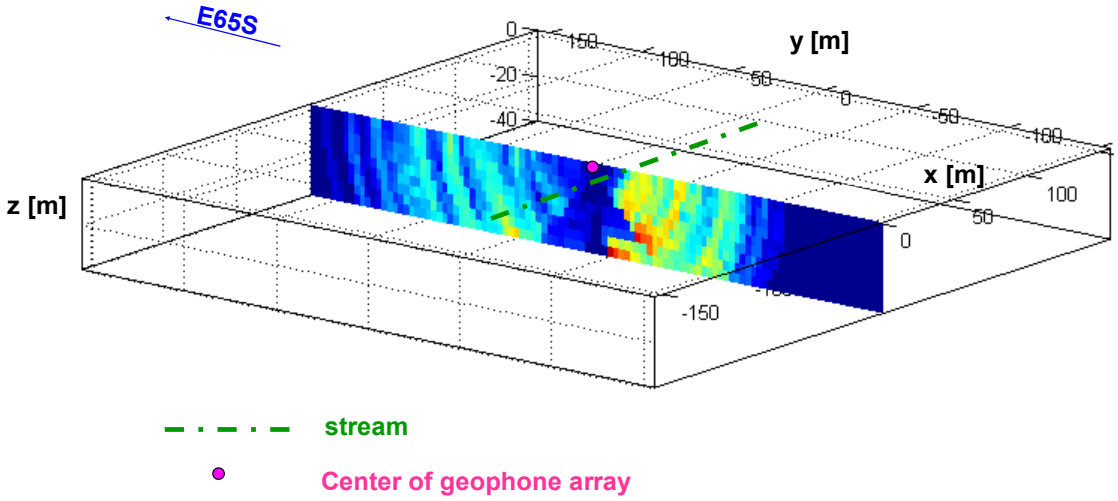

a)

Figure 5.7: Scattering cross-section along a) E65S, red stands for high semblance coefficient (i.e. strong scattering), blue stands for low semblance. Green dashed line shows the location and orientation of the stream. The pink dot denotes the location of the center of Array1; b) cross-section along N65E, the creek is oriented N55E.

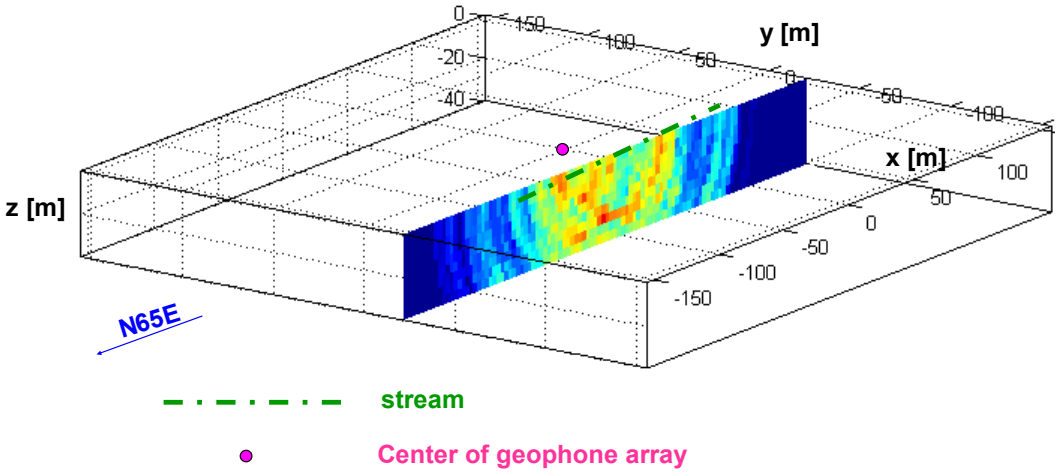

b)

Figure 5.7: Continued

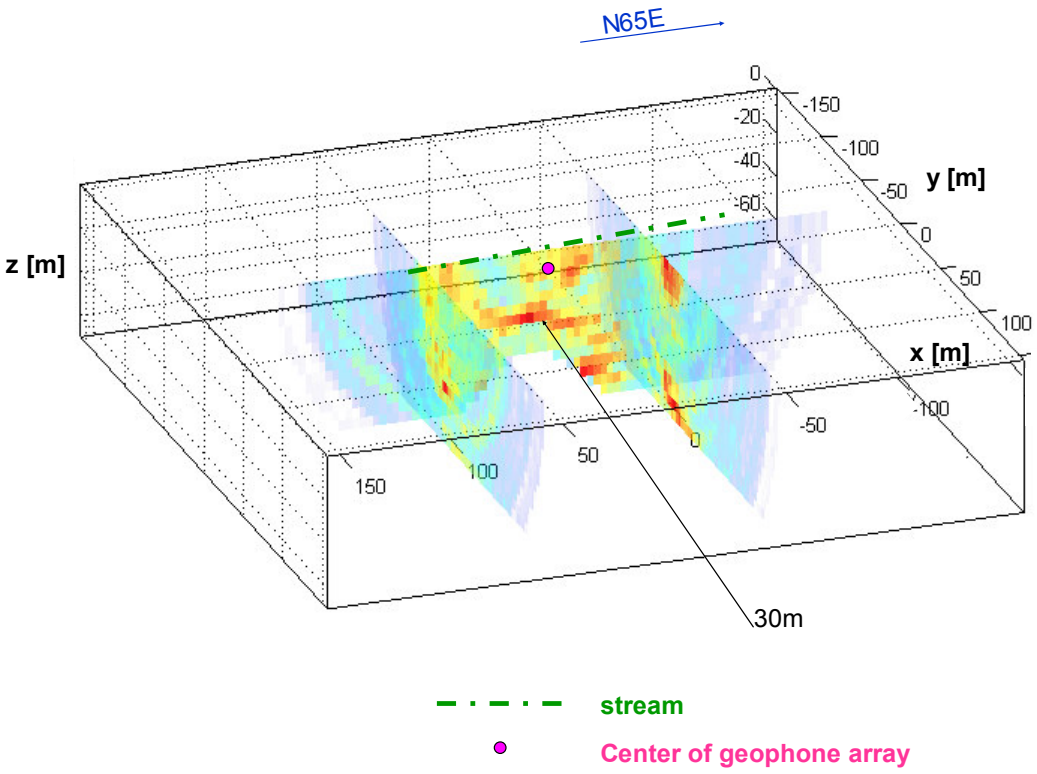

Figure 5.8: Three cross-sections (one at N65E, and two at E65S). Green dashed line shows the location and orientation of the stream. The pink dot denotes the location of the center of Array1.

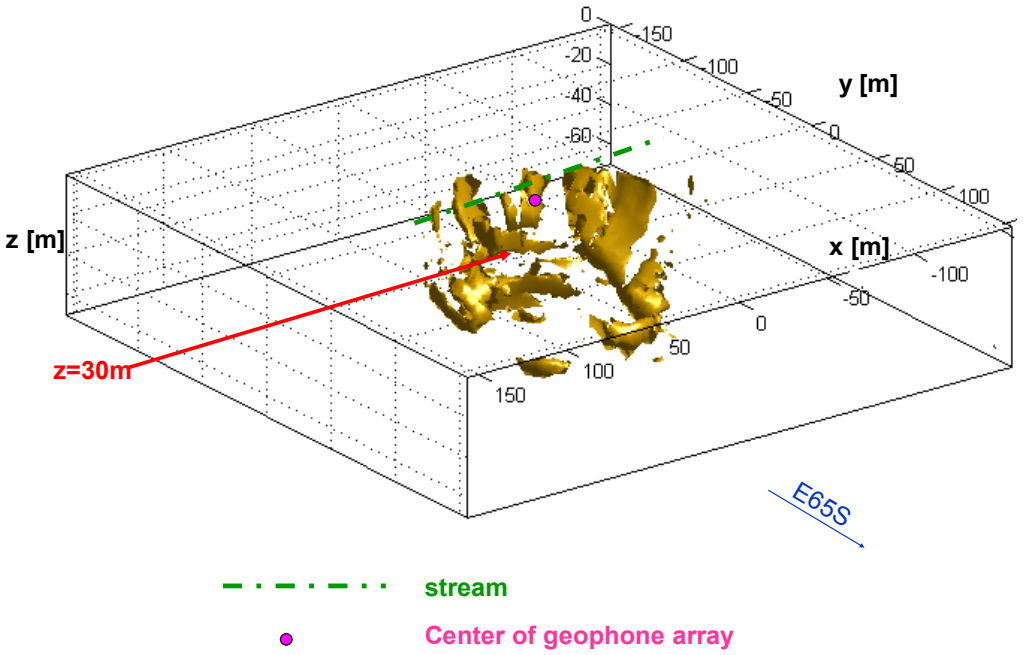

Figure 5.9: 3-D image of the average semblance coefficient (≥0.09). Green dashed line shows the location and orientation of the stream. The pink dot denotes the location of the center of Array1.

5.3. Images from the soil site

Available well data from the soil site suggest that the velocity structure exhibits strong vertical variation. The top 7.3m consist of unsaturated saprolite. Below the water table at 7.3m, the saprolite extends down another 7.9m. The bedrock is at depth of 15.2m, and a subhorizontal fracture is observed at depth of 22.5m (Williams, 2006). The semblance imaging technique described here is assuming a homogeneous velocity model, which is clearly inconsistent with the described velocity structure at the soil site. The semblance coefficient, calculated for body waves (filtered at 100Hz, Gaussian filter) shows maximums at 750m/s and 450m/s at the time of arrival of direct P and S waves, respectively. This was used as a reference for the velocity in the saprolite, necessary to be applied to the 3-D imaging algorithm. We assumed that for waves traveling with apparent velocity of 750m/s, we should be able to image at least the water table, because we assumed that it is overlaid by a homogeneous layer of saprolite. Because 750m/s is the apparent velocity of P waves, the true velocity will be lower. We generated 3-D images of scattered P waves at 550m/s, and 650m/s. Both models failed to image the water table. Figure 5.10 shows 2-D images obtained for true velocity of 550m/s, at 0, 5, and 20m depth. Two areas are showing strong scattering, starting at the earth's surface and continuing down in depth. We do not see a continuous reflection at depths of 5 to 10m, associated with the water table. Similar results were obtained with 650m/s true velocity.

In an attempt to image the fracture at 22.5m depth, we generated 3-D images, assuming 750m/s velocity in the first 7.3m of unsaturated saprolite, 1500m/s in the saturated layer below it, and 2000m/s in the bedrock. This leads to an average apparent velocity of 1400m/s. The images were generated for average true velocity of 1100m/s,

and 1200m/s. Figure 5.11 shows three depth slices at 1200m/s true velocity. These images look very different than the ones obtained with 550m/s true velocity (Figure 5.10). The only zone of strong scattering is near the well, and it is continuous with depth. Scattering is slightly higher at 5m and 20m, than at the surface and at intermediate depths.

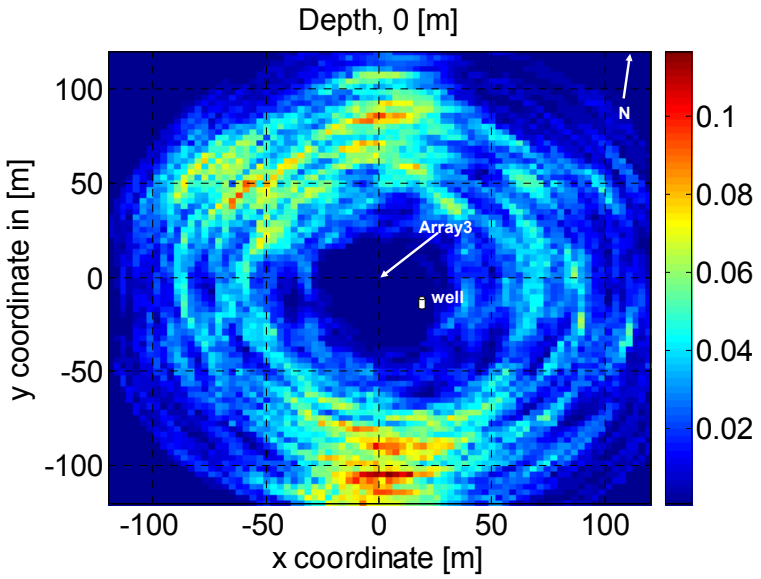

a)

Figure 5.10: 2-D depth images of the semblance coefficient of scattered P waves, true velocity is 550m/s, Array3. The center of the array is denoted by a white arrow, and the well location – by a white cylinder; (a) at 0m depth; (b) at 5m depth; (c) at 20m depth.

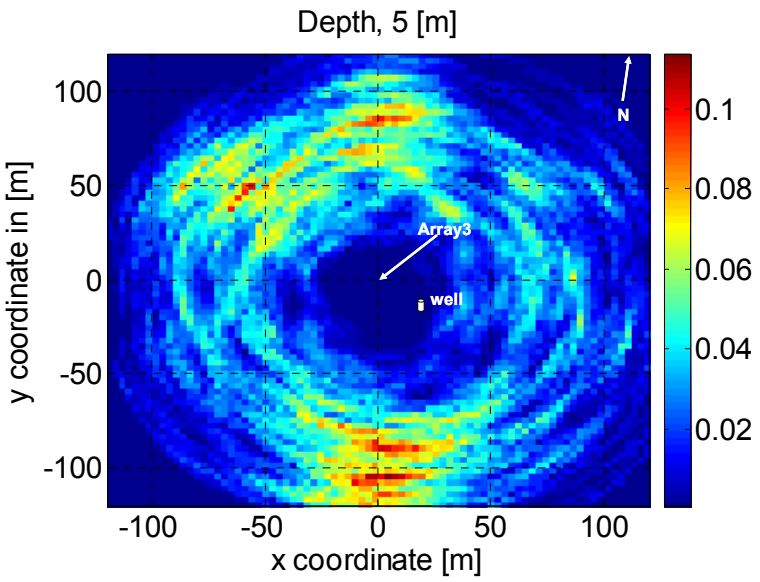

b)

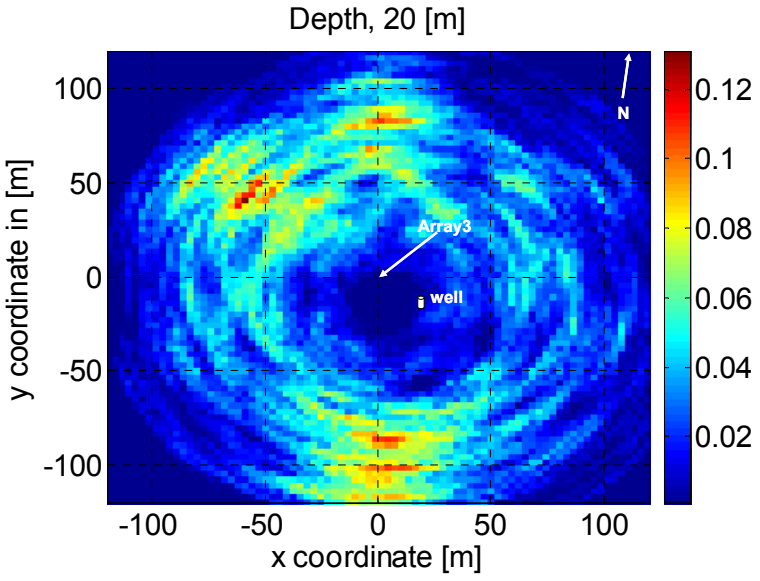

c)

Figure 5.10: Continued

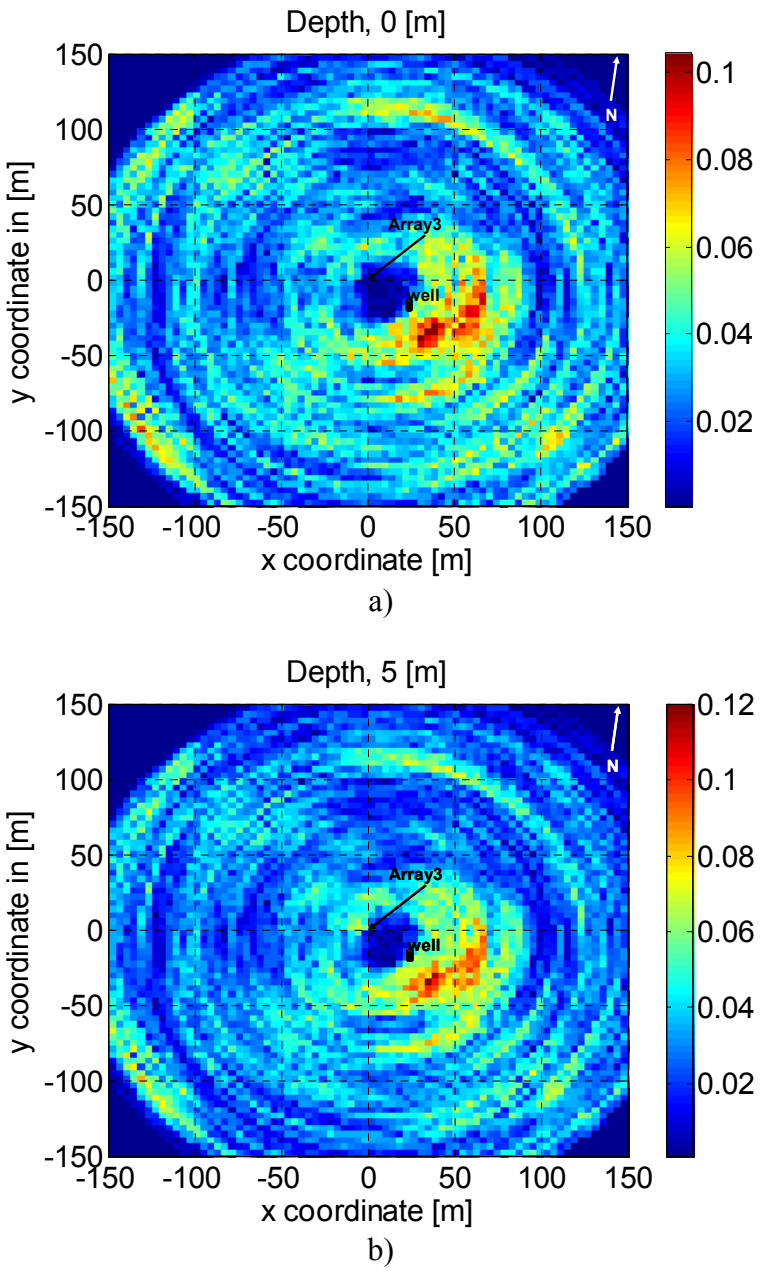

Figure 5.11: 2-D depth images of the semblance coefficient of scattered P waves, true velocity is 1200m/s, Array3. The center of the array is denoted by a black arrow, and the well location – by a black cylinder; (a) at 0m depth; (b) at 5m depth; (c) at 20m depth.

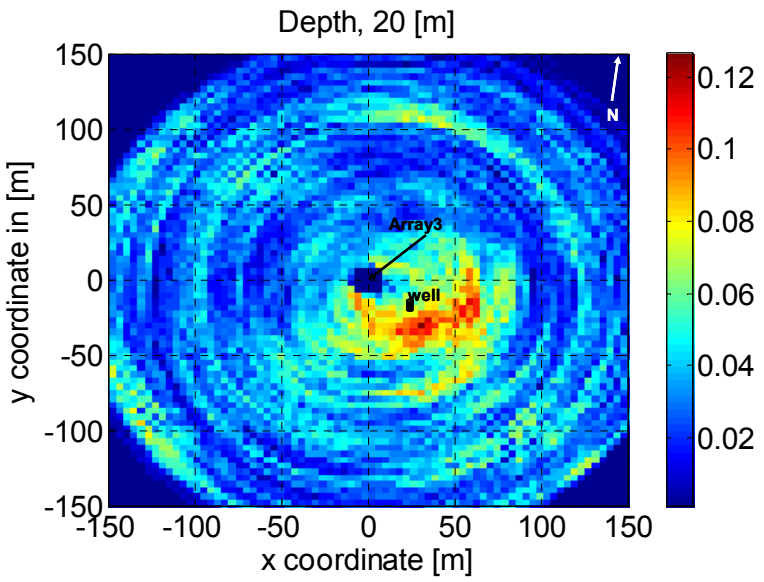

c)

Figure 5.11: Continued

5.4. Summary

The 3-D images from the outcrop arrays (Array1 and Array2) correlate with the observed surface scatterers and the available geological information in the area. The images obtained from Array2 show lower scattering, in areas where the images obtained from Array1 show more intense scattering. This may be due to the fact that the geophones deployed for the data acquisition of Array2, were placed on more irregular surface as those for Array1. This small irregularities may lead to small time lags and therefore to lower semblance coefficient. On the other hand, the angle of incidence of seismic waves on the scatterer affects the radiation pattern of scattered waves. A test on the dependence of the semblance coefficient on that angle must be performed to better understand the effect of low scattering observed on the images from Array2. Such test may provide additional information on the orientation of the scatterer (e.g. fracture).

For the soil site though, the results are not satisfactory. Every attempt to image the water table or the subhorizontal fracture at 22.5 m depth, failed, probably because the assumption for homogeneous velocity is inappropriate, especially within the soil site. To image below the base of the surface layer of saprolite, ray tracing should be used to determine the apparent velocities. The correlation of the 3-D imaging results with additional geophysical information available for each field site is further discussed in Chapter6.

CHAPTER 6

DISCUSSION

The semblance based imaging technique presented here identified a few zones of scattering, at different depths. We compared the imaging results obtained from the scattered surface waves with the location of the observed scatterers on and near the outcrop. Figure 6.1a shows a map of PMRW (Peters et al. 2002), with the study area outlined in red. Figure 6.1b compares the observed and "semblance-based" surface scatterers, for that area of interest. The strongest zone of scattering is observed about 20 m north of the array. This is the location of a small creek, which runs at the bottom of the outcrop. A second zone of scattering (on the order of a grid cell, 5x5m) is about 20m N65E of the array. This maximum in the semblance coefficient correlates with the location of a small ridge (about 4m long). A third zone of scattering is identified at approximately the same distance, but in east direction. It correlates with the location of an exfoliation sheet (about 10m long and 3-4m high). Two tree islands, 40-50m from the array, in E65S direction, are identified on the seismic image as strong surface scatterers as well.

In order to obtain independent information for the scatterers at depth, and compare that with the semblance images, we collected additional geological and geophysical data. This is discussed in the following two sections.

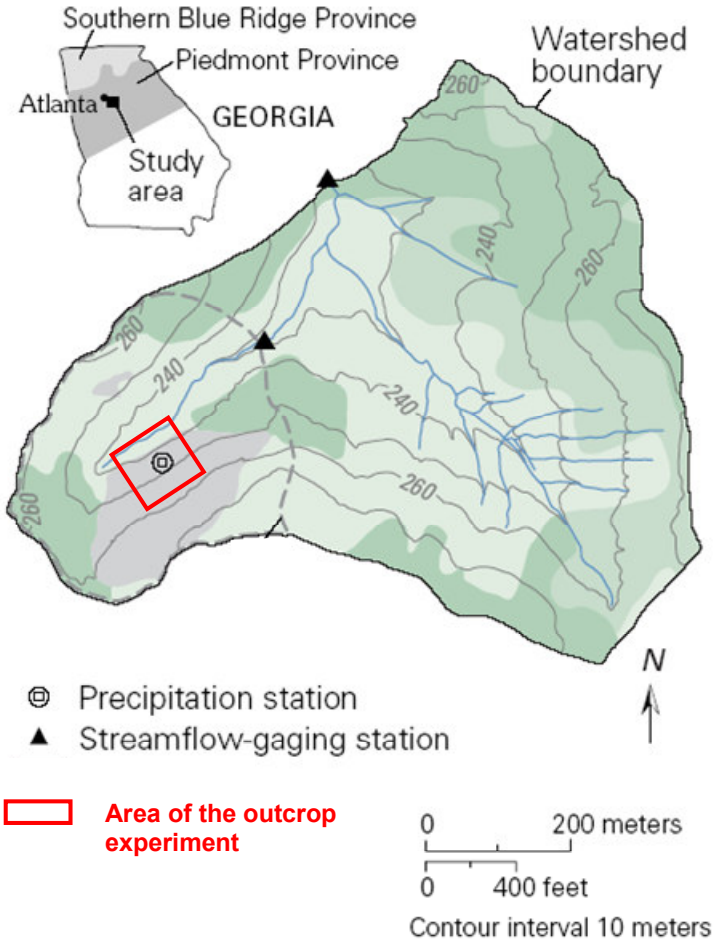

a)

Figure 6.1: (a) map of Panola Mountain Research Watershed, Stockbridge, GA (adopted from Peters et al. 2002); (b) image of surface scatterers (calculated through the semblance algorithm) compared to observed surface scatterers.

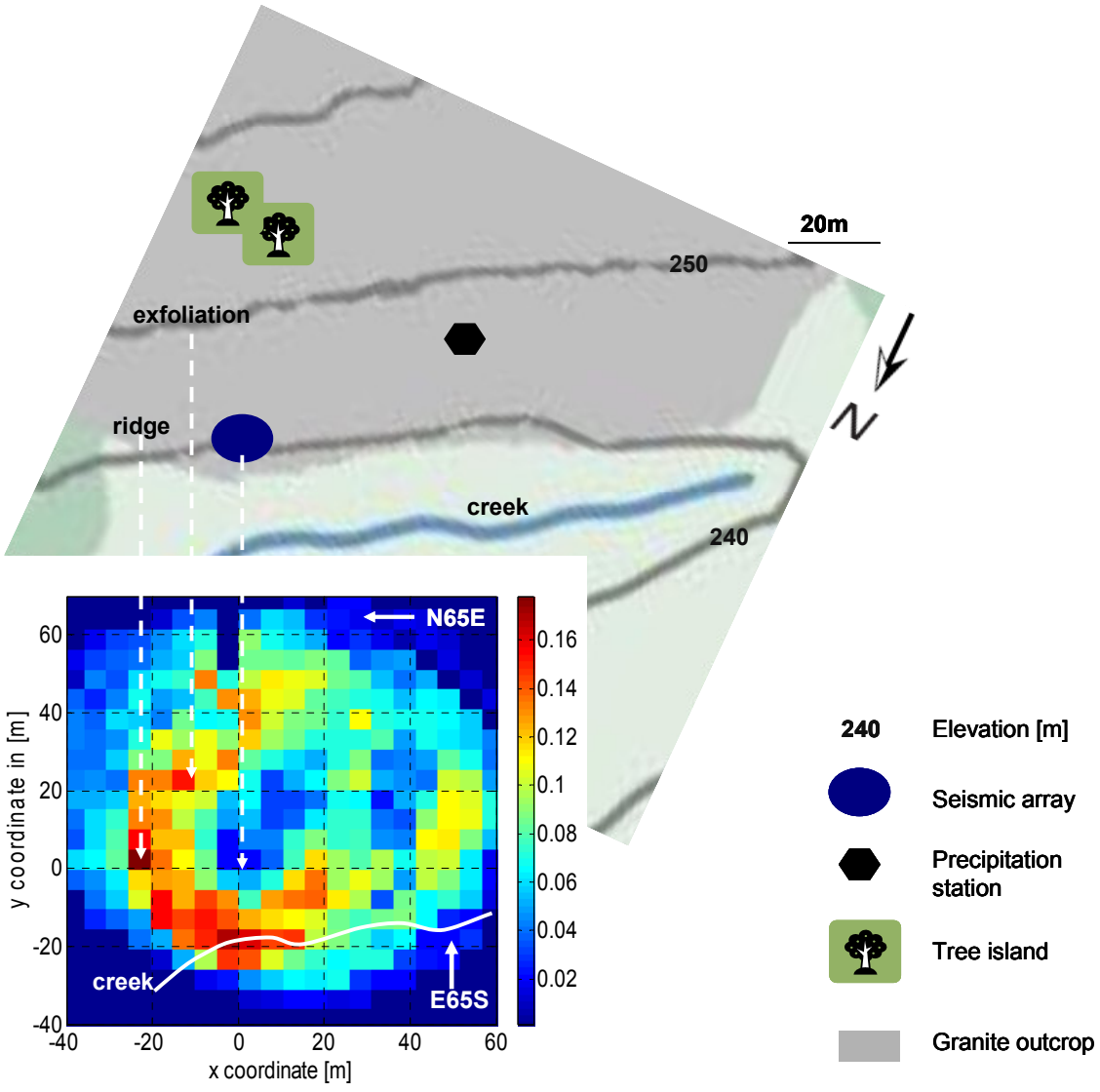

b)

Figure 6.1: Continued

6.1 Discussion of the results from the outcrop arrays

The images obtained for the outcrop were compared with geological and GPR data. Figure 6.2 shows how the semblance cross-section along E65°S compares to a geological cross-section along the same profile line. The location of the creek is marked by high semblance coefficient, and the rest of the outcrop does not show much scattering as it was expected. The geological cross-section indicated that the contact zone between granite and regolith is at 70m from the center of Array1, in E65°S direction. This contact zone is not well defined on the semblance cross-section. This may be due to the fact that the transition from granite to regolith is not as abrupt as it is shown on the geological cross-section. In addition, the contact zone may have very different geometry, and depth as what is observed on the surface. Figure 6.3 compares the semblance cross-section (along the same E65S profile), and a GPR cross-section. The GPR data were acquired with a 250MHz antenna. To determine the depth of the radar reflections we used velocity of 80m/μs (Hebert 2005). The area of the creek is well defined on the GPR image (dotted yellow ellipse), and correlates with the semblance cross-section. The contact zone between granite and regolith, defined by the geological cross-section is characterized by a very weak radar reflection.

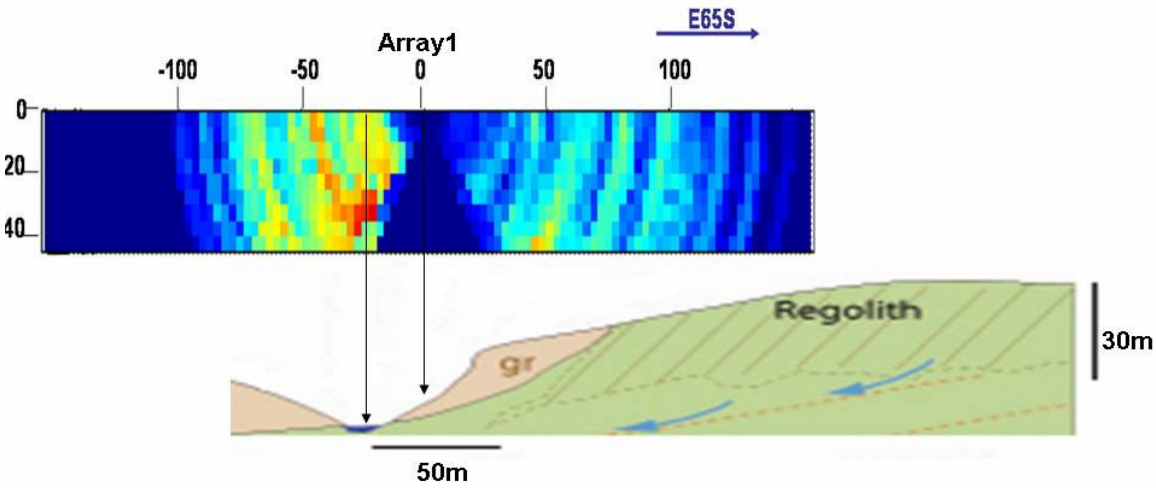

Figure 6.2: Comparison of a semblance (top) and a geological (bottom) cross-section along E65S profile line. Good correlation is observed between the zone of maximum semblance and the location of the creek (at the bottom of the outcrop).

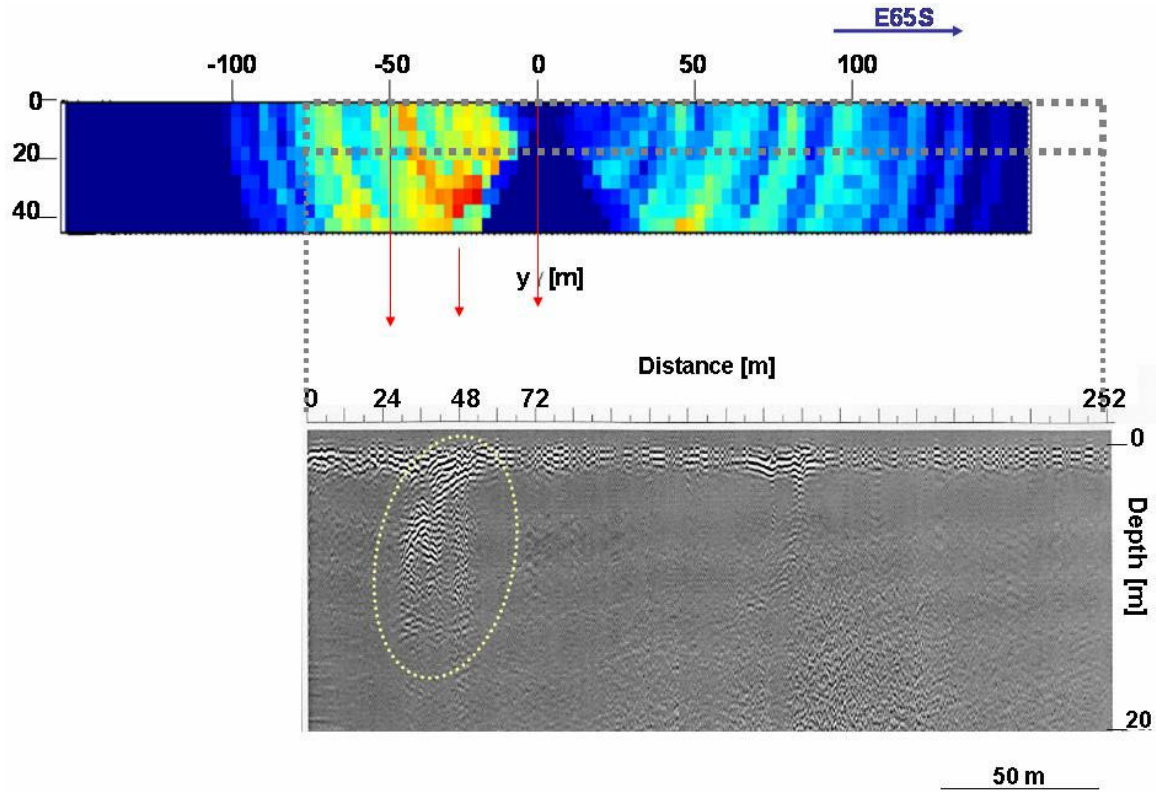

Figure 6.3: Comparison of a semblance (top) and a GPR (bottom) cross section along E65S profile line. The radar reflections from the creek are well defined and correlated with the high semblance coefficient. The contact zone between granite and regolith is identified by a very weak reflection.

Figure 6.4. shows how the semblance images compare with the spatial distribution of different geological formations in the area. Figure 6.4a presents a geological map of Dekalb, Rockdale, and Henry counties (Georgia). PMRW is located in Rockdale County. The area of the outcrop is outlined in red, and compared to a depth image of the semblance coefficient (Figure 6.4b). The boundaries of the outcrop represent a contact zone between the easily weathered Amphibolite-biotite gneiss and the more resistant Panola granite. Some of this contact area is outside the boundaries of the semblance image. For the area around the creek though, the ring-like zone of high semblance (i.e. high scattering) is well correlated with the contact between gneiss and granite.

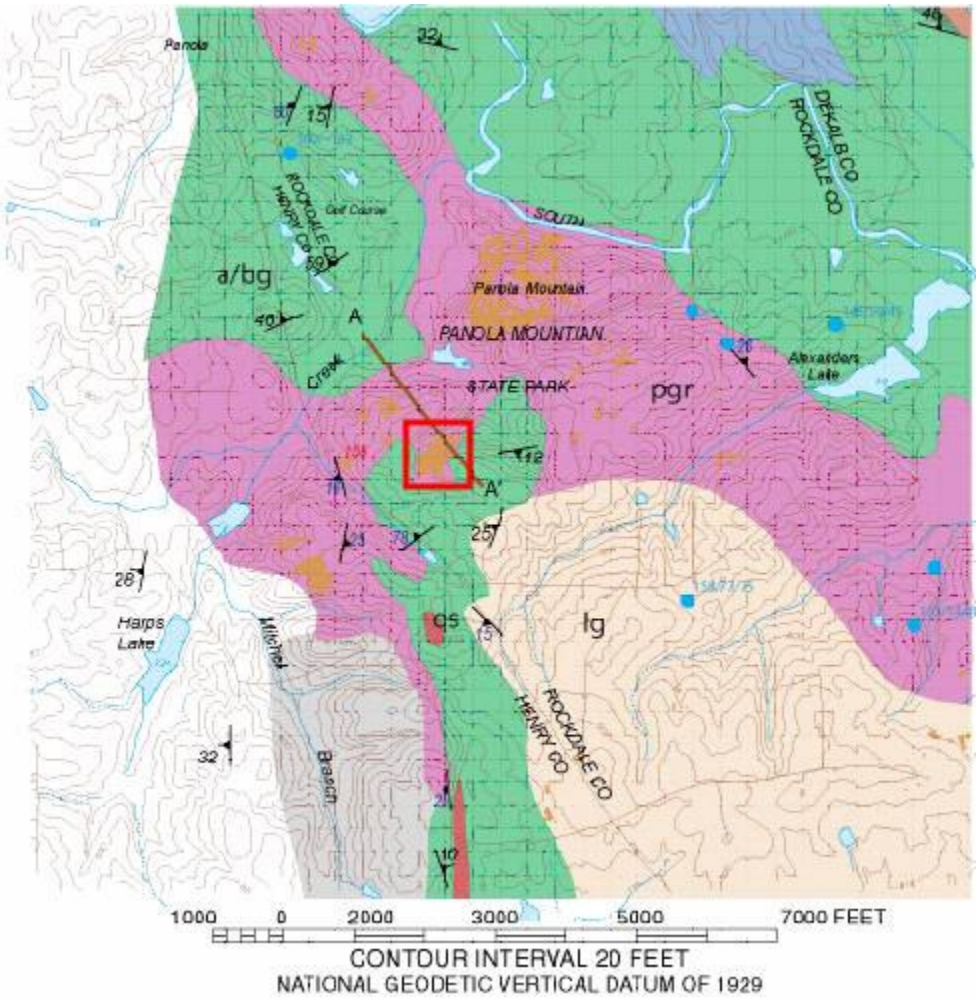

a)

Figure 6.4: (a) Geological map of Dekalb, Rockdale, and Henry counties (Georgia). The area outlined in red contains the granite outcrop and the surrounding formations; (b) comparison of the semblance image at depth of 5m, and the geological map of the outcrop area (modified from Williams 2006).

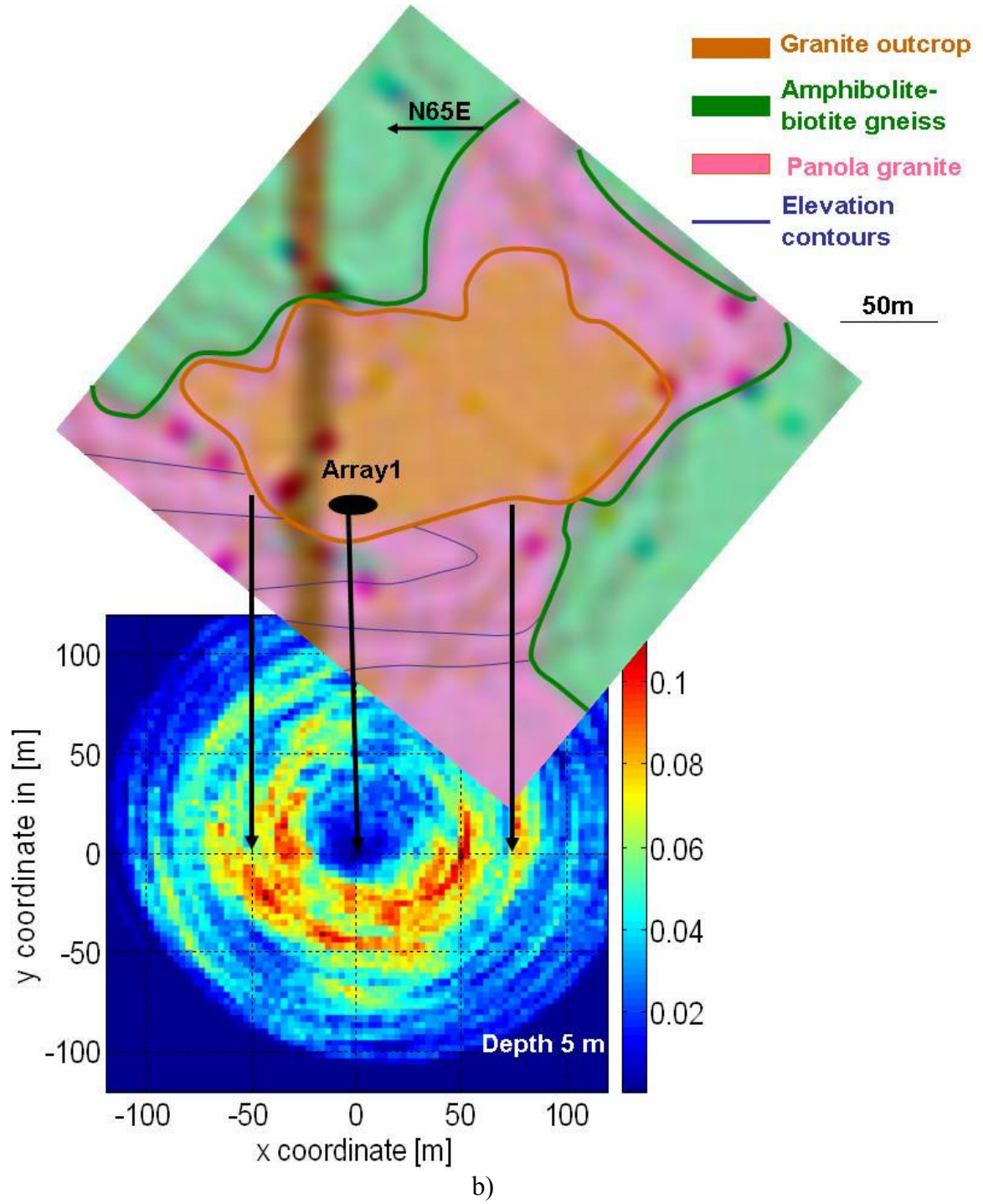

b)

Figure 6.4: Continued

6.2 Discussion of the results from the soil array

At the soil site, we compared the results to resistivity logs from a water well, (USGS -Panola155), which indicated the water table at 7.3m depth, and the bedrock – at 15.2m (Williams, 2006). Well diameter measurements (using well caliper) revealed two fractures at 22.5m, and at 23.2m. From the semblance coefficient of direct body waves, we defined the P wave velocity to be 750m/s within the unsaturated saprolite layer. With this in mind, and assuming 1500m/s P wave velocity for the saturated saprolite, and 2000m/s P wave velocity for the bedrock, we attempted to generate images of the first 40m (in depth) in the area of the well. This attempt failed to image the water table, the bedrock or the fractures within it. This is a consequence of the assumption for homogeneous velocity. In addition, the slow velocity layer above the bedrock would significantly attenuate waves reflected from the bedrock. The strong velocity contrast between saprolite and bedrock traps most of the energy within the saprolite layer. Assuming unweathered bedrock with density of 2600kg/m^3, and density of the saprolite of 1500kg/m^3 (Anderson 1997); for velocity of P waves of 750m/s in the saprolite and 5000m/s in bedrock, the transmission coefficient would be 0.16. With other words only 16% of the input energy will reach the fractures.

On the other hand, the high bedrock velocities imply that waves scattered from the granite or the fractures within it would approach the array at very small angles of incidence. We would need to consider apparent velocities far above 5000m/s to be able to capture these scattered waves. In order to do that the semblance based imaging algorithm has to be substantially modified. An iterative ray-tracing technique must be incorporated to find the exact positions of the scattered waves.

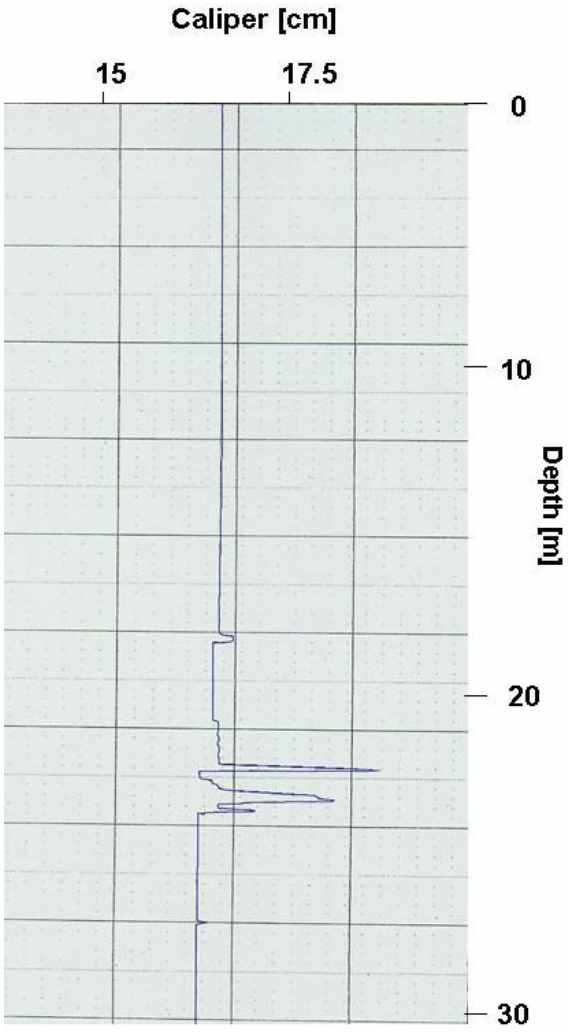

Figure 6.5.: Caliper data from well Panola155. Two fractures are observed at depths of 22.5m and 23.2m (Williams 2006).

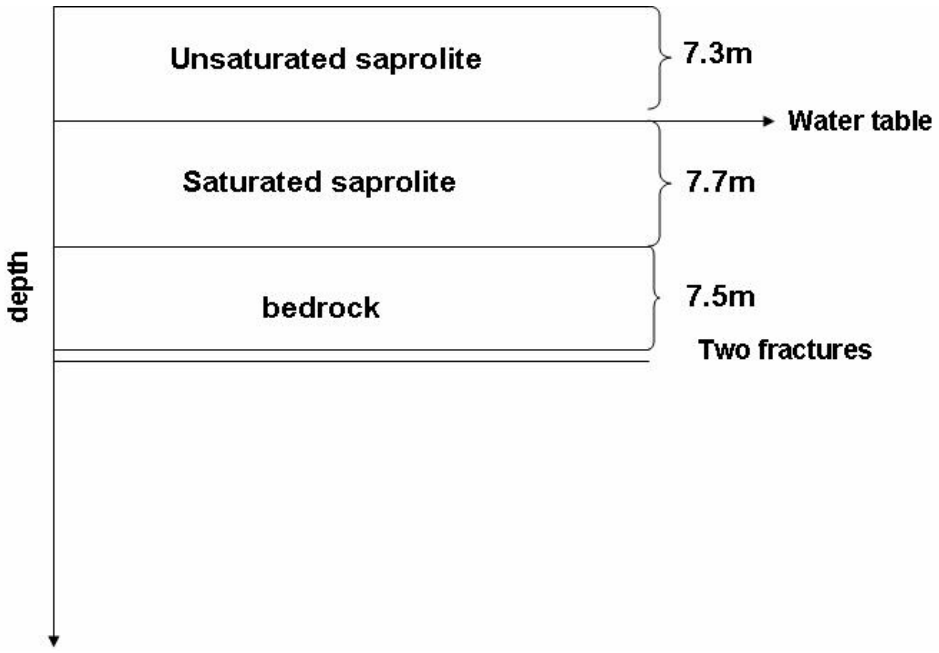

Figure 6.6: Depth model extracted from resistivity and caliper data at Panola155.

CHAPTER 7

CONCLUSIONS

The heterogeneity of the Earth is both compositional and mechanical and exists on all scales. Mechanical heterogeneities are discontinuities in which loss of cohesion has taken place. Such loss of cohesion results in greater scattering potential. Due to the low temperature and confining pressure the near-surface discontinuities are more likely to be open and therefore to scatter seismic energy more efficiently. Despite the numerous surveys and huge amount of seismic data collected over the last 50 years, the imaging of scatterers remains a challenging problem due to their complex response to incident seismic energy. Three-dimensional imaging algorithms have been developed for large-scale surveys (deep scatterers), or for dense seismic arrays. The imaging of shallow discontinuities has been done using modified versions of conventional seismic reflection methods. They are not cost-efficient for near-surface applications

We conducted three small-scale seismic experiments with the objective of identifying shallow scatterers. The imaging of scattering objects in the earth was performed by a search for scattered seismic waves, using the semblance coefficient. The semblance coefficient is a statistical measure of the similarity between multiple channels. We were able to obtain 3-D images from three seismic arrays, at two different field sites. We made a number of assumptions in developing the technique: 1) we assumed plane wave propagation, which is acceptable for distant sources and equivalently for small aperture of the array; 2) we assumed elastic wave propagation, which is acceptable for low temperature and pressures, and small strains (Turcotte and Schubert, 2002); 3) we

assumed that all noise is random; 4) we assumed that areas of fracture clustering would generate strong coherent scattering energy. This assumption is supported by the results from numerical simulations of wave propagation in media with discrete distribution of scatterers (Vlastos et al., 2003); 5) we assumed single scattering. It was found to be the dominant mechanism of scattering for short lapse times, small station-source distances, and weak scattering medium (Chen, 1999; Goutbeek et al., 2004); 6) homogeneous velocity was assumed for the imaging algorithm.

We found that the poor coupling between a geophone and the rock is a potential source of undamped resonances. In addition, the semblance analysis shows that narrow-band frequency filtering and short time intervals are necessary to minimize the interference from wavelets with different lengths and arrival times. The length of the time interval is chosen to be equal to one cycle of the predominant frequency. This way, we make the assumption of a single cycle wavelet. This would not be appropriate assumption for more complex sources such as Vibroseis, or when undamped geophone resonance frequencies are present. In these cases the effect that we observed may not be as prominent.

7.1. Imaging obtained from the outcrop field site

The high semblance areas observed on the surface of the outcrop, obtained from surface waves, correlate with the location of a small creek running at the bottom of the outcrop and other topographic features in the area. This zone of intense scattering extends to the east, where the edge of the outcrop is observed and southeast (above the array), which correlates with a zone of trees, a ridge and exfoliation sheets. The area southwest of the array that shows lowest semblance was not observed to have any surface scatterers.

We observe this low scattering on the images obtained from both Array1 and Array2. Some discrepancies are observed between the images from the two outcrop arrays. A few zones of strong scattering observed from Array1, are not as intense on the images from Array2. This may be due to two different factors. First, the geophones deployed for Array2 acquisitions, were placed on much more irregular surface, than they were for the Array1 acquisition. This may lead to small time lags between the channels, and from there – to lower semblance coefficient. Second, the radiation pattern of scattered waves depends on the angle of incidence to the scatterer. Further study of the dependence of the semblance coefficient on the angle of incidence is necessary to asses the lower scattering observed from Array2. Such test may also provide information on the orientation of the scatterer (e.g. fracture).

The three-dimensional images from the outcrop field site, obtained from scattered P and S waves, show good correlation with the geological and GPR data collected in the area. The geological cross-section and map suggest that the site of the creek is part of a contact zone between granite and amphibolite-biotite gneiss, and probably is controlled by fracture and joint concentration (Williams, 2006). Both GPR and semblance images support that suggestion. We noted that Panola granite is generally unweathered in comparison to the amphibolite-biotite gneiss. Therefore, the contact zone is represented by a sufficient difference in the elastic properties of the two different types of rock, to scatter seismic waves.

7.2. Images obtained from the soil field site

Much narrower frequency filters were needed for the data from the soil site in order to avoid contamination from dispersed surface waves. Because surface and body waves were well isolated in frequency, we were able to identify scattered P and S waves, with very high semblance coefficient. The semblance algorithm failed to image the subhorizontal fractures within the bedrock. We believe this is due to a number of factors: 1) because of the strong velocity contrast between saprolite and bedrock only small portion of the input energy would reach the bedrock fractures; 2) the slow velocity layer above the bedrock would significantly attenuate waves reflected from the bedrock. However, waves scattered from the granite or the fractures within it would approach the array at very small angles of incidence, due to the high bedrock velocity. In order to image the bedrock fractures an iterative ray-tracing technique must be incorporated to find the exact positions of the scattered waves.

7.3. Recommendations for future work

- An "all-azimuth" distribution of source positions would have improved the imaging in all directions from the array.
- When the experiment is conducted on an outcrop, we recommend that the geophones are firmly attached to the rock using gypsum and not just attached with clay to a cement platform. The drying and cracking of the clay that we used to attach the geophones released some geophones and allowed undamped resonance to contaminate the response.

- In addition, the use of three-component geophones will improve significantly the ability to identify shear waves, particularly those with near vertical incidence that have apparent velocities greater than the P-wave velocity.
- The use of a 24-channel array will allow for larger spatial coverage.
- For a soil site, geophones should be buried under the soil layer, to avoid the generation of surface waves. This would also imply a more homogeneous velocity model (avoiding the two layers of saturated and unsaturated saprolite that we had). If possible the source should be applied to the bedrock as well.
- In order to reach greater depths, a more powerful source should be used. On hard rock, the source we used was sufficient, approximately 5 kg for a 100x100 square meter area. Larger areas would need larger source.

REFERENCES

Abma, R. and N. Kabir, 2005. Comparison of interpolation methods. The Leading Edge, October, pp.984-989.

Aki K., and P. G. Richards, 2002. Quantitative Seismology. University Science Books

Bachrach R., and A. Nur, 1998. High resolution shallow-seismic experiments in sand, Part1: Water table, fluid flow, and saturation. Geophysics, vol.63, No.4, pp.1225-1233.

Bachrach R., and T. Mukerji, 2004. Portable dense geophone array for shallow and very shallow 3D seismic reflection surveying – Part1: Data acquisition, quality control, and processing. Geophysics, vol.69, No.6, pp.1443-1455.

Bachrach R., and T. Mukerji, 2004. The effect of texture and porosity on seismic reflection amplitude in granular sediments: Theory and examples from a high-resolution shallow seismic experiment. Geophysics, vol.69, No.6, pp.1513-1520.

Bachrach R., J. Dvorkin, and A. Nur, 1998. High resolution shallow-seismic experiments in sand, Part2: Velocities in shallow unconsolidated sand. Geophysics, vol.63, No.4, pp.1234-1240.

Baker G., C. Schmeissner, D. W. Steeples, and R. Plumb, 1999. Seismic reflections of less than two meters. Geoph. Res. Lett., vol.26, No.2, pp.279-282.

Bannister, S., and Melhuish, A., 1997, Seismic scattering and reverberation Kaingaroa plateau Taupo volcanic zone New Zealand, New Zealand J. of Geol. And Geoph., 40, 375-381.

Boadu F., 1994. Fractal characterization of fractures:effet of fractures on seismic wave velocity and attenuation. PhD Thesis, Georgia Tech.

Bradford J., L. Liberty, M. Lyle, B. Clement, and S. Hess, 2006. Imaging complex structure in shallow seismic-reflection data using pre-stack migration. Geophysics, in review.

Brown S., and C. H. Scholz, 1986. Closer of rock joints. J. Geophys. Res., vol.91, pp.4939-4948.

Buker F., A. G. Green, and H. Horstmeyer, 1998. Shallow 3-D seismic reflection surveying: Data acquisition and preliminary processing strategies. Geophysics, vol.63, No.4, pp.1434-1450.

Chen M., and T. Long., 2004. GT-SDAP&DiffView Installation guide. Georgia Institute of Technology.

Chen X., and L. T. Long, 2000. Spatial distribution of relative scattering coefficients determined from microearthquake coda. BSSA, 90,2,pp.512-524.

Chen X., 1999. On the characteristics of coda scatterers for shallow earthquakes. PhD Thesis, Georgia Institute of Technology.

Douze E. J., and S. J. Laster, 1979. Statistics of semblance. Geophysics, vol.44, No.12, pp.1999-2003.

Fehler M., P. Roberts, and T. Fairbanks, 1988. A temporal change in coda wave attenuation observed during an eruption of Mount St. Helens. J. Geophys. Res., vol.93, pp.4367-4373.

Ghose R., V. Nijhof, J. Brouwer, Y. Matsubara, Y. Kaida, and T. Takahashi, 1998. Shallow to very shallow, high-resolution reflection seismic using a portable vibrator system. Geophysics, vol.63, No.4, pp.1295-1309.

Goutbeek F. H., B. Dost, and T. van Eck, 2004. Intrinsic absorption and scattering attenuation in the southern part of the Netherlands. Journal of Seismology, vol.8, No.1, pp.11-23.

Grimm, R., H. B. Lynn, C. R. Bates, D. R. Phillips, K. M. Simon, and W. E. Beckham, 1999. Detection and analysis of naturally fractured gas reservoirs: multiazimuth seismic surveys in the wind river basin, Wyoming. Geophysics, vol.64, No.4, pp.1277-1292.

Groenenboom J., and J. Falk, 2000. Scattering by hydraulic fractures: finite difference modeling and laboratory data. Geophysics, vol.65, No.2, pp.612-622.

Hauge G., and M. Schoenberg, 2000. The echo of a fault or fracture. Geophysics, ol.65, No.1, pp.176-189.

Hebert G. J., 2005. A Geophysical Investigation of Hydraulic Pathways at the Panola Mountain Research Watershed. MS Thesis, Georgia Institute of Technology.

Hunter J. A., S. E. Pullan, R. A. Burns, R. M. Gagne, and R. L. Good, 1984. Shallow seismic reflection mapping of the overburden-bedrock interface with the engineering seismograph – Some simple techniques. Geophysics, vol.49, No.8, pp.1381-1385.

Hunter J.A., and G. D. Hobson, 1977. Reflections on shallow seismic records. Geoexploration, vol.15, pp.183-193.

Jin A., and K. Aki, 1989. Spatial and temporal correlation between coda Q and seismicity and its physical mechanism, J. Geophys. Res., vol.94, pp.14041-14059.

Kearey Philip, and M. Brooks, 1991. An introduction to geophysical exploration. Second edition, Blackwell Science.

Kruger F., M. Baumann, F. Scherbaum, and M. Weber, 2001. Mid mantle scatterers near the Mariana slab detected with a double array method. Geophys. Res. Lett., vol.28, No.4, pp.667-670.

Kuwahara Y., H. Ito, H. Kawakatsu, T. Ohminato, and T. Kiguchi, 1997. Crustal heterogeneity as inferred from seismic coda wave decomposition by small-aperture array observation. Phys. Earth Planet. Int., vol.104, pp.247-256.

Lacoss T. E., E. J. Kelly, and M. N. Toksoz, 1969. Estimation of seismic noise structure using arrays. Geophysics, vol.34, pp.21-38.

Lanz E., A. Pugin, A. Green, and H. Horstmeyer, 1996. Results of 2- and 3-D high-resolution seismic reflection surveying of surficial sediments. Geoph. Res. Lett., vol.23, No.5, pp.491-494.

Liner C., 1999. Elements of 3-D seismology. PennWell.

Loui J. N., S. Chavez-Perez, S. Henrys, and S. Bannister, 2002. Multimode migration of scattered and converted waves for the structure of the Hikurangi slab interface, New Zealand. Tectonophysics, vol.355, pp.227-246.

Matsumoto S., K. Obara, and A. Hasegawa, 1998. Imaging P-wave scatterer distribution in the focal area of the 1995 M7.2 Hyogo-ken Nanbu (Kobe) earthquake. Geophys. Res. Lett., vol.25, No.9, pp.1439-1442.

Miller R. D., D. W. Steeples, and M. Brannan, 1989. Mapping a bedrock surface under dry alluvium with shallow seismic reflections. Geophysics, vol.54, No.12, pp.1528-1534.

Milsom John, 1996. Field Geophysics, Second Edition, John Wiley & Sons Ltd.

Neidell, N., and Taner, T., 1971. Semblance and other coherency measures for multichannel data, Geophysics, 36, 482-497.

Nikolaev, A., and Troitskiy, P., 1987. Lithosperic studies based on array analysis of P-coda and microseisms, Tectonophysics, 140, 103-113.

Nishigami K., 2000. Deep crustal heterogeneity along and around the San Andreas fault system in central California and its relation to the segmentation. J. Geophys. Res., vol.105, No.B4, pp.7983-7998.

Novelo-Casanova et al., 1985. Time-space variation in seismic S-wave coda attenuation (Q^{-1}) and magnitude distribution (b-values) for the Petatlan earthquake. Geophys. Res. Lett., vol.12, pp.789-792.

Peters, N., Hooper R.P., Huntington T.G., and Aulenbach B.T., 2000. Panola Mountain, Georgia: a water, energy, and biogeochemical budgets program site. USGS Fact Sheet 162-00.

Revenaugh J., 1999. Geological applications of seismic scattering. Ann. Ev. Earth Planet. Sci., 27, pp.55-73.

Rieber, F., 1936. A new reflection system with controlled directional sensitivity. Geophysics, vol.1, No.1, pp.97-106.

Rietbrock, A., and F. Scherbaum, 1999. Crustal scattering at the KTB from a combined microearthquake and receiver analysis. Geophys. J. Int., vol.136, pp.57-67.

Rost S., and C. Thomas, 2002. Array seismology: methods and applications. Reviews of geophysics, vol.40, No.3, pp.2/1-2/27.

Sato H., and M. Fehler, 1998. Seismic wave propagation and scattering in the heterogeneous earth. Springer-Verlag, N.Y, Inc.

Sayers C., 2002. Fluid-dependent shear-wave splitting in fractured media. Geophysical Prospecting, 50, pp.393-401.

Schepers R., 1975. A seismic reflection method for solving engineering problems. J. Geophys., vol.41, pp.367-384.

Scherbaum F., D. Gillard, and N. Deichmann, 1991. Slowness power spectrum analysis of the coda composition of two microearthquake clusters in northern Switzerland. Phys. Earth Planet. Int., vol.67, No.1-2, pp.137-161.

Scherbaum F., F. Kruger, and M. Weber, 1997. Double beam imaging: mapping lower mantle heterogeneities using combinations of source and receiver arrays. J. Geophys. Res., vol.102, No.B1, pp.507-522.

Sheriff R. E., 2002. Encyclopedic dictionary of Applied Geophysics. Society of Exploration Geophysics.

Sheriff, R. E. and L.P. Geldart, 1982. Exploration seismology. Vol 1, Cambridge University Press.

Shtivelman V., U. Frieslander, and E. Zilberman, 1998. Mapping shallow faults at the Evrona playa site using high-resolution reflection method. Geophysics, vol.63, No.4, pp.1257-1264.

Simmons G., and A. Nur, 1968. Granites – relation of properties in situ to laboratory measurements. Science, vol.162, pp.789-791.

Simpson, S. M., 1967. Traveling signal-to-noise ratio and signal power estimates. Geophysics, vol.32, No.3, pp.185-193.

Spitzer R., F. Nitsche, A. G. Green, and H. Horstmeyer, 2003. Efficient acquisition, processing, and interpretation strategy for shallow 3D seismic surveying: A case study. Geophysics, vol.68, No.6, pp.1792-1806.

Spudich P., and T. Bostwick, 1987. Studies of the seismic coda using an earthquake cluster as a deeply buried seismograph array. J. Geophys. Res., vol.92, No.B10, pp.10526-10546.

Steeples D., 2001. Engineering and environmental geophysics at the millennium. Geophysics, vol.66, No.1, pp.31-35.

Steeples D., A. G. Green, T. V. McEvilly, R. D. Miller, W. E. Doll, and J. W. Rector, 1997. A workshop examination of shallow reflection surveying. The Leading Edge, vol.16, pp.1641-1646.

Steeples D., and R. D. Miller, 1998. Avoiding pitfalls in shallow seismic reflection surveys. Geophysics, vol.63, pp.1213-1224.

Taner M. T., and F. Koehler, 1969. Velocity spectra-digital computer derivation and applications of velocity functions. Geophysics, vol.34, No.6, pp.859-881.

Tchebotareva, I., Nikolaev, A., Sato, H., 2000, Seismic emission activity of Earth's crust in Northern Kanto, Japan, Phys. of E. and Pl.Int., 120, 167-182.

Telford W. M., L. P. Geldart, and R. E. Sheriff. Applied Geophysics, Second Edition, 1990, Cambridge University Press

Thomas C., M. Weber, C. W. Wicks, and F. Scherbaum, 1999. Small scatterers in the lower mantle observed at the German broadband arrays. J Geophys.Res., vol.104, No.B7, pp.15073-15088.

Turcotte D. L., and G. Schubert, 2002. Geodynamics. Cambridge University Press.

Turner J., 1998. Scattering and diffusion of seismic waves. BSSA, vol.88, No.1, pp.276-283.

Van der Kolk C., W. S. Guest, J. H. H. M. Potters, 2001. The 3D shear experiment over the Natih field in Oman: the effect of fracture-filling fluids on shear propagation. Geophysical Prospecting, 49, pp.179-197.

Vlastos S., E. Liu, I. G. Main, and X.-Y. Li, 2003. Numerical simulation of wave propagation in media with discrete distribution of fractures: effect of fracture sizes and spatial distributions.

Walsh J. B., 1965. The effect of scacks on the compressibility of the rock. J. Geophys. Res., 70, pp.381-389.

Walsh J. G., and M. A. Grosenbaugh, 1974. A new model for analyzing the effect of fractures on compressibility. J. Geophys. Res., vol.84, pp.3532-3542.

White A., Blum A.E., Schulz M.S., Huntington T.G., Peters N.E., and Stonestrom D.A. (2002). Chemical weathering of the Panola granite: solute and regolith elemental fluxes and the weathering rate of biotite. Rock-Water Interactions, Ore Deposits and Environmental chemistry, 7, pp.37-59.

Williams L., 2003, Overview of geology, ground-water availability, and ground-water exploration and development in the greater Atlanta region, USGS Guidebook 23, 4-15.

Williams L., and W. Burton., 2005. Common types of water bearing features in bedrock, Rockdale county, Georgia. Proc. Georgia Water Resources Conf., Athens, GA.

Williams, L., 2006. Personal communication.

Yilmaz O., and S. Doherty, 1987. Seismic Data Processing (Investigations in Geophysics, Vol 2), Society of Exploration Geophysicsts.